SENSORY FUNCTIONS OF THE BACTERIAL FLAGELLAR MOTOR

A Dissertation

by

JYOT ANTANI

Submitted to the Office of Graduate and Professional Studies of
Texas A&M University
in partial fulfillment of the requirements for the degree of

DOCTOR OF PHILOSOPHY

Chair of Committee,	Pushkar Lele
Committee Members,	Steve Lockless
	Arul Jayaraman
	Qing Sun
Head of Department,	Arul Jayaraman

August 2021

Major Subject: Chemical Engineering

ABSTRACT

Motility helps bacteria explore different environments and promotes the chances of their survival. Motility is powered by the rotation of thin helical appendages called flagella. Each flagellum is rotated by a transmembrane flagellar motor. A flagellar motor consists of a rotor and several stator units that deliver torque. Switching in the direction of the motor rotation enables navigation in response to chemical signals – termed chemotaxis – which helps the cell swim to favorable surfaces. In addition, the flagellar motor has been implicated in tactile sensing of surfaces, which helps bacteria establish colonies on surfaces. Previous research indicated that physical obstruction of the rotation of the flagellar motor caused several stator units to be recruited in *Escherichia coli*. The role of stator recruitment in the signaling events that lead to bacterial colonization of surfaces is unknown. In this work, I discuss our recent efforts to explain the mechanisms by which stator recruitment modulates the binding affinity of a major chemotaxis protein, CheY-P, to the flagellar motor. Our results indicate that the motor regulates its sensitivity to chemical signals by controlling the binding of CheY-P to the motor with mechanical force. These findings explain for the first time how bacteria are able to robustly target different niches irrespective of the fluctuations in the environmental conditions. To further delineate the link between environmental fluctuations and chemotaxis, we worked with a carcinogenic pathogen, *H. pylori*. The major technical challenge in *H. pylori* is the lack of suitable assays to probe the behavior of flagellar motors. Using particle-tracking approaches, we discovered that *H. pylori* cells swim faster when moving forward, and slower when swimming backward. Based on this

finding, we developed a novel approach to determine the sensory output of the flagellar motors. This approach revealed that *H. pylori* employ a flagellar modulation strategy that is very similar to that employed by the model species, *E. coli*. These findings shed light on fundamental problems in chemotaxis and bacterial colonization, which are major biomedical challenges.

DEDICATION

…to my grandfather, Chandrakumar Antani, who taught me to always aspire for the greatest intellectual role.

…to my grandmother, Jyotsna Antani, who taught me to really think about what I read.

…to my father, Digant Antani, who taught me to consider many different perspectives.

…to my mother, Jignasa Antani, who taught me to work my hardest to achieve my dreams.

…to my fiancée, Twara Baxi, who is teaching me to believe in myself.

…to science:

असतो मा सद्गमय ।	From falsehood lead me to truth.
तमसो मा ज्योतिर्गमय ।	From darkness lead me to light.
मृत्योर्माऽमृतं गमय ॥	From death lead me to immortality.

ACKNOWLEDGEMENTS

I would like to thank my committee chair, Dr. Lele, for his guidance throughout the course of this research. While being in his lab, I have learned a tremendous amount about science, life, and the science of life. Thanks also to my committee members, Dr. Lockless, Dr. Jayaraman, and Dr. Sun, for their support and inputs during and beyond the committee meetings. Special thanks are due to Dr. Michael Manson for his *persistent* mentoring. Mike was an Honorary Committee Member: he actively participated in the discussions about my results and provided invaluable guidance on multiple manuscripts. I will miss our scientific (and other) conversations on Mike's porch.

Thanks also go to the numerous friends and connections who made my time at Texas A&M University a memorable experience. Special thanks to Ashley Henley for making life in the department easier. Neha and Rishita, thanks for being home away from home in the beginning of this PhD. Thanks to Aayushman and Roshan, for making a routine out of the much-needed coffee trips and movie nights during the last year.

Thanks are also due, to the current and past members of the Lele Lab. Thanks to Katie for the best book recommendations! Big thanks to Ravi for being a true academic elder brother – for making me realize the value of socializing in science, and later guiding me in the postdoc search. Katie, Ravi, Anusha, Annie, Kathy, Rachit, Siddu, Aravindh, Anita: thanks all of you for being supportive coworkers and delightful friends!

Finally, thanks to my family, especially Mumma, Pappa, and Twara, for their encouragement, patience, and love.

CONTRIBUTORS AND FUNDING SOURCES

Contributors

This work was supervised by a dissertation committee consisting of Dr. Pushkar Lele (advisor), Dr. Arul Jayaraman, and Dr. Qing Sun of the Department of Chemical Engineering, and Dr. Steve Lockless of the Department of Biology. Dr. Michael Manson (Professor Emeritus, Department of Biology) got involved as an honorary but active member of the committee.

Chapter 2 is part of a topical review titled “Roadmap on emerging concepts in the physical biology of bacterial biofilms: from surface sensing to community formation”, published in *Physical Biology* (2021).

Chapter 3 is a manuscript titled “Proprioception in the *Escherichia coli* flagellar motor”, currently under review. Rachit Gupta and Annie Lee helped with the experiments and analyses indicated as a black square in Figure 3-2E.

Chapter 4 is reprinted from the article “Asymmetric random walks reveal that the chemotaxis network modulates flagellar rotational bias in *Helicobacter pylori*”, published in *eLife* (2021). Anita Sumali helped with the data analysis. Dr. Tanmay Lele helped in the model development.

Appendix C is part of the journal article, “A method for direct imaging of x–z cross-sections of fluorescent samples”, published in *Journal of Microscopy* (2020). This work was a collaboration with Tanmay Lele Lab. The experiment described was carried out by Aditya Katiyar. Appendix D is part of another collaborative project with the Tanmay Lele Lab. The microscopy images were provided by Aditya Katiyar.

All other work conducted for this dissertation was completed by me under the guidance of Dr. Pushkar Lele.

Funding Sources

This work was supported in part by grants from the DOD ACC-APG-RTP Division (W911NF1810353), the National Institute of General Medical Sciences United States (R01-GM123085), and the Cancer Prevention and Research Institute of Texas (RP170805) to Dr. Pushkar Lele. The funding agencies had no role in study design, data collection or interpretation, or the decision to submit the work for publication.

NOMENCLATURE

CW	clockwise
CCW	counterclockwise
YFP	yellow fluorescent protein
CW_{bias}	clockwise bias
Amp	ampicillin
Amp^R	ampicillin resistant
Chloro	chloramphenicol
Cm^R	chloramphenicol resistant
Kan	kanamycin
LB	Lysogeny Broth / Luria Bertani media
MB	Motility Buffer
DMSO	dimethyl sulfoxide
N_{st}	Number of stator units bound to the motor
[CheY-P]	Intracellular concentration of phosphorylated CheY

TABLE OF CONTENTS

Page

LIST OF FIGURES

Page

LIST OF TABLES

Page

1. INTRODUCTION

Antibiotic resistance in pathogenic microbes poses one of the biggest threats to public health. According to a 2019 report by the Center for Disease Control (USA), more than 2.8 million antibiotic-resistant infections occur in the USA every year, and this results in over 35,000 deaths [1]. Due to major challenges to the discovery of new antibiotic compounds, we need to devise alternative techniques to treat infections. Hence, a wide area of research has focused on antivirulence measures by trying to identify the factors involved in microbial virulence. Bacterial communities such as biofilms are resistant to external stressors such as antibiotics. Hence, research efforts focus on determining the intracellular processes that contribute to the formation of biofilms. Such fundamental research can motivate new drug design, which will aid in our fight against antibiotic resistance. In this dissertation, I discuss some of the biophysical mechanisms involved in how bacterial cells explore different environments, sense environmental cues, and identify a suitable niche for establishing a community.

Bacterial motility is a key fitness factor responsible for robust host invasion. Motility is powered by the rotation of helical filaments called flagella, which are appendages that protrude from the cell body. The torque required for the rotation of each helical flagellum is delivered by a flagellar motor, which is a transmembrane organelle made up of numerous proteins [2]. *E. coli* consists of 4 to 6 nonpolar peritrichous flagella, which means that the flagellar motors are distributed throughout the outer membrane. Each motor switches between clockwise (CW) and counterclockwise (CCW) directions of rotation, which in turn rotates the flagellum in the corresponding directions.

When all the flagella of a single *E. coli* rotate CCW, they bundle up together to push the bacterium in a single direction – this is called a *run*. When one or more flagella switch the direction of rotation to CW, the bundle comes apart and the cell may undergo reorientation – this is called a *tumble*. Through modulation of the runs and tumbles (Figure 1-1A), the cell performs a biased random walk towards favorable pastures [3].

Migration of bacteria towards favorable chemical environments is termed chemotaxis, which occurs through a cascade of protein-mediated signaling (Figure 1-1B). Briefly, in the two-component chemotaxis signaling network, binding of an attractant molecule to the chemoreceptors reduces the activity of the kinase CheA, which in turn decreases the rate of phosphorylation of the response regulator CheY. As a result, less CheY-P binds to the motor and the motor is more likely to turn counterclockwise (CCW), so the runs are extended. This is because CheY-P binding promotes CW motor rotation. There are at least two major control modules for the intracellular concentration of CheY-P, in the form of the phosphatase and the adaptation enzymes. The probability of CW rotation of the motor, the CW_{bias}, is ultrasensitive to the intracellular concentration of CheY-P [4, 5]: it goes from 0 to 1 within a narrow range (~2.5 μM to 5 μM) of [CheY-P]. Thus, the network in *E. coli* enables chemotaxis through modulation of the CW_{bias} in the flagellar motor. In addition to navigation in response to chemical signals, flagellar switching has also been implicated in responding to mechanical and thermal stimuli [6-9]. In this dissertation, I will discuss our work uncovering some of the fundamental principles that govern the modulation of flagellar switching by mechanical, chemical, and thermal signals.

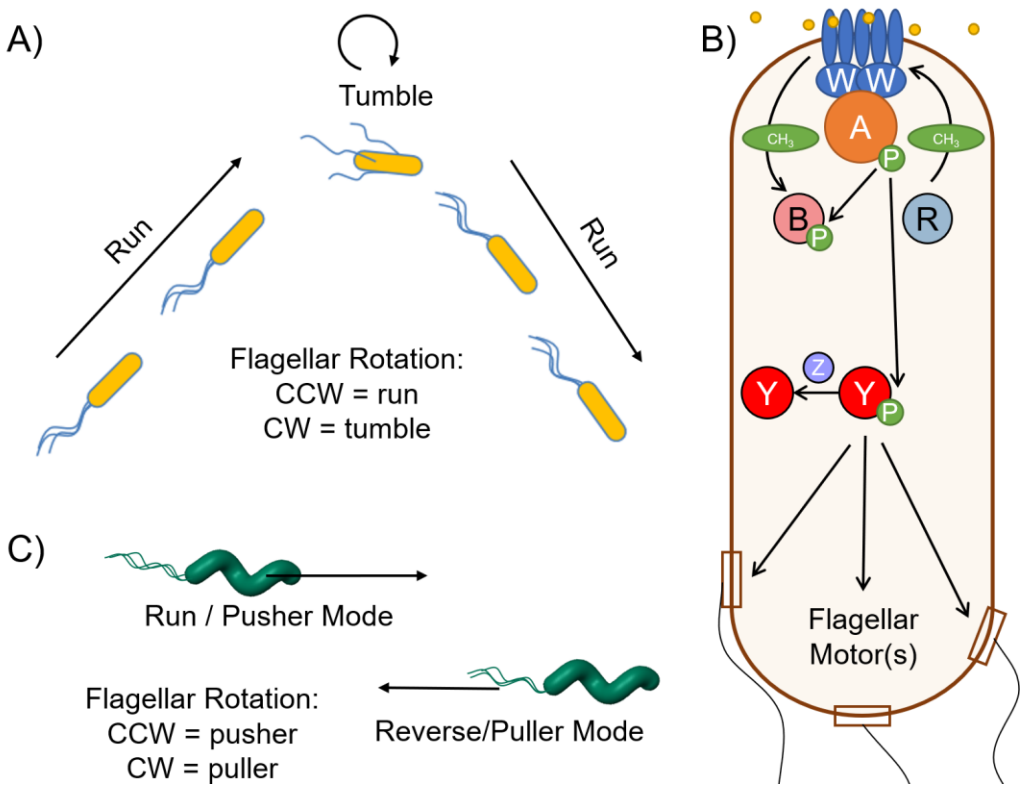

Figure 1-1. Background of bacterial motility and chemotaxis.

A) *E. coli* employs the run-tumble pattern of motility. **B)** The chemotaxis network in *E. coli*: Transmembrane chemoreceptors (blue) consist of binding pockets for different ligand molecules (yellow). Favorable molecules are called attractants and unfavorable molecules are called repellents. The chemoreceptors form stable complexes with the histidine kinase CheA (orange) through the kinase-receptor coupling factor CheW (blue). Binding of ligands (attractants/repellents) modulates chemoreceptor conformation. This conformational change is transduced via CheW and results in a change in the autophosphorylation activity of CheA. The phosphoryl group (P in green) from CheA spontaneously transfers to the response-regulator CheY (red), which is a diffusible cytoplasmic molecule. CheY, in its phosphorylated form (CheY-P), interacts with the flagellar motor to promote clockwise (CW) rotation [10]. By adjusting the fraction of time spent rotating CW, i.e., CW_{bias}, the bacterium effectively moves towards favorable environments. A phosphatase CheZ (purple) enhances the dephosphorylation rate of CheY-P, which acts as a negative controller of intracellular CheY-P

(Figure 1-1 Continued…)
concentration. In addition to signal relay to the motor through CheY-P, *E. coli* chemotaxis network is equipped with robust perfect adaptation to chemical stimuli, which allows sensing a large dynamic range of attractant or repellent concentrations. This is achieved by sustained methylation and demethylation of the receptors, which restores the receptors to their pre-stimulus activity [11]. The methyl-transferase CheR (light blue) is responsible for chemoreceptor methylation, whereas the methyl-esterase CheB (light red) is responsible for demethylation. CheR constantly methylates the chemoreceptors to set them back to the pre-stimulus conformation, whereas CheB borrows a phosphoryl group from CheA and when phosphorylated (CheB-P) catalyzes demethylation of the receptors. This helps reset the kinase activity and hence [CheY-P]. **C)** *H. pylori* employs a run-reverse pattern of motility which is different from the run-tumble pattern of *E. coli*.

The bacterial flagellum doubles up as a mechanosensor that detects cell adhesion to surfaces [12]. Flagellar sensing of surfaces helps establish biofilms, which are known to be highly resistant to external stressors such as antibiotics, fluid flows, etc. However, the molecular mechanisms by which the flagellar motor transduces surface-associated signals are unknown. Chapter 2 discusses our vision of the future breakthroughs necessary to explain the mechanisms of biofilm formation through flagellar sensing of surfaces [13]. It discusses the status quo of flagellar surface sensing and delineates the challenges in determining the precise role of the flagella in biofilm formation.

The flagellar motor includes a switch – a protein complex that can change its conformation to cause switching in the direction of rotation of the flagellum. The stator units that deliver the torque required for motor rotation are known to respond to mechanical stimuli [12, 14, 15]. In Chapter 3, I will describe our findings that show

long-range allosteric regulation of the flagellar functions by mechanosensing. Our results suggest that the stator units modulate the binding of CheY-P to the switch by modifying mechanical stresses within the rotor. Mechanosensitive regulation of CheY-P binding to the switch describes a mechanism for the communication between the external viscous load on the flagella and the chemotactic motor output.

In Chapter 4, I discuss a new technique that we developed to measure the chemotactic output in the carcinogenic pathogen, *Helicobacter pylori* [16]. Due to localization of all the flagellar motors at one cellular pole, this bacterium employs a run-reverse pattern of motility, which is different from the run-tumble motility of *E. coli* (Figure 1-1C). CCW rotation of the bundle causes *H. pylori* to run, similar to *E. coli*. As the flagella are in close proximity to each other at one pole, all the flagellar motors likely sense the same signal from the chemoreceptor. Hence, they appear to switch their rotational directions synchronously. As a result, the flagellar bundle does not come apart when the motors rotate CW. Instead, the bundle pulls the cell in the opposite direction. Owing to this run-reverse pattern of motility, the biophysical mechanisms of chemotaxis are expected to be different from the run-tumble model. We developed a novel assay that helped us circumvent some of the technical difficulties in measuring the chemotactic output in *H. pylori.* With the method, we determined the effect of a chemoattractant on the output, the CW_{bias}. We observed that the ligand decreased the bias. In the absence of CheY-P, the bias was zero. The relationship between the reversal frequency and the CW_{bias} was unimodal. Thus, *H. pylori*'s chemotaxis network appears to modulate the probability of CW rotation in otherwise CCW-rotating flagella, similar to the canonical

(*E. coli*) network. This is a surprising finding, as polar-flagellates (flagella located at one pole) tend to adopt chemotaxis strategies that are very different from those in *E. coli*, in which the flagella are uniformly spaced on the cell body.

I present the conclusions of this work in Chapter 5 and provide a broader perspective for our findings.

In Appendix C, I discuss our design of a chamber that allows mounting of sample slides normal to the focal plane on a microscope [17]. This chamber enables visualization of the cross-sections of objects without distortions prevalent in 3D confocal scans, which should prove useful for those interested in measuring the thickness of bacterial biofilms over time.

2. ROLE OF BACTERIAL FLAGELLA IN SURFACE SENSING*

2.1. Status of the field

Bacterial motility and chemotaxis are virulence factors that facilitate host invasion. Motility is predominantly mediated by rotary flagella that propel a cell through viscous bulk fluids. The chemotaxis network modulates flagellar reversals to enable the bacterium to migrate in response to chemical gradients. Together, the two processes are crucial for motile bacteria in their search for favorable niches.

Once a motile bacterium reaches a suitable surface, it may transition from its planktonic state to a surface-associated state. The mechanisms of this transition are unknown but likely involve the sensing of surface adhesion by the bacterium and subsequent signal transduction – termed surface sensing. Surface sensing promotes the development of thriving microbial communities on surfaces, such as biofilms, which are adept at withstanding several environmental stressors including antibiotics.

Surface sensing is strongly influenced by the stiffness of the semi-solid or solid surface since it controls the strength of the mechanical load on an adherent bacterium. Changes in mechanical load, which arise due to the attachment of the cell to a surface, are detected through a process termed mechanosensing [7]. Mechanosensing modulates protein structure-function to regulate a myriad of bacterial functions. Although unlikely

* This chapter is adapted with modifications from "Roadmap on emerging concepts in the physical biology of bacterial biofilms: from surface sensing to community formation" by GCL Wong, JD Antani, et al., 2021, Physical Biology, *Accepted Manuscript*.

to be the only surface sensing strategy, mechanosensing is probably a widespread phenomenon in the bacterial kingdom.

Among the known mechanosensors, the bacterial flagella are prominent [6]. The rotation of individual flagellar filaments is powered by a transmembrane motor consisting of several proteins that form a rotor complex and a torque-generating stator complex containing multiple units. Adhesion of the extracellular flagellar filament to a rigid surface obstructs the rotation of the flagellar motor. Such an increase in the mechanical resistance to rotation (also termed as an increase in the viscous load) causes remodeling of the stator complex, recruiting additional units to the stator to deliver a higher torque to the motor [12]. Such adaptation in structure and function following a viscous load-change is the hallmark of mechanosensitive processes.

The flagellar stator plays a crucial role in mechanosensing. Disrupting the stator function (torque generation) eliminates the viscous load on the motor. The loss of load (and torque) inhibits the ability of individual stator units to bind to the motor [14]. Thus, the flagellar stators are most likely the mechanosensitive components within the flagellum. Consistent with this notion, flagellar stator proteins have been implicated in surface sensing and in the formation of biofilms in a variety of bacterial species [6]. How stator remodeling triggers downstream signaling to initiate biofilm formation upon surface adhesion remains an open question.

2.2. Current and Future Challenges

The biochemical pathways triggered by the stators can be termed as mechanosensitive if the downstream effects are initiated by a change in the viscous load

on the flagella. Earlier works suggested that the obstruction of motor rotation in mono-flagellated *Vibrio parahaemolyticus* cells triggered changes in the expression of genes responsible for producing numerous lateral flagella. These lateral flagella are necessary for swarming on surfaces. Changes in gene expression associated with the lateral flagella are triggered by several types of perturbations: growth on solid surfaces, suspension in media with high viscosities, as well as the agglutination of cells with the aid of flagellar antibodies [18]. Although the flagellar viscous loads are likely elevated by each of these perturbations, the magnitudes of load-changes vary drastically between them. In general, there is a lack of information about the correlation between the magnitudes of load-changes and the physiological response – in this example, the expression of lateral flagella. Determining the magnitudes of viscous load-changes needed to trigger biochemical signaling will be important in the future to explain the role of flagellar mechanosensing in signaling.

In contrast, flagellar-mediation of surface sensing in *Caulobacter crescentus* merely requires the presence of functional stator and rotor proteins; the extracellular components of the flagellum are not necessary [19]. In the absence of extracellular flagellar components, no load changes are possible. Hence, mechanosensing is precluded. This suggests that the signal that activates flagellar-mediated biochemical signaling may not always be a viscous load-change [7]. Accurately identifying the signals that activate the flagellar stators at a surface will be crucial to constrain the models of flagellar-mediated surface sensing.

A swimming bacterium experiences a constant viscous drag that is proportional to its speed. The inhibition of flagellar rotation due to surface attachment not only perturbs flagellar activity but it also reduces the drag on the cell body by eliminating motility. Due to the coupling of flagellar functions and motility, it is not straightforward to determine if it is the loss of flagellar functions or the concomitant reduction in the viscous drag on the cell that triggers downstream effects. A case in point is the regulation of K-state transition in *Bacillus subtilis*, which regulates natural competence. The transition probabilities were found to be correlated with the viscous loads on the flagella [20]. However, the alterations in the viscous loads also inhibited motility. It is possible that the reduction in the drag triggered mechanosensors on the cell body to regulate K-state transition probabilities, independent of the flagella. Discriminating between these two mechanisms is a significant challenge.

Bacteria produce different types of chemical entities, including metabolites such as indole and molecules involved in quorum-sensing such as autoinducers [21]. Although swimming bacteria cannot outrun small diffusible chemical stimulants [22], motility does ensure that the local concentrations of the endogenously-produced chemical signals around the cell will be lower relative to the concentrations around immobilized cells. If the chemical signal is very slow to diffuse and the cell is highly sensitive to small differences in the signal levels, downstream signaling could be initiated through the build-up of higher local concentrations of the chemical species. Distinguishing between phenomena triggered by chemical sensing and those due to surface sensing is a future challenge.

2.3. Advances in Science and Technology to Meet Challenges

The load on the flagellar motor increases significantly only if the cell-filament attachment to the surface meets specific criteria [7]. Hence, visualizing how the flagella interact with the surface is necessary to obtain important insights regarding the magnitudes of load-changes and whether the flagella indeed trigger downstream effects. This is often ignored in studies on surface sensing.

Growth on surfaces may result in multiple activation signals and subsequent downstream effects may or may not arise due to flagellar sensing alone. To address this, cells could be suspended in media of high viscosities to increase the viscous loads on the flagella. The limitation of this approach is the weak dependence of loads on medium viscosities [12]. A better approach, in some cases, is to stall the flagellar motors – which causes the maximum possible load-change – by linking filaments together with anti-flagellin antibodies in the bulk fluid [18]. This technique enables flagellar stalling but only in the case of peritrichous cells. This is because locking the flagella belonging to the same cell eliminates all possible rotational degrees of freedom for the motors. In the case of monotrichous bacteria such as *V. parahaemolyticus*, *C. crescentus*, or *Pseudomonas aeruginosa*, the antibody approach fails to stall the motors as the cell bodies freely rotate along their principal axes (Figure 2-1). Advances in the methods to load the flagella, for example with optical traps [12], in monotrichous bacterial species in the bulk fluid will be critical in delineating the role of the flagella in initiating intracellular signaling.

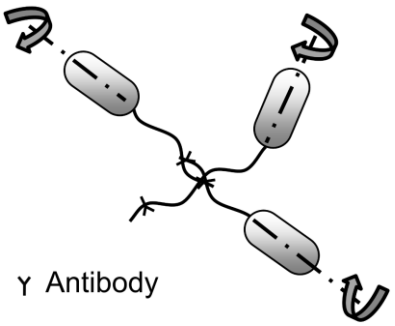

Figure 2-1. Linking of flagella on multiple singly flagellated (monotrichous) cells with antibodies fails to stall the motors as the cell bodies are free to rotate.
Reprinted with permission from [13].

Genetic modification is a standard approach to determine the role of a particular enzyme in bacterial functions. However, the deletion of a flagellar gene typically inhibits motility, causing several types of stimuli to act on the bacterium at once. In the presence of multiple activating signals, observations can become challenging to interpret. Advances are needed in mechanical stimulation techniques to apply a single type of stimulus. Combining such techniques with dynamic gene perturbation methods [23] is anticipated to reveal bacterial adaptations that may occur following surface adhesion; these are likely to be missed in current approaches that tend to focus on the steady-state responses to the loss of enzymatic function. In particular, measurements of the dynamics of surface adaptation are expected to provide information about the direct as well as indirect interactions in the gene regulatory networks that regulate the transition to the surface-associated states.

2.4. Concluding Remarks

The bacterial flagellum was historically viewed as an apparatus that enables

motility. New research has expanded that view by identifying a role for the flagella in surface sensing and other related phenomena. As discussed, several challenges exist in determining the molecular mechanisms by which flagella trigger the transition from planktonic to surface-associated states. Advances in genetic engineering, microscopy, and mechanical stimulation techniques will be necessary to address some of those challenges.

3. LONG-RANGE REGULATION OF FLAGELLAR ALLOSTERIC INTERACTIONS BY MECHANICAL FORCES

3.1. Introduction: Proprioception in the bacterial flagellar motor

One typically thinks of proprioception in the context of the feedback between mechanosensory neurons located within muscles, tendons, and joints and the central nervous system, which enables an organism to sense its position and movement [24, 25]. For example, the campaniform sensilla in insects provide sensory feedback in response to stresses felt at the joints of the tarsal segments. This feedback allows the insect to regulate the activity of the motor neurons that enervate the leg muscles to maintain its posture and its grip on the substrate when it walks on the floor or the ceiling [26]. In addition to animals, proprioceptive feedback has been described in plants [27, 28]. Here, we report a simple form of bacterial proprioception that enables a cell to adapt to changes in the mechanical forces acting on it by fine-tuning its sensitivity to extracellular stimuli.

E. coli swim by rotating helical flagellar filaments with the aid of transmembrane flagellar motors. The flagellar motor consists of a stator and a rotor. The stator is made up of several independent stator units, with each unit capable of rotating the motor. The rotor is a multimeric complex of several different types of proteins [29]. The chemotaxis response regulator, CheY-P, binds cooperatively to the cytoplasmic interface (C-ring) of the motor to increase the probability of clockwise (CW) rotation in an otherwise counterclockwise (CCW) rotating motor [30]. This switch output is called the CW_{bias}. Modulation of the CW_{bias} is the basis for chemotaxis – the migration toward favorable

chemical environments. The chemotaxis network modulates the CW_{bias} in response to chemical stimuli by controlling the level of CheY-P.

The basal CW_{bias} must be maintained within its dynamic range ($0 < CW_{bias} < 1$) for chemotaxis: cells of *E. coli* in which the motors remain locked in the CCW ($CW_{bias} = 0$) or the CW ($CW_{bias} = 1$) direction fail to respond to chemical stimuli [31]. We previously showed that a sudden increase in the viscous load on the motor inhibits switching, causing it to rotate exclusively CCW [12]. Within a few minutes, the motor recruits additional stator units, which increases the torque delivered to the motor. During this time, the switch adapts to a steady-state CW_{bias} independent of the chemotaxis network. The role of mechanosensitive stator recruitment in the adaptation in CW_{bias} is not understood.

Here, we investigated whether mechanosensitive stator recruitment influences the interactions of CheY-P with the C-ring, a complex structure that contains three proteins – FliG, FliM, and FliN [32]. We discovered that more CheY-P binds to the C-ring when more stator units bind to the motor in response to increased torque. However, neither recruitment of more FliM, as has been seen in response to chemotaxis signals [33], nor changes in the proton flux that powers motor rotation, was responsible for the changes in CheY-P binding affinity. Instead, our data is consistent with a mechanism in which increased mechanical stress generated by the stator units on the $FliG_C$ domain regulates CheY-P binding to $FliM_N$/FliN. This mechanism enables the cell to adapt its basal CW_{bias} precisely, which helps fine-tune the motor sensitivity such that the cell is able to respond to chemical stimuli over a range of viscous loads. We suggest that this process

is functionally analogous to, although mechanistically completely distinct from, the proprioceptive feedback that controls the neuromuscular circuitry in animals.

3.2. Results

3.2.1. Mechanosensitive stator recruitment modulates CheY-P binding

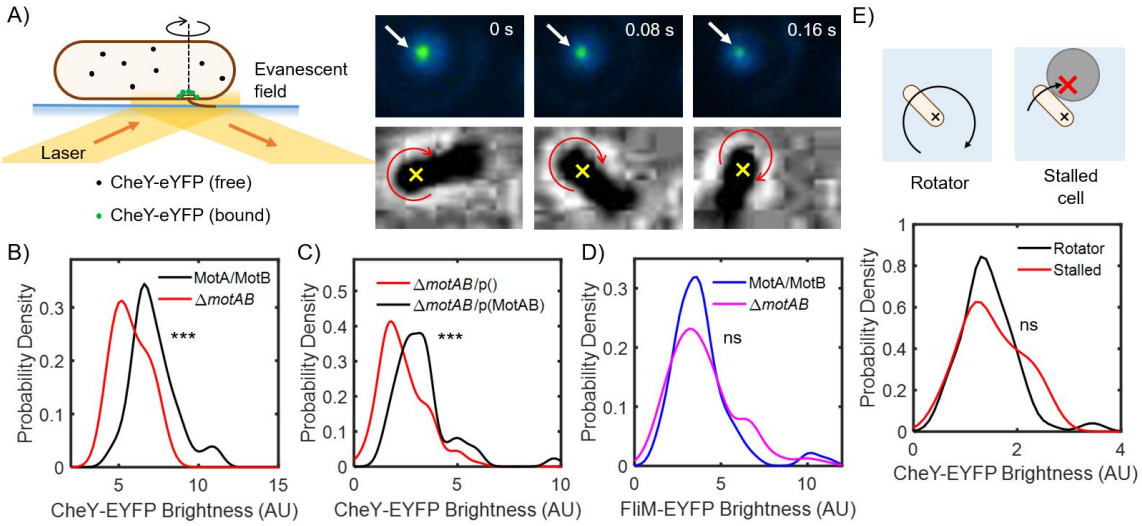

Figure 3-1. CheY-binding to the motor increases with the number of bound stator units. **A)** We monitored the rotation of tethered cells simultaneously in the TIRF and the phase channels. The fluorescent moieties (CheY-EYFP) were visible in the evanescent field as they bound to the motor: The top row shows a time series of TIRF images for a single tethered cell. The arrow points to CheY-P bound to the motor. The corresponding phase contrast images are shown in the bottom row. The × shows the point of tethering around which the cell rotates. **B)** The intensity of the localized CheY-P around each motor was quantitatively estimated from the TIRF images (see *Materials and Methods*, section 3.4). The probability-density estimates are indicated for a strain carrying functional stators (MotA/MotB strain, black curve, n = 50 motors) and a strain lacking stator proteins (Δ*motAB* strain, red curve, n = 48 motors). The difference in the mean intensities in the two strains was significant (Paired *t*-test, ***p-value < 0.001). The mean number of CheY-P molecules bound to the motor in the absence of stator units was lower than that in the presence of stators units. **C)** We compared CheY-EYFP binding to the motors in

(Figure 3-1 Continued…)
the Δ*motAB* strain transformed with a plasmid encoding *motA-motB* with that in a Δ*motAB* strain transformed with an empty plasmid. The strain lacking MotA-MotB (red curve, n = 106 motors) had significantly lower intensities (***p-value < 0.001) than the strain expressing MotA-MotB (black curve, n = 46 motors). **D)** We measured the localization of FliM-EYFP in each tethered cell. The difference in the mean intensities in the motors of a strain carrying functional stators (blue curve, n = 95 motors) and a strain lacking stator proteins (magenta curve, n = 131 motors) was not statistically significant (ns, p-value > 0.05). **E)** Tethered cells were stalled by obstructing the rotation with optically trapped beads. The difference in the mean CheY-EYFP intensities in rotating cells (black curve, n = 86 cells) and stalled cells (red curve, n = 36 cells) was not statistically significant (ns, p-value > 0.05).

We employed the tethered cell assay to determine whether mechanosensitive stator recruitment modulated the interactions of CheY-P with the C-ring (Figure 3-1A). We worked with a Δ*cheRcheBcheYcheZ* strain, called the MotA/MotB strain hereafter, and transformed it with a *ptrc99A* vector encoding *cheY* fused with *eyfp* (see *Materials and Methods*, section 3.4). The CheY-EYFP fusion is functional and induces switching in the motors in the absence of native CheY [34]. The viscous load on the motor in a tethered cell is significant (~ 150 pN.nm.s), and the high resistance to rotation causes the motor to recruit a full complement of ~11 stator units in ~ 5 min [14]. Hence, we waited 10 min after tethering to allow stator recruitment to complete. Next, cells were excited with a 514 nm laser in the TIRF mode to visualize CheY-EYFP localization around each tethered motor, and the fluorescence signals were recorded with an EMCCD camera (Figure 3-1A). Simultaneous recording of cell rotation in the phase-contrast channel helped locate precisely the tether around which the cell body rotated. Mapping the

spatial coordinates in the phase-contrast images onto the TIRF images allowed us to locate each motor accurately in the TIRF channel. As we recorded a time-series in the TIRF channel, cell rotation was also visible in the TIRF images. This enabled us to confirm the motor location independently in the TIRF channel (see *Materials and Methods*, section 3.4).

We employed custom-written algorithms to quantify the intensity of the fluorescent punctum in each tethered cell [14]. Briefly, we corrected for the background fluorescence and determined the total pixel intensities within a 350 nm mask placed around each motor (see *Materials and Methods*, section 3.4). The total intensity of each punctum at the point of the tether indicated the total number of fluorophores bound to the motor [35]. The mask ensured that we did not include neighboring fluorescent moieties when calculating the intensities. The probability density estimates for the intensities obtained from n = 50 motors are indicated in Figure 3-1B.

Each stator unit is made up of five MotA subunits and two MotB subunits [36, 37]. A stator-less motor was generated by deleting Δ*motAmotB* from the MotA/MotB strain. We visualized CheY-EYFP localization in tethered cells of this strain to determine how the absence of stator units affected CheY-P interactions with the motors. In the absence of stators, tethered cells diffused rotationally. To identify the point of tether, we forced the cells to rotate with hydrodynamic flows and recorded their movements in the phase channel. We did this by turning the flow of motility buffer into the perfusion chamber on and off several times. Each time, the non-motile cells that were tethered by their flagella rotated to align with the direction of the flow. Those that

were stuck to the surface did not move. With this approach, we could reliably distinguish between the cells that were tethered by their flagellar stubs and those that merely adhered to the surface. We recorded the forced rotation of the cell, which allowed the point of tether to be quantified from the phase-contrast data for each cell. The probability-density estimates of CheY-EYFP localization at the motors in the Δ*motAmotB* strain are shown in Figure 3-1B. As can be seen, more CheY-EYFP molecules bound to motors that rotated with a full complement of stator units relative to the motors of non-motile cells that lacked stators.

Next, we determined whether the differences observed in CheY binding in the two strains in Figure 3-1B could be attributed to differences in the phosphorylation levels of CheY, to differences in the activity of the chemotaxis kinase CheA, or to some other unknown effects. We transformed the Δ*motAmotB* strain with a *pBAD34* vector encoding *motAmotB*, in which the production of MotA-B is inducible with arabinose [38]. This plasmid is compatible with the *ptrc99A* plasmid. This yielded the Δ*motAmotB*/p(MotAMotB) strain (see *Materials and Methods*, section 3.4). A control strain was prepared by transforming the Δ*motAmotB* strain with an empty *pBAD* plasmid, which yielded the Δ*motAmotB*/p() strain. We repeated our measurements of CheY-P binding to motors in these two strains, using the protocols described previously. As seen in Figure 3-1C, CheY-P molecules bound to the motor in greater numbers when the stator proteins were expressed than when they were absent. We conclude that the remodeling of the stator promotes CheY-P binding to the motor.

3.2.2. The FliM ring does not remodel when stator units are recruited

The FliM complex is capable of remodeling by recruiting FliM subunits to adapt to variations in CheY-P levels caused by strong chemoattractants [33, 35]. We thus asked whether mechanosensitive stator recruitment causes recruitment of additional FliM, thereby increasing CheY-P binding. We performed TIRF measurements to compare the number of FliM-EYFP subunits in individual motors in the presence and absence of the stator units. We employed a *ΔcheY strain* that carries a *fliM-eyfp-fliM* allele in place of the chromosomal *fliM* gene (see *Materials and Methods*, section 3.4). The fusion is functional and does not interfere with motor function [39]. We compared the FliM-EYFP intensities in tethered cells of this strain and in cells of a strain deleted for *motAmotB*, using the protocols discussed in previous sections. The absence of CheY locked the rotation of the motors in the CCW-only direction, ensuring that changes in the direction of rotation did not contribute to FliM remodeling [35]. As shown in Figure 3-1D, the difference in the mean fluorescence intensities in the two strains was not significant ($p > 0.05$). Thus, the number of FliM subunits in the motor did not change with the number of bound stator units. The similarity in the intensities in the presence and the absence of the stator also ruled out the possibility that the intensity of individual YFP molecules was somehow different in the presence and absence of MotAB. These data suggested that the affinity of CheY-P for FliM increases with the number of stator units bound to the motor.

3.2.3. CheY-P binding does not depend on proton flux or motor rotation

Flagellar rotation is powered by the proton motive force – the flux of protons through the stator from the periplasm into the cytoplasm yields the free energy required to rotate the motor [40]. Stator recruitment increases the flux of protons. We explored whether the increased proton flux influences the affinity of CheY-P for FliM. To do this, we compared CheY-P binding in rotating and stalled motors. Stalled motors retain a full complement of bound stator units [15]. However, the proton flux is expected to sharply decrease as rotation is impeded.

We tethered cells of the MotA/MotB strain as before and provided adequate time for stator remodeling. Next, we optically trapped large latex beads (4.5 μm diameter) or floating cells and placed them in the path of each rotating cell to obstruct rotation (Movie S1). After 2 min, we imaged CheY-EYFP localized at the motors in the stalled cells and quantified the intensities. We compared these intensities with those observed at the motors in tethered cells in the vicinity that rotated freely. There was no significant difference in the mean CheY-EYFP intensities in the stalled and rotating motors (Figure 3-1E). This result suggests that the reduced affinity of CheY-P for FliM in the absence of stators was not due to the lack of proton flux or motor rotation. Instead, it is likely that mechanical force regulates CheY-P binding as torque on FliG increases with an increasing number of bound stator units when the motor rotates under a high viscous load [41].

3.2.4. Mechanosensitive stator recruitment promotes CW rotation

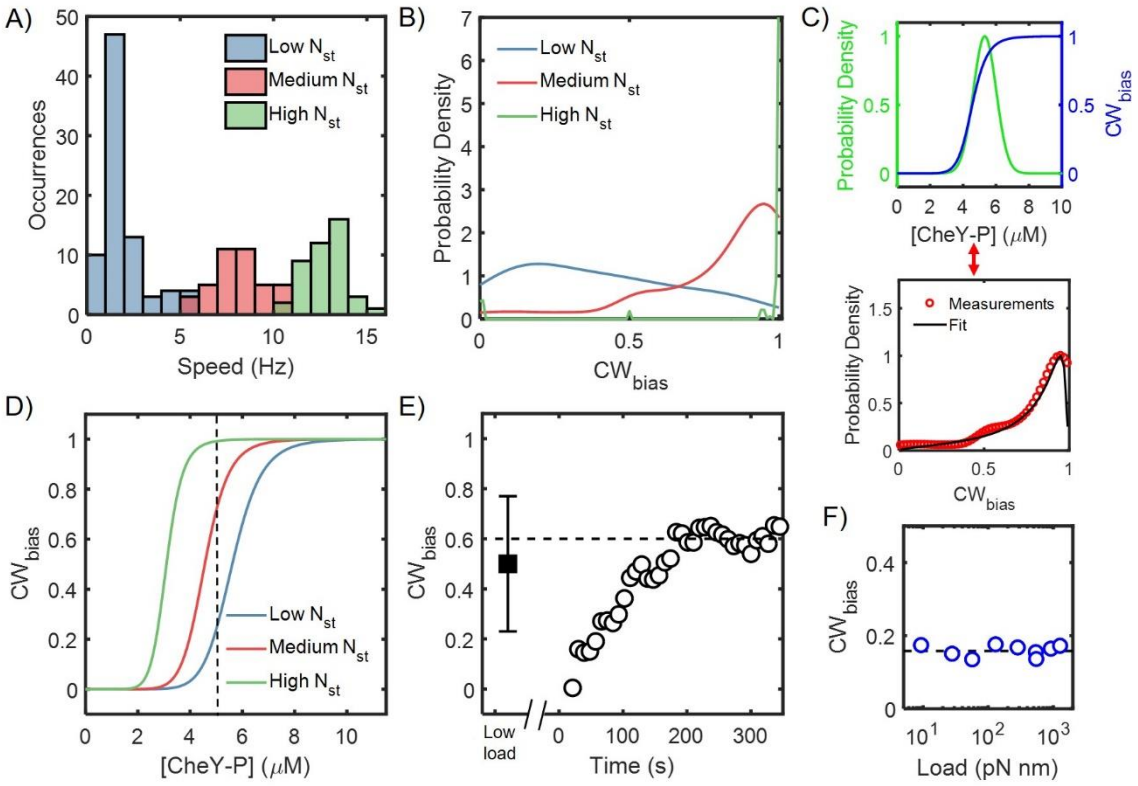

Figure 3-2. Motor response curves shift with the number of bound stator units.
A) The number of stator units bound to individual motors was varied by controlling the expression of MotA-MotB from an inducible plasmid-borne promoter (see *Materials and Methods*, section 3.4). We probed motor rotation with 2 μm beads (high viscous load). Data on a total of n = 165 motors were collected and binned into three groups as per the speed of rotation, as indicated by the different colors: low speeds (n= 81 motors, average torque ~ 270 pN.nm), medium speeds (n= 40 motors, average torque ~ 1150 pN.nm), and high speeds (n= 44 motors, average torque ~ 1800 pN.nm). Each stator unit adds ~ 1.1-1.3 Hz to the overall rotation speed. **B)** The probability density for the CW_{bias} is indicated for each speed group. The distribution shifted to increased CW_{bias} with an increasing number of bound stator units (N_{st}). **C)** *Top:* The variation in the CheY-P levels in a population (green curve) was described by a normal distribution (μ =

(Figure 3-2 Continued…)

5.3 ± 0.5 μM, σ/μ = 0.13). The CW_{bias} versus CheY-P relationship is described by a Hill equation (blue curve) parameterized by the Hill coefficient h and the dissociation constant K_D. Together, these relationships provide an equation for the distribution of CW_{bias} (see Appendix A.2). *Bottom:* The value of K_D for each N_{st} group was calculated from a least-square fit of the analytical CW_{bias} distribution (black curve) to the corresponding experimental data (symbols). We assumed a constant h = 10 [4]. **D)** The CW_{bias} versus CheY-P curves calculated from the fitted K_D values are shown. The curves shift left with increasing N_{st} (the number of stator units bound to the motor). At a representative [CheY-P] = 5 μM (dashed black line), the CW_{bias} = 0.24, 0.71, and 0.99 for low, medium, and high N_{st}, respectively. **E)** The mean CW_{bias} at low viscous load was measured to be 0.5 ± 0.27 (solid square) in a *ΔcheRcheB* strain by monitoring the rotation of 300 nm beads. The standard deviation is indicated. The post-stimulus data (open circles) from ref. [12] shows the adaptation in CW_{bias} when the load is suddenly increased by tethering a cell (at t = 0 s). **F)** The steady-state CW_{bias} for wild-type cells, calculated from the transition rates between CW-CCW directions of rotation [42, 43], is indicated as a function of load.

To determine the functional consequences of the mechanosensitive binding of CheY-P, we measured the CW_{bias} in cells when the torque was differentially controlled by varying the number of stator units bound to the motor (N_{st}). We employed a Δ*motA-motB* strain of *E. coli* transformed with the pBAD34-*motAmotB* plasmid. The strain also lacks chromosomal alleles for the methyltransferase (CheR), methylesterase (CheB), and the phosphatase (CheZ), which ensures a high level of phosphorylated CheY in the cell. Using this strain allowed us to measure variations in the CW_{bias} over its full dynamic range (0 to 1). We attached 2 μm beads to individual flagella and waited an adequate time (~ 10 min) for mechanosensitive stator recruitment to complete (see *Materials and*

Methods, section 3.4). At steady state under a high viscous load (for example, a 2 μm bead or a tethered cell), the motor contains ~ 8 – 11 stator units in a wild-type cell [41]. However, by carefully limiting the production of MotA-MotB proteins, we could generate motors containing anywhere from 1 to 11 stator units.

We measured the rotational speeds of a total of n = 165 motors over the different induction levels, as described in *Materials and Methods* (section 3.4). We estimated the N_{st} for each motor by dividing the average speed by 1.3 Hz, which is the approximate increment in the rotational speed when a single stator unit is added to the stator [41]. We binned the data into three groups: a low N_{st} group consisting of 1-4 stator units, a medium N_{st} group consisting of 5-8 units, and a high N_{st} group (> 8 units). The distributions of speeds for the three groups are indicated in Figure 3-2A. The CheY-P levels vary significantly from cell to cell in the Δ*cheRcheBcheZ* strain, which causes the CW_{bias} values to be widely distributed over a population of cells [44]. We measured the distributions of the steady-state CW_{bias} in each group. Figure 3-2B shows the kernel-density estimates for the CW_{bias} distributions; the raw data are available in the Appendix A Figure 1. The CW_{bias} was distributed predominantly at ~ 1 at high N_{st} (>8 stator units, average torque ~ 1800 pN.nm). For a medium N_{st} (5-8 stator units, average torque ~ 1150 pN.nm), the average bias was lower (0.8 ± 0.04). At the lowest N_{st} (1-4 stator units, mean torque ~ 270 pN.nm), the average CW_{bias} dropped to 0.4 ± 0.04. Thus, variations in the motor torque modified the distributions of the CW_{bias} in populations of cells.

3.2.5. Mechanosensitive stator recruitment tunes motor sensitivity

Next, we quantified how torque modulates the dependence of the CWbias on

CheY-P levels from the distributions of the CW_{bias} in Figure 3-2B. The CW_{bias} vs [CheY-P] relationship is well described by the Hill equation [4, 44]. As the intracellular CheY-P levels are independent of the number of stator units, the variations in the CW_{bias} distributions for the different torque values (Figure 3-2B) arise entirely due to changes in the CW_{bias} vs. CheY-P relationship with the number of stator units bound to the motor.

To determine how the CW_{bias} vs. CheY-P relationship depends on torque, we derived an analytical expression for the distribution of the CW_{bias} in a population of cells, following our previous work [44]. To do this, we assumed a normal distribution of CheY-P with a mean μ and a spread of σ**.** We combined the distribution with the Hill equation that describes the CW_{bias} versus CheY-P relationship (Figure 3-2C) to yield an analytical form for the CW_{bias} distribution in a population of cells (see equation 1 in Appendix A.2). We first fitted the equation to the CW_{bias} distribution for the high torque (high N_{st}) group in Figure 3-2B, with μ as a free parameter. We assumed $\sigma = 0.13\,\mu$, a Hill coefficient value (h) = 10, and a dissociation constant value (K_D) = 3.1 μM based on previous studies [4, 44]. A nonlinear least-square fit yielded μ = 5.3 ± 0.5 μM for the *ΔcheRcheBcheZ* strain, which is reasonable given the higher levels of CheY-P phosphorylation in this strain compared to the wild type. Next, we assumed the same values of μ and σ for the remaining N_{st} groups, as the distribution of [CheY-P] is not expected to depend on the number of stator units. Nonlinear least-square fitting with K_D as a free parameter yielded K_D = 4.5 ± 0.0 for medium torque (medium Nst) and = 5.6 ± 0.0 for low torque (low N_{st}), see Appendix A Table 1. The dissociation constant K_D for

the CheY-P/motor interaction thus decreased with increasing torque, contrary to a recent prediction [45].

The predicted CW_{bias} versus CheY-P relationships obtained from the fitted K_D are shown in Figure 3-2D. The curves shift leftward as the motor recruits more stator units following a load increase. The high N_{st} case (green curve) correctly represents the CW-only rotation of motors with a full complement of stator units (Figure 3-2A). The K_D is highest for the case of lowest torque (~ 270 pN.nm). The shift in motor response curves with increasing torque indicates that the CW_{bias} increases as more stator units are recruited. This explains our previous observation of adaptation in the CW_{bias} during the mechanosensitive recruitment of stator units in wild-type and Δ*cheRcheB* cells [12]. The adaptation in a Δ*cheRcheB* strain is reproduced in Figure 3-2E, where the stimulus was applied at t = 0 s. To determine the pre-stimulus CW_{bias}, we measured the average CW_{bias} at low loads by measuring the rotation of 300 nm beads in the Δ*cheRcheB* strain. As is evident in Figure 3-2E (t < 0 s), the pre-stimulus and post-stimulus CW_{bias} is similar, which suggests that the CW_{bias} first decreases upon a load increase and then precisely adapts to the pre-stimulus level. This is analogous to the precise adaptation in the CW_{bias} in response to chemical stimuli [46].

The data in Figure 3-2E suggest that the basal or steady-state CW_{bias} should remain approximately constant irrespective of the viscous load. To test this, we calculated the CW_{bias} for wild-type cells from previous studies that reported the transition frequencies for CW-to-CCW and CCW-to-CW reversals over a range of loads (see Appendix A.3 and [42, 43]). Our calculations indicated that the CW_{bias} in the wild

type was indeed independent of the viscous load (Figure 3-2F). Thus, the torque-mediated interplay between stator recruitment and the mechanosensitive CheY-P binding ensures that the dynamic range of the motor is never exceeded, even when the viscous load changes. This adaptation likely facilitates chemotaxis even when the viscosity of the medium changes dramatically.

3.3. Discussion

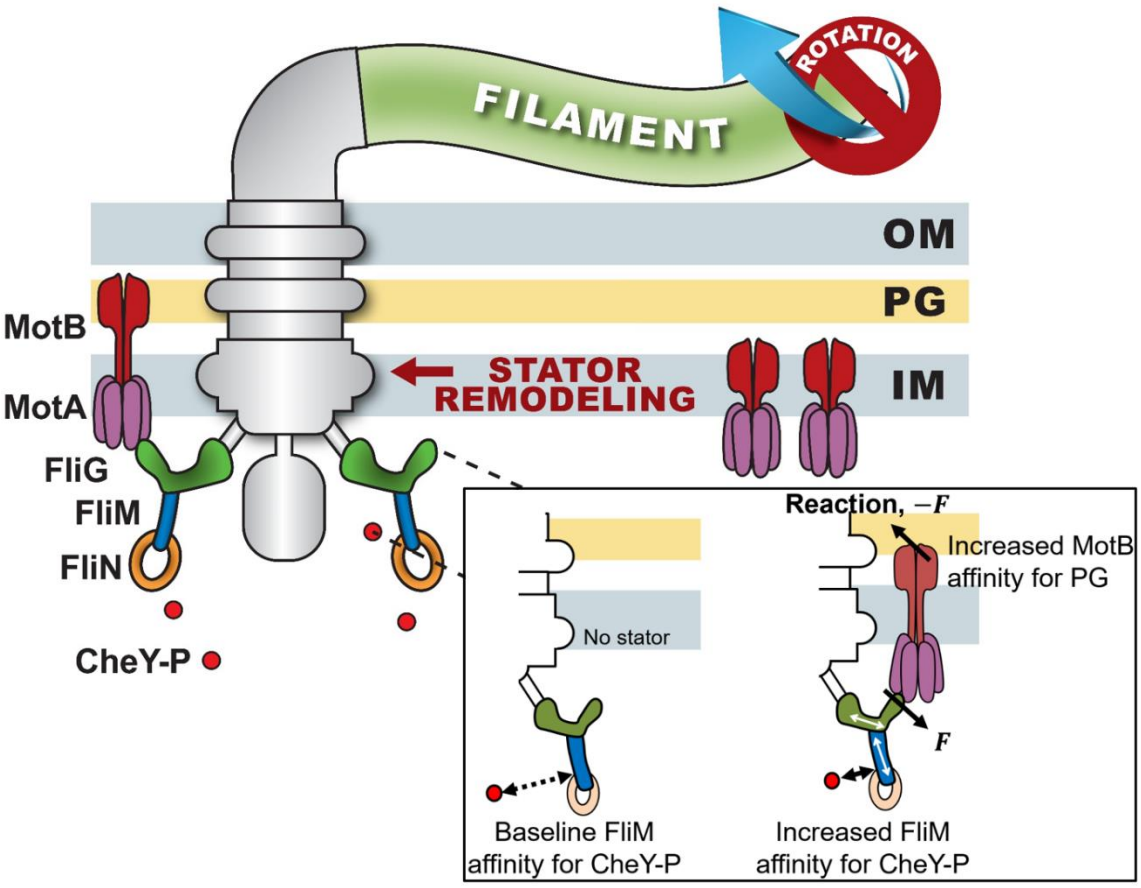

Figure 3-3. Model for proprioceptive control in the flagellar motor.
Independent stator units (MotA/MotB, purple/maroon units) deliver torque to the FliG ring (green) to rotate the transmembrane flagellar motor. The conformational state of the FliG ring determines the direction of rotation. The default conformation is CCW;

(Figure 3-3 Continued…)
binding of CheY-P to the FliM (blue) and FliN (orange) complexes increases the probability that the FliG ring will adopt a CW conformation. An increase in the viscous resistance to the rotation of the extracellular flagellar filament causes the transmembrane flagellar motor to recruit additional stator units. **Inset**: *Left*: In the absence of stator units, the affinity CheY-P binding is at a baseline level. *Right*: Increased mechanical force (F) on the $FliG_C$ domain due to the mechanosensitive recruitment of a stator unit induces conformational shifts (white arrows) in FliM/FliN, increasing their affinity for CheY-P . An equal and opposite force ($-F$) strengthens the association of the peptidoglycan and the peptidoglycan-binding domain of MotB, increasing the dwell time of the stator unit at the motor [14]. The torque-mediated increase in CheY-P affinity compensates for the increased resistance to changes in the conformation of the FliG ring, thereby maintaining a constant motor sensitivity (basal CW_{bias}).

Our measurements suggested that there was no significant difference in CheY-P binding to rotating motors relative to motors that were stalled with optical traps (Figure 3-1E). Although it is possible that some protons leak through the stator in a stalled motor, the high duty ratio under high viscous loads ensures that the proton flux through a stalled motor is very low. The recent model for stator function by rotation of the MotA pentamer of a stator unit around a centrally located MotB dimer, which is held stationary by attachment to the cell wall, also predicts that stator units in a stalled motor will not conduct ions subunits [36, 37]. Thus, our data suggest that the increased proton flux during the mechanosensitive recruitment of stator units does not influence CheY-P binding. Instead, the torque (force) delivered by the stator to the rotor likely modulates CheY-P binding.

Each stator unit increases the total force it delivers to a FliG subunit from ~ 0.5 pN at very low loads to ~ 10 pN at high viscous loads [12]. In a stator with a full complement of 11 stator units, this corresponds to an increase of ~ 110 pN over the FliG ring. In previous work, we showed that the increased torque delivered by each stator unit following the adhesion of the flagellum to a surface is the basis for mechanosensitive stator recruitment [14]. As the force delivered by MotA to FliG causes an equal and opposite force where MotB anchors to the cell wall, the increased torque strengthens its interactions with the peptidoglycan-binding domain of MotB (Figure 3-3**)**.

Here, we propose that the force felt by the C-terminal domain of a FliG subunit is transmitted to the FliM subunit. These conformational shifts increase the affinity of the N segment of FliM, which lies ~ 15 nm away from the C-terminal domain of FliG, for CheY-P (Figure 3-3**)**. When the force is weaker, as at very low viscous loads [47], or when no stator units are present, these allosteric conformational changes do not occur. The affinity for CheY-P increases when the torque increases: K_D decreases by ~ 2.5 μM with an increase in torque of ~ 1530 pN.nm (Figure 3-2D). This increased affinity for CheY-P, coupled with the cooperativity in CheY-P binding and the ultrasensitive motor response curve, causes a major change in CW_{bias} (Figure 3-2D).

Our previous results indicated that when the load on a motor rotated by a single stator unit suddenly increases, the motor rotates exclusively CCW [12]. We propose that the increased torque delivered by the single stator unit physically obstructs the FliG subunit from undergoing a change to the CW conformation. This is consistent with a recent model that assumes that torque increases the difference in free energy (ΔG_{CCW-CW})

between the CCW conformation and the higher-energy CW conformation of the FliG ring [45]. However, contrary to that model, we observed that the K_D decreases as new stator units are recruited and the torque increases further. The resultant increase in the affinity of FliM for CheY-P compensates for the elevated ΔG_{CCW-CW}. This enables the CW_{bias} to adapt precisely to mechanical stimuli: the pre-stimulus and post-stimulus values of the CW_{bias} are similar (Figure 3-2E). Precise adaptation maintains a constant basal CW_{bias} over varying viscous conditions in the wild type (Figure 3-2F).

Although receptor-mediated adaptation is capable of adjusting CheY-P levels so that the operating point (basal CW_{bias}) remains within the dynamic range of the response ($0 < CW_{bias} < 1$), the chemotaxis network is insensitive to changes in the viscous load on the flagella [48]. Instead, mechanosensitive stator recruitment maintains the motor within the operational dynamic range over different loads by modulating CheY-P binding. This homeostasis in basal chemotactic function is critical for maintaining sensitivity to chemical signals over a wide range of viscous conditions, enabling cells to navigate heterogeneous environments with varying viscosities. In bacteria in which flagellar motors contain constant numbers of stator units, such as *Helicobacter pylori* [49], load-dependent stresses may still tune the affinity of FliM for CheY-P. Future research will be required to test this possibility.

In addition to chemotaxis, an intermediate value of the CW_{bias} ($0 < CW_{bias} < 1$) is necessary for inducing bacterial swarming [50], a surface-associated form of group motility [51]. The mechanosensitive binding of CheY-P to FliM may enable the cell to adapt to the increased viscous drag near a surface, thereby helping in the transition from

a planktonic state to the surface-associated swarmer state. Mechanosensitive CheY-P binding may also prevent swimmers from becoming hydrodynamically trapped at surfaces, as exclusively smooth-swimming cells are, by inducing tumbles [52].

There are striking similarities between the phenomena discussed in this work and proprioceptive feedback observed in animals and plants. Similar to the mammalian proprioreceptors, golgi tendon organs, the flagellar motor encodes load as viscous resistance to motion. The load-induced mechanical stress within the flagellar motor generates an allosteric effect that increases the affinity of FliM for CheY-P. This enables the motor to fine-tune its operating point (basal CW_{bias}) to maximize its sensitivity to chemical stimuli over a range of viscous conditions. The resetting of the CW_{bias} accomplishes similar outcomes as those achieved by the proprioceptive feedback in neuromuscular systems: the load imposed on the output of the system modulates motor behavior to maintain maximal sensitivity to novel external stimuli [24, 25]. Finally, proprioception enables the flagellar motor to relay key information to the cell regarding its position in space: whether it is swimming (medium viscous loads) or stuck to a surface (high viscous load). Proprioception in bacteria is thus likely to play a key role in surface-sensing pathways.

3.4. Materials and Methods

3.4.1. Strains and Plasmids

All strains are derivatives of *Escherichia coli* RP437. They carry a sticky variant (*fliC*st) of the flagellin gene, which allows cells to be tethered to glass surfaces and to latex beads via their flagellar filaments. Chromosomal modifications were achieved with

the λ-red mediated homologous recombination technique [38]. We employed two compatible vectors for controlling the expression of proteins: pTrc99A encodes resistance to ampicillin and pBAD34 encodes resistance to chloramphenicol. Strains and plasmids are listed in Appendix A.6.

3.4.2. Cell Culture

We grew overnight cultures in TB (tryptone broth) at 30°C from colonies freshly streaked on solid media plates (LB agar), supplemented with antibiotics when appropriate (100 μg/mL ampicillin, 25 μg/mL chloramphenicol). We grew day cultures by diluting overnight cultures in fresh 10 mL TB at 33°C in a shaking incubator set at 170 RPM. The cultures were supplemented with ampicillin (100 μg/mL) and chloramphenicol (25 μg/mL), as appropriate. To induce expression from the *ptrc99A-cheY-eyfp* plasmid, we added 15 μM isopropyl-β-D-thiogalactoside (IPTG) to the day cultures. To vary the expression from the *pBAD34-motA-motB* plasmid, we added 1×10^{-5} to 6×10^{-5} % L-arabinose to the day culture.

3.4.3. Tethered Cell Assays

Upon reaching an OD_{600} ~ 0.5-0.6, the day culture was washed twice with motility buffer (MB: 0.01 M potassium phosphate, 0.067 M NaCl, 0.1 mM EDTA, 1 μM methionine, 10 mM lactic acid). The cell pellet obtained from the wash cycles was resuspended in 1 ml MB. We sheared the flagellar filaments by rapidly pushing the cell suspension through a 10 cm polyethylene tubing (0.58 mm inner diameter) ~ 50-75 times with the aid of two syringes with 21 gauge adapters. The sheared suspension was again washed in MB and resuspended in 400 μl MB. The concentrated cell suspension

was layered on top of a 12 mm diameter coverslip (Fisher Scientific). The cells were allowed to settle and tether to the coverslip surface for 5-7 min. The coverslip was then used to seal a perfusion chamber with the side with adhering cells facing inward [53]. The outlet of the perfusion chamber was connected with a 0.58mm ID mm tubing to a syringe pump (Chemyx Fusion 200) that withdrew fluid at ~120 μL/min. The inlet of the perfusion chamber was connected to a reservoir containing MB. Continuous perfusion with fresh MB eliminated oxygen gradients and removed cells that did not adhere to the surface.

3.4.4. Bead Assays

We treated the 12 mm coverslips with 0.01% poly-L-lysine. We then rinsed off unbound poly-L-lysine multiple times with MB. Next, we layered the sheared cells onto the coverslip. We waited ~ 5-7 min to allow the cells adequate time to settle and adhere to the surface. We then added ~ 10 μl of a washed 2μm bead suspension. We waited 5 min for the beads to sediment and tether to the flagellar stubs. Finally, the coverslip was used to seal the perfusion chamber, as discussed previously.

3.4.5. Phase and TIRF measurements

We coupled a 100 mW 514nm laser (Cobolt Fandango) into a TIRF microscope (Nikon Eclipse Ti-E) equipped with a 60x TIRF objective and aligned the laser to generate an evanescent field with a characteristic decay length of ~100 nm. Tethered cells were illuminated with the laser, and the emissions were filtered and relayed to a back-illuminated, cooled (-60°C), EMCCD camera (Andor iXon Ultra). A clean-up bandpass (555/55, Chroma Inc.) ensured that only the TIRF emissions entered the

EMCCD camera. This setup enabled us to visualize the cells in the phase contrast channel simultaneously. Phase illumination was achieved with halogen light filtered with a bandpass filter (745/90, Chroma Inc.). An IDS-uEye monochrome camera recorded the phase signal at 20-100 fps. A dichroic mirror (680 nm cut-off, Chroma Inc) split the TIRF emissions and the phase signals. Before obtaining the fluorescent emissions, we brought the tethered cells into focus in the phase channel. Our microscope is fitted with a Perfect Focus System (PFS, Nikon Inc), which helps maintain focus over long periods. We then exposed the cells to the laser while recording three consecutive images on the EMCCD camera, using an exposure time = 80 ms. A representative experiment is shown below, where we compared the numbers of FliM complexes in cells grown under different conditions.

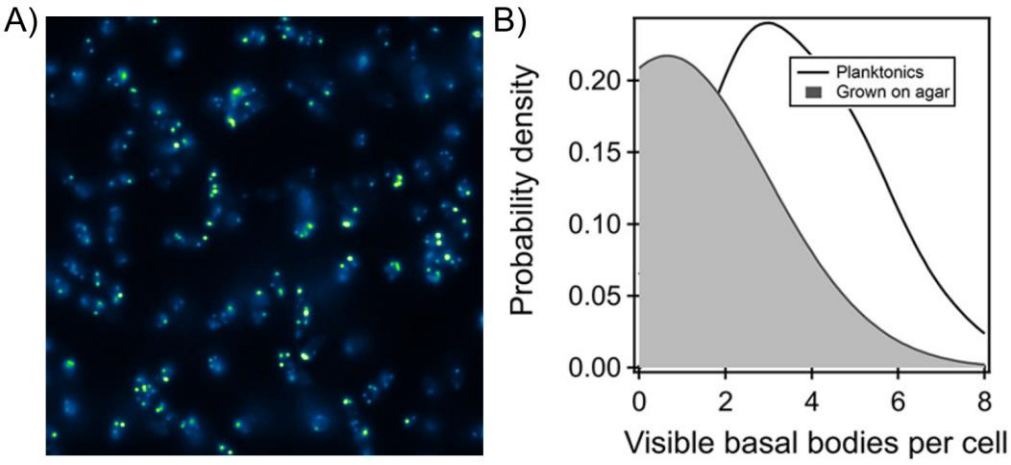

Figure 3-4. Visualization of putative flagellar motor preassemblies.
A) Motor pre-assemblies were determined by visualizing the fluorescent puncta formed by FliM-EYFP. **B)** The number of putative flagellar preassemblies were determined from TIRF measurements. There were fewer such bodies in the agar-grown cells (number of preassemblies = 0.64 ± 0.16, n = 28 cells) relative to the planktonic cells

(number of preassemblies = 3.72 ± 0.27, n = 29 cells), as seen from the kernel density estimates from the raw data. The difference in the means was significant ($p < 0.05$).

3.4.6. Optical Traps

We formed an optical trap with an IR laser (976 nm wavelength, ALS-IR-976-10-I-SF, Azurlight). First, we expanded the beam to ~10-12 mm diameter with a pair of lenses (Thorlabs Inc) that formed a Galilean telescope. The expanded beam was subsequently relayed with the help of another pair of lenses into the TIRF arm of a Nikon Ti-E microscope. A pair of dichroic mirrors reflected the beam to overfill the back-aperture of a 60X TIRF objective (Nikon Inc). See Appendix A Figure 2 for details.

3.4.7. Stalling of Tethered Cells

We treated 4.5 μm polystyrene beads (Polysciences, Inc.) with a 0.01% poly-L-lysine solution before introducing the beads into the perfusion chamber. The optical trap was used to trap a single bead at a time. Rather than moving the trap, we translated the microscope stage with a joystick (MS2000-XY, Applied Scientific Instrumentation Inc), which allowed us to precisely position the bead into the path of a rotating cell.

In an alternate version of this experiment, we used a micromanipulator (Eppendorf TransferMan® 4r) to push beads that were settled on the bottom coverslip of the chamber with microcapillaries (Piezo Drill Tip ICSI, 25° tip angle, 6 μm inner diameter, 6 mm flange).

3.4.8. Image Analysis

The rotation of tethered cells and beads was recorded with a phase contrast microscope at 20-100 fps with an IDS-uEye monochrome camera UI-3240LE-M-GL. We developed custom-written MATLAB codes to analyze the video recordings. To analyze bead rotation, we employed particle-tracking approaches that accurately detect the centroid of the bead in each image frame [35]. The bead positions followed circular tracks, which helped calculate the speed and the direction of rotation. The tethered cells were analyzed with custom-written cell-tracking algorithms, which fit ellipses to binarized images of the cell [35]. Each fit provided the orientation of the cell in that image. The speed and the direction of rotation were determined from the changes in the orientation with time. To calculate the point of tether, we plotted the center-of-mass of each fitted ellipse over the entire time-series data. As can be seen in Appendix A Figure 3, the center-of-mass followed a circular track. The center of the circular track was determined by fitting a circle, which coincided with the point of tether (and the location of the motor). The point of tether enabled us to determine the motor location in the corresponding TIRF channel.

In the case of tethered cells lacking stator proteins, we recorded movies for a long duration to allow the cells to rotationally diffuse along the point of tether. The point of tether could be readily determined if the rotation was ~ 180° or more. For cells that did not undergo at least a 180° turn, we used hydrodynamic flows to force rotation. Turning the flow in the perfusion chamber on and off was adequate to cause the cell to rotate and align with the flows. This method allowed us to determine the point of tether.

The TIRF images were analyzed following our previous algorithms [35]. First, we used a spatial bandpass filter to filter out background noise. The algorithm then detected an intensity peak that coincided with the motor, around which we placed a 350 nm digital mask. We then summed up the intensities of the pixels within the mask to quantitatively determine the intensity of the localized fluorescent puncta.

4. CHEMOTACTIC FUNCTIONS IN THE RUN-REVERSING BACTERIUM *HELICOBACTER PYLORI*[†]

4.1. Introduction

Over half of the human population is colonized by the motile gram-negative bacteria, *H. pylori*. *H. pylori* infections have been implicated in peptic ulcers as well as non-cardia gastric cancer [54]. Infections are promoted by the ability of the bacterium to swim with the aid of helical appendages called flagella [55, 56]. The flagellar filaments are rotated by transmembrane flagellar motors that repeatedly switch their direction of rotation. Owing to the unipolar location of the left-handed flagellar filaments [57], counterclockwise (CCW) rotation of the motors causes the cell to run with the flagella lagging behind the body – a mode of motility termed as the *pusher* mode. The cell reverses with the body lagging the flagella when the motors switch the direction of rotation to clockwise (CW). This mode of motility is termed as the *puller* mode [58]. Modulation of the reversals between the two modes enables the cell to undergo chemotaxis — migration towards favorable chemical habitats [59-61], which promotes pathogenesis. The core chemotaxis network is similar to that in *E. coli* [59, 62-65]. Several components that form the flagellar motor are also similar to those in *E. coli* [59]. How the chemotaxis network modulates flagellar functions in *H. pylori* remains unknown [59, 63, 66].

[†] Adapted with modifications from "Asymmetric random walks reveal that the chemotaxis network modulates flagellar rotational bias in *Helicobacter pylori*" by JD Antani, AX Sumali, TP Lele, and PP Lele, 2021, eLife **10**: e63936.

Switching in the direction of flagellar rotation is promoted by the binding of a phosphorylated response regulator, CheY-P, to the flagellar switch. In the canonical chemotaxis network, chemoreceptors sense extracellular ligands and modulate the activity of the chemotaxis kinase, which in turn modulates CheY-P levels. Increased CheY-P binding to the motor promotes CW rotation in an otherwise CCW rotating motor [67]. The output of the flagellar switch is quantified by the fraction of the time that the motor rotates CW, termed CW_{bias} [31, 33, 68]. A decrease (increase) in CheY-P levels causes corresponding decrease (increase) in CW_{bias} [4, 69]. Thus, dynamic variations in the CW_{bias} sensitively report changes in the kinase activity due to external stimuli as well as due to the internal noise in the network [4, 70]. In contrast, the frequency at which motors switch their direction does not accurately represent changes in the chemotaxis output as the frequency decreases when CheY-P levels increase as well as when CheY-P levels decrease [4]. Prior work has focused exclusively on the effects of extracellular ligands on the frequency of cell reversals [71-76] rather than the motor bias. It is unknown whether the chemotaxis network in *H. pylori* modulates the rotational bias.

In run-reversing bacteria, reversal frequencies can be readily quantified based on the number of reversals made by the swimming cell per unit time [71-76]. To quantify the CW_{bias} however, the duration for which the cell swims in each mode needs to be determined by distinguishing between the two modes. However, discriminating between the swimming modes of single *H. pylori* cells is difficult owing to the technical challenges in visualizing flagellar filaments in swimmers [57, 77]. A popular method to

quantify the CW_{bias} is by monitoring the rotation of tethered cells, where a single flagellar filament is attached to a glass surface while the cell freely rotates [31]. Alternatively, the bias is determined by sticking the cell to the surface and monitoring the rotation of a probe bead attached to a single flagellar filament [78, 79]. Such single motor assays have been employed successfully in *E. coli* because the filaments are spaced apart on the cell body. In *H. pylori* however, the flagella are distributed in close proximity to one another at a single pole [49], increasing the likelihood of tethering more than one filament. Tethering of multiple flagella on the same cell eliminates rotational degrees of freedom, inhibiting motor function. Because of the limited measurements of the CW_{bias}, crucial features of the signaling network, such as the dynamic range of signal detection, adaptation mechanisms, and the roles of key chemotaxis-related proteins, remain unknown in *H. pylori* [59, 60, 63, 66].

Here, we report a novel approach to measure the CW_{bias} based on differences in the swimming speeds in the pusher and puller modes of *H. pylori*. We successfully employed this method to determine the effect of a known chemoattractant and varying temperatures on the CW_{bias}. Our observations suggest that the CW_{bias} decreases upon stimulation with an attractant, similar to the canonical model. The default direction of flagellar rotation is CCW and the presence of CheY increases the $CW_{bias} \sim 0.35$. The relationship between reversal frequencies and rotational bias is unimodal. These results are consistent with the notion that the chemotaxis network modulates the flagellar rotational bias (as well as the reversal frequencies) under environmental stimulus. Our quantitative model and simulations suggest that the basal chemotaxis output in *H. pylori*

and other run-reversing bacteria may be tuned to enhance diffuse spread. The approach discussed in this work provides a solid framework to study chemotaxis signaling and the behavior of the flagellar switch in *H. pylori*.

4.2. Results

4.2.1. Swimming speeds are asymmetric

To determine the behavior of flagellar motors in *H. pylori*, we tracked cell motility in the bulk fluid with a phase contrast microscope. The positions of single cells were quantitatively determined from digital videos with the aid of particle tracking (see *Materials and Methods*, section 4.4). Owing to the use of low magnification microscopy, we were able to observe several cells exhibiting reversals in the field of view. A representative cell trajectory at 37°C is shown in Figure 4-1A (see another example in Movie S2). With each reversal, the cell appeared to change from one mode of swimming to the other, although the modes could not be identified (as puller or pusher) because the flagella were not visible. Changes in the swimming modes were distinguished from rotational turns of the cell body – where the swimming mode remains unchanged – by visually inspecting each reversal for each cell. The turn angle between the original direction just before and the new direction just after a reversal ($\emptyset$) followed an exponential distribution with a peak ~ 180° (Figure 4-1B), indicating that cells simply retraced their paths for brief durations following each reversal. The flick of the flagellum that causes turn angles to be distributed ~ 90° in another run-reversing species *Vibrio alginolyticus* [80], is unlikely to occur in *H. pylori*. The distance traveled between any two reversals was identified as a segment and numbered (Figure 4-1A). The swimming

speeds over 6 consecutive segments are indicated in Figure 4-1C. The speeds were binned as per the segments, yielding *n+1* bins for *n* reversals. The mean speed from each bin was plotted for all the *n+1* bins (Figure 4-1D). Mean speeds in alternate bins were anti-correlated: each reversal either decreased or increased the speed. This suggested that the speeds in the two modes were unequal. Such anti-correlation was consistently observed in a large population of cells (n = 250). The distribution of the ratio of their mean speeds in the fast and slow modes is shown in Figure 4-1E. The speed in the fast mode was ~ 1.5 times the speed in the slow mode.

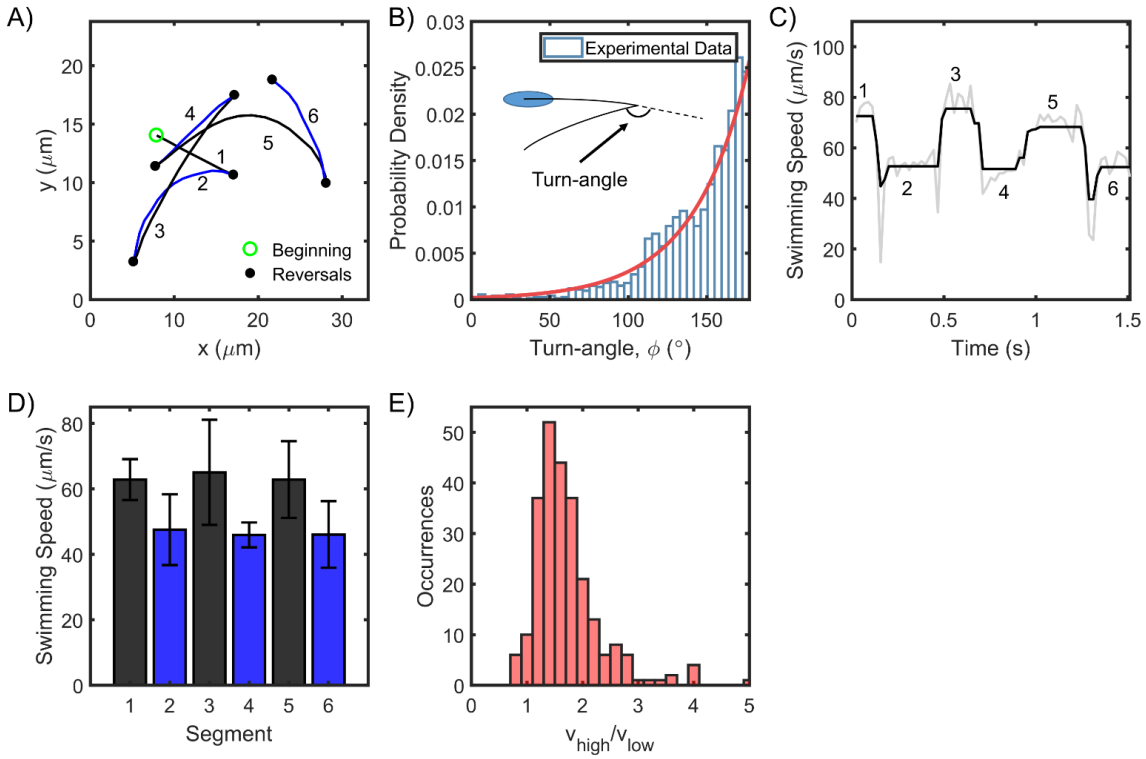

Figure 4-1 *H. pylori* swim forward and backward at different speeds.

A) Representative swimming trace of a single bacterium. Each reversal is represented by a filled circle. The beginning of the trajectory is denoted by an open circle. Uninterrupted swimming between two reversals was labeled as a segment and the

(Figure 4-1 Continued…)
segments were numbered chronologically. **B)** The turn angles were exponentially distributed (n = 1653 samples); reversals mostly caused the cells to retrace their movements. **C)** The swimming speed for a single cell over 1.5 s is indicated. The speeds alternated between high and low values with each reversal. Raw data is indicated in gray; filtered data is indicated in black. **D)** The mean speed for each segment is indicated chronologically. Standard deviations are indicated. **E)** The mean speed for the high (low) mode for each cell was calculated by averaging over all its high- (low-) speed segments. The distribution of the ratios of the high and low mean speeds for each cell is indicated. The mean ratio was 1.5 ± 0.4 (n = 250 cells). Reprinted with permission from [16].

4.2.2. Cell swims faster in the pusher mode

A recent study attempted to visualize the flagella in *H. pylori* with high magnification microscopy, and claimed that the cells swam faster in the pusher mode. However, the sample sizes were severely limited by the difficulties in visualizing flagella on the swimmers [57]. To conclusively determine the faster mode in *H. pylori*, we exploited the hydrodynamic coupling between swimmers and glass boundaries. Cells that swim very close to an underlying solid boundary exhibit circular trajectories owing to the increased viscous drag on the bottom of the cell and the flagellar filaments. CCW rotation of the left-handed helical filament causes the *pusher* to experience a lateral force that promotes CW circular tracks (Figure 4-2A, [81, 82]). The situation is reversed when the filaments rotate CW. Thus, it is possible to discriminate between the two modes when a bacterium swims near a surface. We analyzed each cell that swam in circular trajectories near the surface and determined the mean speeds for the two directions. The cells were viewed from the bulk fluid, as indicated in Figure 4-2A (*right panel*). Four

sample trajectories are shown in Figure 4-2B. For each cell, the CW trajectories were always faster relative to the CCW trajectories, indicating that the pusher mode was the faster mode (Figure 4-2C). This was confirmed over n = 116 cells; the mean ratio of the speeds of the CW trajectories to that of the respective CCW trajectories was ~ 1.6 ± 0.5 (Figure 4-2D).

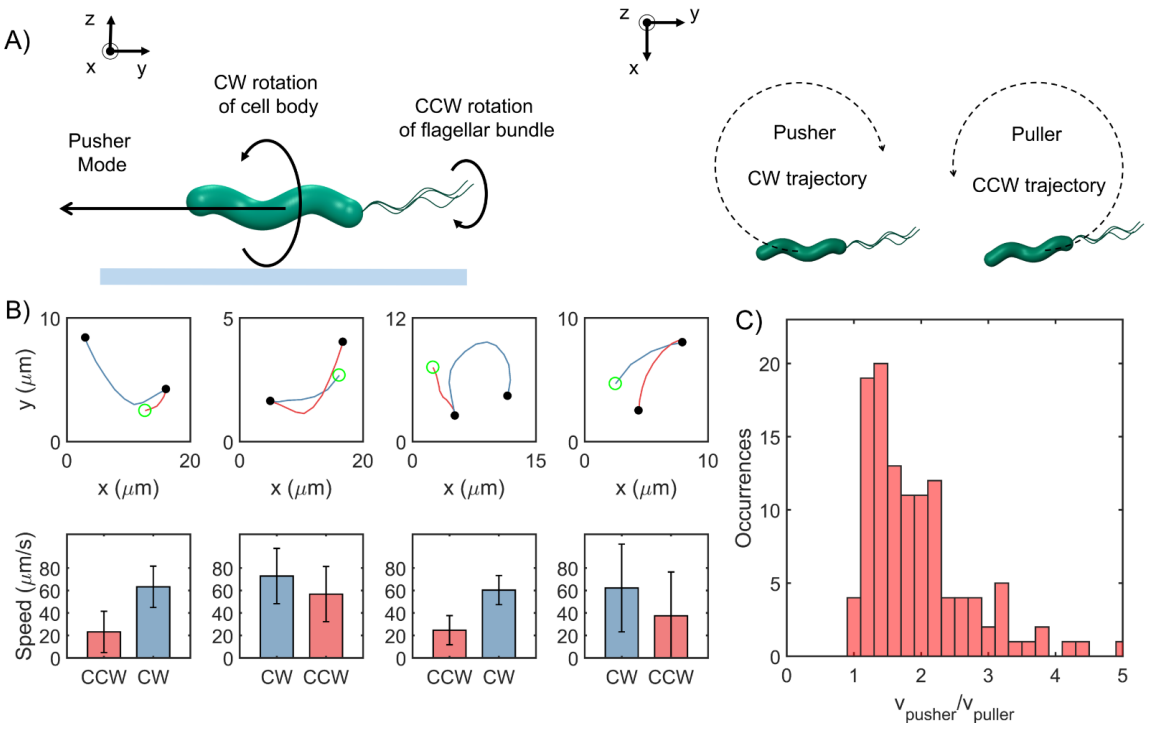

Figure 4-2 Cells swim faster in the pusher mode.

A) The viscous drag on the bottom of the cell body and the flagellar filament is higher near an underlying surface (indicated by the blue line in the *left panel*). The drag is lower on the top half of the body and filament. This difference in drag causes a lateral thrust on the cell, giving rise to circular trajectories: CW trajectory in the pusher mode and CCW trajectory in the puller mode (*right panel*). **B)** *Top row:* Blue segments indicate CW trajectories; red segments indicate CCW trajectories. Filled circles indicate reversals; open circle indicates the beginning of the trajectory. *Bottom row:* The corresponding mean speeds and standard deviations are indicated for the two trajectories: CW tracks

(Figure 4-2 Continued)
were always faster than CCW tracks. **C)** The distribution of the ratio of the speeds along the pusher and puller modes is indicated (n = 116 cells). The mean ratio = 1.6 ± 0.5. Reprinted with permission from [16].

4.2.3. Partitioning of swimming speeds enables estimation of chemotaxis response to attractants

As *H. pylori* rotate their flagella CW in the puller mode, the CW_{bias} could be calculated from the fraction of the time that the cells swam slower (see *Materials and Methods*, section 4.4). This method worked for all the cells that reversed at least once in the field of view: the faster and slower modes could be discriminated from each other based on comparisons between the mean speeds before and after a reversal (as shown in Figure 4-1D). These cells consisted ~81% of the total data. The remaining cells did not reverse under observation; they persisted in a particular direction before exiting the field of view. Hence, these cells were termed as single-mode swimmers. As the mode of swimming could not be readily determined for these cells, those data were grouped into cells that swam near the surface for at least some time and those that did not. In the former group of cells, the majority was identified as pushers based on the direction of their circular trajectories near surfaces, as discussed in Figure 4-2. About 8% of the cells could not be identified and were excluded from the analysis. The distribution of the bias is shown in Figure 4-3. The bias was similar to that observed in *E. coli* [31, 39, 46, 83-85], suggesting that the basal chemotactic output in the two species is similar. As evident, most cells tended to rotate their motors CCW for a higher fraction of time.

Next, we imaged swimmers belonging to a *cheY*-deleted strain and observed that the trajectories of cells near a surface were exclusively CW circles. More than 150 cells were observed near surfaces and they exhibited CW trajectories. A fraction of the data is shown in Figure 4-3B and in Appendix B Figure 1. This suggested that the default direction of flagellar rotation is CCW, similar to *E. coli* [39, 86]. Considering that the bias is zero in the absence and ~ 0.35 in the presence of CheY, CheY-P binding likely promotes CW rotation in an otherwise CCW rotating motor in *H. pylori*.

To test the idea that the chemotaxis network modulates the rotational bias, we employed our technique to quantify changes in the CW_{bias} in swimmers when stimulated by a chemical attractant. We stimulated cells by adding them to a bath of urea (20 mM in motility buffer-MB, see *Materials and Methods*—section 4.4), which is a potent chemoattractant for *H. pylori* [87]. Following exposure to the attractant, majority of the cells swam exclusively in the pusher mode – their post-stimulus CW_{bias} was ~ 0 (Figure 4-3C). The reversal frequency also decreased in response to the chemo-attractant (Figure 4-3D), which is in agreement with previous reports [72, 88]. In comparison, the post-stimulus CW_{bias} in swimmers exposed to MB-only (control case) did not change significantly and continued to exhibit both modes of motility (Figure 4-3C, D). These observations are consistent with the notion that a reduction in the kinase activity upon the sensing of chemo-attractants inhibits the rotational bias of flagellar motors, similar to how the chemotaxis network modulates the response of *E. coli* to attractants [31].

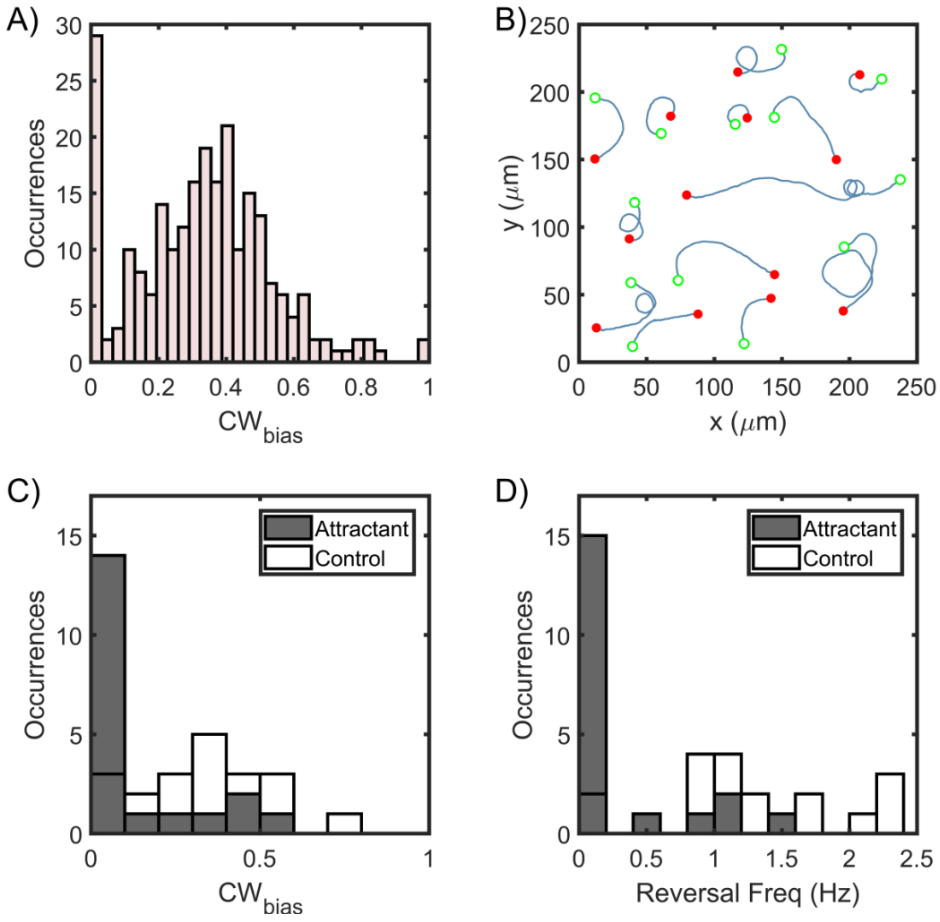

Figure 4-3. Asymmetric swimming speeds enable quantification of chemotaxis output. **A)** CW_{bias} was determined at 37°C in the absence of chemical stimulants. Cell trajectories with durations of 1 s or more were considered for calculation. The distribution was obtained from n = 240 cells. A Gaussian fit to the switching population (n = 212 cells) yielded CW_{bias} = 0.35 ± 0.23 (mean ± standard deviation). **B)** Single cell trajectories of a Δ*cheY* mutant are indicated. Cells swam in CW-only trajectories, which indicate CCW flagellar rotation. Open green circles denote the start of a trajectory; filled red circles denote the end. The trajectories were spatially displaced to group them for the purpose of illustration and truncated to show the direction of rotation. Full trajectories and additional cells are included in Appendix B Figure 1. **C)** The post-stimulus CW_{bias} was monitored for ~ 30-60 s immediately following exposure to 20mM urea (n = 20 cells); 14 cells swam exclusively in the pusher mode during the period of observation

(Figure 4-3 Continued…)
and displayed CW-only trajectories near surfaces. In the control case, cells were exposed to the buffer-only. The average post-stimulus CW_{bias} was 0.31 ± 0.04 (mean ± standard error, n = 20 cells). The difference in the mean bias for the attractant and the control cases was significant (p-value < 0.001). **D)** The post-stimulus reversal frequency for cells treated with urea was 0.23 ± 0.09; those treated with the buffer had an average reversal frequency of 1.4 ± 0.04. The difference in the mean frequency for the attractant and the control cases was significant (p-value < 0.001). Reprinted with permission from [16].

4.2.4. Effect of thermal stimuli on chemotactic output

Majority of the previous experiments on motility and chemotaxis in *H. pylori* have been performed at room temperatures [57, 60, 89]. However, in the host, *H. pylori* experience higher temperatures. Here, we explored how changes in the surrounding temperatures modulated flagellar output in *H. pylori*. We recorded cell motility at different temperatures. The recording began ~ 5-10 min after each temperature change to provide adequate time for transient processes to stabilize (see *Materials and Methods*, section 4.4, for additional information). The mean pusher and puller speeds trended upwards with the temperature (Figure 4-4A, *left panel*), presumably through modulation of proton translocation kinetics that power the motor [90]. The ratio of the speeds in the two modes appeared to be independent of the temperature (Figure 4-4A, *right panel*). These responses are consistent with experiments in *E. coli* that show a strong influence of temperatures on the rotational speeds of the flagellar motor [90-92].

The frequency of reversals increased steadily with temperature up to 37°C, whereas the steady-state CW_{bias} varied weakly with temperature (Figure 4-4B). At room

temperatures, the CW_{bias} was the lowest, indicating that the cells mostly prefer to swim in the pusher mode. Next, we combined our data over the entire range of temperatures (25° to 43°C) and for each cell, plotted the reversal frequency against its CW_{bias}. The reversal frequency was maximum at ~ 0.5 CW_{bias} and decreased on either side (Figure 4-4C); also see Appendix B Figure 3. As our results suggest that CheY-P binding likely increases the CW_{bias} (Figure 4-3B, C), this also means that the reversal frequency has a similar unimodal dependence on CheY-P levels. Hence, we propose that changes in the reversal frequency in *H. pylori* cannot provide accurate information about the effect of stimulants on the kinase activity (i.e., whether a stimulant increases or decreases the activity). On the other hand, the rotational bias is likely a better measure of the kinase activity, similar to that in *E. coli*.

In *E. coli*, flagellar switching has been well described by a two-state model, where the binding of phosphorylated CheY (CheY-P) to the flagellar switch stabilizes the CW conformation [92]. In the absence of CheY-P, the probability of observing CW rotation in an otherwise CCW-rotating motor decreases with increasing temperatures [91]. The chemotaxis network itself adapts such that the steady-state levels of CheY-P are independent of the temperatures [8]. Assuming that CheY-P levels are also independent of the temperature in *H. pylori*, the relative insensitivity of the rotational bias in Figure 4-4B suggested that the dissociation constant for CheY-P/switch interactions likely decreased with rising temperatures. Following the thermodynamic analysis of Turner and co-workers for a two-state flagellar switch [92], we calculated the dissociation constant normalized by CheY-P levels, as shown in Figure 4-4D (see

Appendix B.2 for details). Assuming that the CheY-P levels are ~ 3 μM [4], we estimate the dissociation constant to be ~ 9 μM at 37°C.

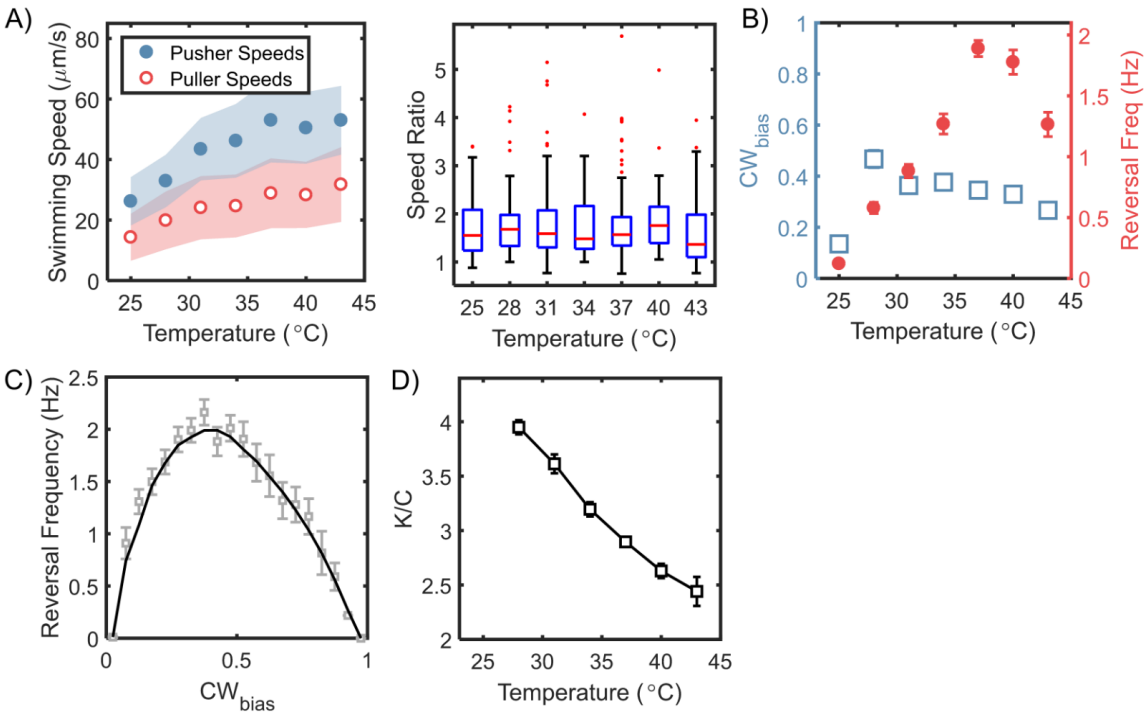

Figure 4-4. Steady-state chemotactic output is independent of temperature.

A) ***Left*****:** Swimming speeds for each mode are plotted (mean ± standard deviation) for different temperatures. The speeds increased with temperature till 37°C, after which they plateaued. The shaded regions indicate standard deviation. ***Right*****:** The ratios of the pusher and puller speeds are independent of the temperatures, as indicated. A red horizontal line indicates the median ratio at each temperature, and the bottom and top borders of the encompassing box indicate the 25th and 75th percentiles. The extended lines span 99.3% of the data and the dots indicate outliers. **B)** Mean CW_{bias} (open squares) and mean reversal frequencies (filled circles) are plotted over a range of temperatures. The switching frequency was at a maximum at the physiological temperature (37°C), and decreased at higher and lower temperatures. The CW_{bias} increased with the temperature and plateaued above 30°C. The mean values are indicated with standard error. Each data-point was averaged over n ≥ 80 cells. **C)** The relationship

(Figure 4-4 Continued…)
between reversal frequency and CW_{bias} is indicated. The values were obtained from the combined datasets over the entire range of temperatures that we studied (n = 972 cells). The CW_{bias} was binned (bin size = 0.05), and the mean reversal frequency for each bin was estimated. The mean and standard errors are indicated in grey. The black curve is a guide to the eye. **D)** The estimated ratio of the CheY-P dissociation constant (K) and the intracellular CheY-P concentrations (C) is indicated as a function of the temperature. The ratios were calculated from the data in **B)** following a previous approach [92]. The number of binding sites for CheY-P in *H. pylori* ~ 43 was estimated from the relative sizes of the flagellar C-ring (see Appendix B.2 and ref. [49]). The ratio of the dissociation constants for the CCW and the CW motor conformations was assumed to be similar to that in *E. coli* (~ 4.7 from [93]). Reprinted with permission from [16].

4.2.5. Speed asymmetry promotes diffusion

Even without chemotaxis, motility enhances the spread of bacteria, lending a significant advantage over immotile bacteria in exploring three-dimensional spaces [94]. Bacterial motion becomes uncorrelated over long times and large length-scales in the absence of a signal. Several previous works have modeled the diffusion of motile bacteria by assuming that the reversal wait-times are exponentially distributed [3, 95-97]. The wait-time refers to the time between two consecutive reversals. In some bacterial species that exhibit runs and reversals, the wait-time is Gamma distributed [97-99]. The assumption of exponentially distributed wait-times leads to inaccurate predictions in such species [97].

Our cell-tracking analysis revealed that the reversal wait-times were Gamma distributed in *H. pylori* (Figure 4-5A, also see separate distributions for the two swimming modes in Appendix B Figure 4). When calculating the wait-times, we

excluded the beginning of each cell-trajectory just before the first reversal and the end of each cell-trajectory just after the final reversal. To derive an explicit expression for the diffusivity of asymmetric run-reversers that exhibit Gamma distributed reversal intervals, we preferred to modify a previous approach developed for symmetric run-reversers [100] rather than a more general model [101] – see Appendix B.4 for details. Briefly, the velocities of a bacterium that swims at v_0 μm/s in its slower mode was expressed as: $\boldsymbol{v}(t) = v_0\, h(t)\, [1 + aH(h)]\boldsymbol{e}(t)$. The direction of swimming was described by the function $h(t)$, which alternated between $+1$ and -1 with each reversal (Figure 4-5B). A Heaviside function, $H(h)$ and the asymmetry parameter, a, characterized the magnitudes of the speeds in the two directions: v_0 and $v_0(1 + a)$. The CW_{bias} was assumed to be constant (= 0.5) for simplicity.

The deviation of the cell from a straight line during a run (or reversal) occurred due to rotational diffusion, described by $\frac{d\theta}{dt} = \sqrt{2D_\theta}\xi(t)$. White noise characteristics were $\langle \xi(t) \rangle = 0$, and $\langle \xi(t)\xi(t + \tau) \rangle = \delta(\tau)$, where D_θ is the rotational diffusion coefficient. Another randomizer of the bacterial walk is the turn angle, $\emptyset$, which is the angle between the original direction just before and the new direction just after a reversal. The turn angle is likely influenced by kinematic properties: cell shape, filament bundling dynamics, and the flexibility of the flagellar hook. After taking into account the specific form of the reversal wait-time distribution for *H. pylori* (Figure 4-5A), we obtained the following expression for the asymptotic diffusion coefficient from the velocity correlation over long-times:

$$D = \frac{v_0^2}{2D_\theta}\left[\frac{(1+a)^2+1}{2}\cdot\left\{\begin{array}{c} 1-\frac{\omega}{D_\theta}\left(1-\frac{(3\omega)^3}{(3\omega+D_\theta)^3}\right) \\ +\frac{|\langle cos\emptyset\rangle|^2\omega}{D_\theta}\cdot\frac{(3\omega)^3}{(3\omega+D_\theta)^3}\cdot\frac{\left((3\omega+D_\theta)^3-(3\omega)^3\right)^2}{(3\omega+D_\theta)^6-|\langle cos\emptyset\rangle|^2(3\omega)^6} \end{array}\right\}\right.$$
$$\left.-(1+a)\left\{\frac{|\langle cos\emptyset\rangle|\cdot\omega}{D_\theta}\cdot\frac{\left((3\omega+D_\theta)^3-(3\omega)^3\right)^2}{(3\omega+D_\theta)^6-|\langle cos\emptyset\rangle|^2(3\omega)^6}\right\}\right] \quad (1)$$

The reversal frequency is indicated by ω. The expression correctly reduces to that for the symmetric swimmer [100], for α ($= |\langle cos\emptyset\rangle|$) = 1, and a = 0.

As shown in Figure 4-5C, the diffusion coefficients increased with the asymmetry-parameter, a. As per the predictions, asymmetric run-reversers ($a \neq 0$) spread faster than symmetric run-reversers (a = 0). Next, we carried out stochastic simulations of 1000 cells that underwent asymmetric run-reversals with Gamma distributed intervals (see Appendix B.5). The diffusion coefficients from the simulations matched predictions from our model that incorporated Gamma distributed wait-times. Having validated our simulations, we estimated the diffusion coefficients for arbitrary CW_{bias} values over varying a. As shown in Figure 4-5D, the simulated diffuse spread was low when cells covered similar distances in the forward and backward directions, thereby minimizing net displacement. This tended to occur for swimmers with low a values that swam for equal durations in the two directions (CW_{bias} ~ 0.5). For any given a, the diffuse spread increased with the net displacement during a run-reversal, for example, when the swimmer preferred the slower mode much more than the faster mode. The net displacement, and hence, the spread tended to be the highest when the cells spent a greater fraction of the time swimming in the faster mode compared to the slower mode. Thus, in *H. pylori*, the tendency to spend more time in the faster pusher mode (basal

CW_{bias} ~ 0.35, Figure 4-3A) is advantageous (Figure 4-5D). This advantage is amplified by increasing pusher speeds relative to the puller speeds. However, a very low basal value of the CW_{bias} is disadvantageous from a chemotaxis perspective. *H. pylori* appear to respond to attractants by reducing their CW_{bias} (Figure 4-3C). They would lose their ability to respond to attractants if the pre-stimulus (basal) bias was close to its minimum value (= 0). It is possible therefore, that the basal activity of the chemotaxis network is optimized in asymmetrically run-reversing bacteria to promote higher diffusive spread while retaining the ability to respond to chemical stimuli.

Finally, longer durations of runs and reversals helped cells cover larger distances. Thus, the diffusion coefficient was inversely dependent on the run-reversal frequency (Figure 4-5E). As the reversal frequencies reach a maximum at 37°C (Figure 4-4B), it is possible that cells at physiological temperatures spread slower in a niche over long times, providing more time for cells to adhere to surfaces.

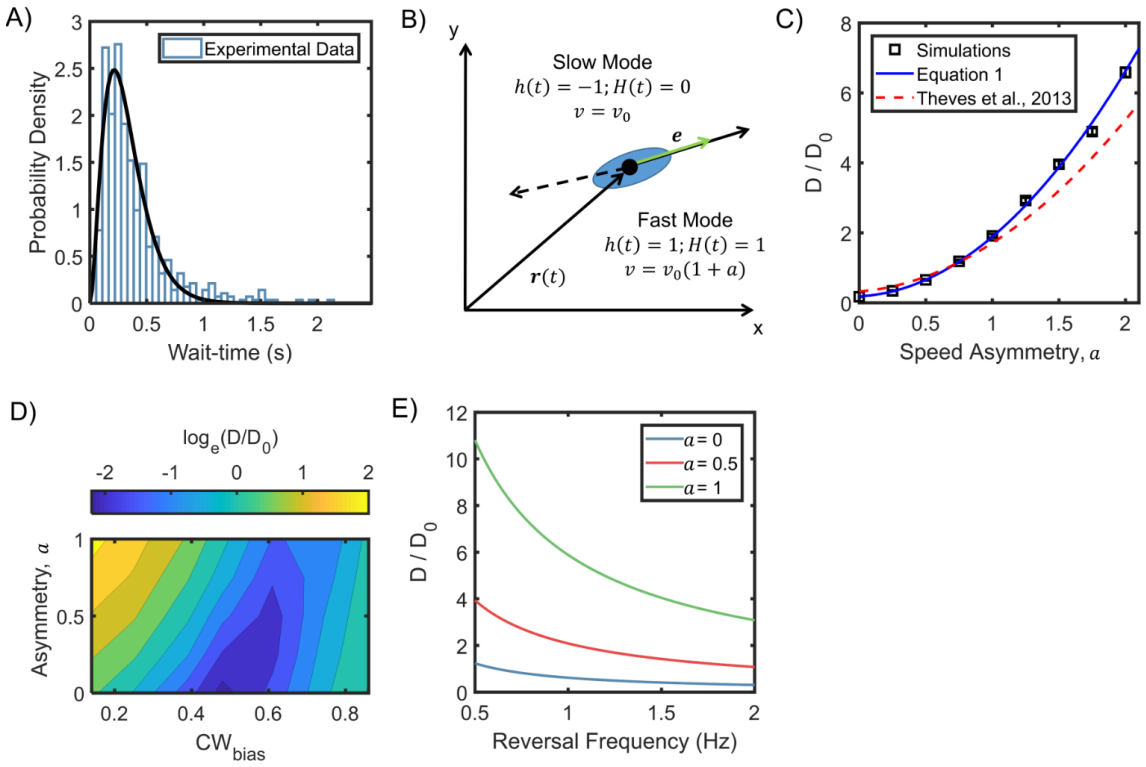

Figure 4-5. Asymmetric random walks in a run-reversing bacterium.

A) Experimentally observed wait-time intervals for runs and reversals obey a Gamma distribution (n = 515 samples): the shape and scale parameters were k = 2.92 ± 0.06 and θ = 0.11 ± 0.00, respectively. **B)** Cell swims at v_0 μm/s in the puller (slower) mode, and at $v_0(1 + a)$ μm/s in the pusher (faster) mode. The symmetric case is described by a = 0, where the run and reverse speeds are equal. Cell alignment is described by the unit vector $\boldsymbol{e}$. **C)** The diffusion coefficients predicted from equation 1 are indicated as a function of the asymmetry in speeds (blue curve). An alternate model that assumes exponentially distributed wait-time intervals in asymmetric swimmers under predicted the diffusivity, as shown by the dotted curve [97]. Symbols indicate coefficients calculated from simulation runs (see Appendix B.5). The parameters were based on experimental measurements: mean wait-time = 0.3 s, α = 0.86, and v_0 = 25 μm/s. D_θ = 0.02 s^{-1} from [100]. Diffusion coefficients have been non-dimensionalized with $D_0 = v_0^2/3\omega_p$ [95], where ω_p is the mean reversal frequency at the physiological temperature (Figure 4-4B). **D)** Diffusion coefficients were calculated from simulations of cell

(Figure 4-5 Continued…)
motility in the absence of a stimulus over a range of a and CW_{bias} values (see Appendix B.5 for details). The diffusion coefficients were normalized with D_0. The sum of the mean wait-times (CW and CCW) was fixed at 0.35 s. **E)** Predicted diffusivity is indicated over a range of typical reversal frequencies. Here, $\alpha = 0.86$ and $D_\theta = 0.02\ s^{-1}$**.** Reprinted with permission from [16].

4.3. Discussion

H. pylori experience physiological temperatures (~ 37 °C) in their human hosts. Previous studies on motility in *H. pylori* have largely been performed at room temperatures [57, 60, 89]. Here, we characterized flagellar functions at physiologically relevant temperatures. Our experiments with a mutant lacking *cheY* showed that the flagellar motors in *H. pylori* rotate CCW by default (Figure 4-3B). At native CheY-P levels, motors in wild-type cells spent about 35% of the time rotating CW (Figure 4-3A) – thus, the probability of CW rotation increases with CheY. Our experiments further showed that treatment of wild-type cells with a potent attractant (urea) decreased the rotational bias (CW_{bias}). These results are consistent with a model in which the chemotaxis network controls the levels of CheY-P to modulate the probability of CW rotation in an otherwise CCW rotating flagellar motor. If so, then the chemotaxis networks in the two species, *E. coli* and *H. pylori*, modulate flagellar functions in a similar manner.

Earlier works focused exclusively on the effect of chemoeffectors on steady-state reversal frequencies in *H. pylori* to characterize chemotaxis responses [71-76]. Because diffusion scales inversely with the reversal frequency (Figure 4-5E), increases in

frequency might help a cell linger in a niche. However, mere variations of the steady-state reversal frequencies with the local stimulant concentrations (or temperatures) does not enable chemotaxis [3]. By combining data collected over a range of temperatures, we showed that the dependence of the reversal frequency on the rotational bias is unimodal (Figure 4-4C). This means that the reversal frequency does not have a unique value with respect to the rotational bias (other than at maximal frequency), similar to that in *E. coli* (Figure 4-6A). Hence, the reversal frequency value is also unlikely to be unique with respect to the kinase activity (the corresponding relationship in *E. coli* is depicted in Figure 4-6B). Therefore, changes in the reversal frequencies by themselves are unlikely to accurately report changes in the chemotaxis output in *H. pylori*. Our results suggest that the rotational bias must be quantified to accurately determine the chemotaxis output in *H. pylori*.

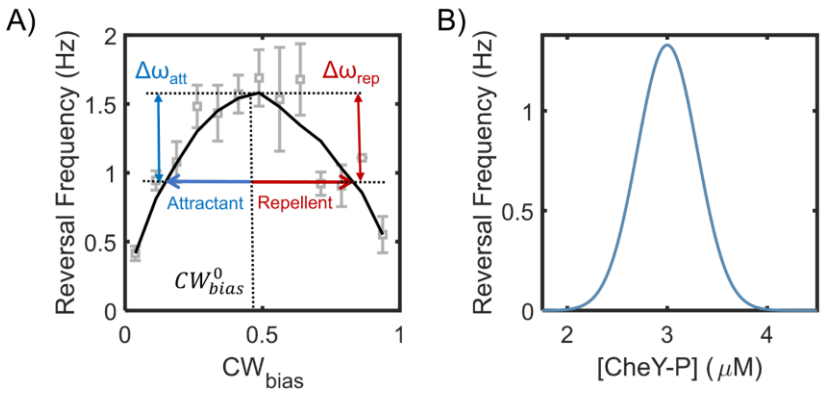

Figure 4-6. Motor reversal (switching) frequencies versus CW_{bias} and CheY-P
A) The dependence of motor reversal frequencies in *E. coli* on the CW_{bias} is unimodal [102], similar to *H. pylori* (Figure 4-4B). The symbols indicate experimental data from ref. [102]. The black curve is a guide to eye. The blue and red arrows indicate the effect of attractants and repellents on the CW_{bias}, respectively. The corresponding changes in

(Figure 4-6 Continued…)
the reversal frequency are similar ($\Delta\omega_{att} \sim \Delta\omega_{rep}$). **B)** The dependence of switching frequency on CheY-P levels is also unimodal in *E. coli* [4]. Thus, an attractant as well as a repellent can induce a drop in the frequency. Reprinted with permission from [16].

Our model for diffusive spread of motile bacteria indicated that run-reversing bacteria that undergo asymmetric random walks diffuse faster than symmetric run-reversers (Figure 4-5C). This is expected, as symmetric run-reversals tend to minimize net displacements. Simulations of bacterial diffusion in the absence of stimulants indicated that the diffusive spread is higher in asymmetric run-reversers when the cells spend a greater fraction of the time swimming in the faster mode compared to the slower mode. Thus, the preference for the faster pusher mode (lower CW_{bias}) in *H. pylori* is advantageous as it helps them spread faster (Figure 4-5D). However, *H. pylori* appear to respond to attractants by reducing their CW_{bias} (Figure 4-3C). A very low value of the basal bias would inhibit the ability to respond to attractants entirely. Hence, we propose that the basal activity of the chemotaxis network is probably tuned to promote higher diffusive spread while optimizing chemotaxis performance. In general, asymmetry in swimming – differences in swimming speeds or differences in the amount of time spent in any one mode or both – may provide evolutionary benefits to run-reversing bacteria by enhancing their spread.

The response of the chemotaxis network to external stimuli is conventionally measured by determining the rotational bias [31, 44, 68, 103]. Tethering cells to glass surfaces is the preferred method of determining the rotational bias. This approach is only useful when one can ascertain that the filament has adhered to the surface, for example

with the use of antiflagellin antibodies that irreversibly link the filament to the surface. However, some studies may forego the use of antibodies when determining the bias. This is problematic as the cell can appear to be tethered but instead it pivots about its non-flagellated pole on a surface while the free rotation of the invisible filament causes the cell to rotate. This can lead to the mischaracterization of the direction of flagellar rotation, and therefore the rotational bias [7, 104, 105]. Alternately, the signaling output has been determined via Förster resonance energy transfer-based measurements of *in vivo* enzymatic reactions [106]. But, neither of these approaches has been realized in *H. pylori*. Here, we characterized the rotational bias based on the asymmetry in the swimming speeds. Our use of low magnification microscopy allowed us to collect large sample sizes to characterize flagellar functions, considerably improving on earlier efforts [57].

To prevent the cell from tumbling during a reversal, all the flagellar motors in a single cell of *H. pylori* must switch synchronously from one direction to the other. Indeed, tumbles were rarely observed. The most frequent turn angles were ~ 180°, which confirmed that the cells retraced their paths following a reversal – this would not have been the case if only a fraction of the motors switched to the opposite direction. This makes our approach feasible for determining the CW_{bias} for an individual cell from its swimming speeds – which reflects the collective action of all the motors – rather than sampling individual motors. How are such multiple stochastic switchers coupled in *H. pylori*? One possibility is that the flagellar switch in *H. pylori* is ultrasensitive to small fluctuations in CheY-P levels, similar to the switch in *E. coli* [4]. The close proximity of

the multiple motors at a single pole in *H. pylori* also means that the local concentration of CheY-P in the vicinity of each flagellar switch is similar. This increases the probability of concerted switching in all the motors.

In *V. alginolyticus*, asymmetry in swimming speeds has been observed only near bounding surfaces but not in the bulk fluid [107]. A limitation of our method is that it is unsuitable for tracking chemotaxis response dynamics in such species, as the asymmetry is lost whenever the cells migrate away from surfaces. In *H. pylori*, though, we observed asymmetric speeds in some cells even at a separation of ~ 200 μm from any bounding surfaces (see Appendix B.6), similar to *Pseudomonas putida* [97]. Therefore, the asymmetry is unlikely to be a surface-effect in *H. pylori*. The effect could be due to differences in the flagellar shape and forms [108] or the swimming gait in the pusher and puller modes [105, 109]. It is more likely that the asymmetry in speeds arises due to the differences in the CW and CCW flagellar rotational speeds, as is the case with *E. coli* – which run and tumble – and *Caulobacter cresecentus* [79, 105] – which exhibit symmetric swimming speeds in the pusher and puller modes (Table 4-1). Such differences in the speeds at which motors rotate CW and CCW depend on the external viscous loads [79, 105]. It is possible therefore, that the asymmetry in *H. pylori* is also load-dependent; vanishing for longer filament lengths in highly viscous microenvironments or for very short filaments. The asymmetry is further expected to depend sensitively on the expression of the flagellar genes, which is modulated by environmental conditions [110]. The asymmetry was prominently observable in our

work with a careful control of experimental conditions (*Materials and Methods*, section 4.4).

Table 4-1**.** Speed asymmetry across different bacterial species.
Reprinted with permission from [16].

Species	**Swimming Speed Ratio**	**Motor Speed Ratio**	**Reference**
H. pylori	1.5	-	This work
P. putida	2	-	[97]
V. alginolyticus	1.5	-	[107]
Burkholderia spp.	3.9	-	[108]
Vibrio fischeri	3.4	-	[108]
C. crescentus	1	~ 2	[105, 109]
E. coli	~ 1.3	1.3	[79, 111]

The flagellar motors in *H. pylori* and *E. coli* share structural similarities and have several orthologous components. The core chemotaxis network in the two species is also similar with the exception of a few enzymes [59, 60, 63, 66]. CheY, in its phosphorylated form, modulates flagellar functions in both species by interacting with components of the flagellar switch [49, 59, 77, 112]. Our results suggest that the regulatory function of CheY-P is also similar in the two species, i.e., CheY-P binding to the motor increases the probability of CW rotation. If so, then the implications of this finding are significant. Because *H. pylori* can retrace their paths upon a reversal unlike *E. coli*, modulation of the rotational bias is bound to undermine chemotaxis when the

cell enters the puller mode. Then, the cell would likely need a mechanism to rectify its movements with respect to the source or some type of feedback between the motors and the receptors to successfully migrate in response to chemical gradients. We anticipate that the approaches described in this work will help uncover these mechanisms and identify unknown protein functions. In Appendix B.8, we have discussed some of the open questions in the *H. pylori* chemotactic fields and our preliminary results from dynamic measurements of the chemotactic activity in response to various stimuli. Our approach is extensible to any run-reversing species that exhibit asymmetric swimming speeds, paving the way to study signaling dynamics in other run-reversing bacterial species.

4.4. Materials and Methods

4.4.1. Key Resources

Table 4-2. Key Resources Table

Reprinted with permission from [16].

Reagent type (species) or resource	Designation	Source or reference	Identifiers
cell line (*H. pylori*)	PMSS1	Karen Ottemann Lab, [113]	
chemical compound, drug	Brucella Broth	Millipore Sigma	B3051
chemical compound, drug	Columbia agar	Thermo Scientific™ Oxoid™	CM0331
chemical compound, drug	Defibrinated Horse Blood	Hemostat Laboratories	DHB100
chemical compound, drug	Fetal Bovine Serum	Gibco™	10438
chemical compound, drug	Polymixin-B sulfate	Alfa Aesar	J6307403
chemical compound, drug	Vancomycin hydrochloride	Sigma Aldrich	V1130
chemical compound, drug	β-Cyclodextrin	Sigma Aldrich	C4767
chemical compound, drug	Urea	Fisher Scientific	BP169
software, algorithm	MATLAB		

4.4.2. Strains and cell culturing

All the work was done with *H. pylori* PMSS1. Cultures of microaerophilic *H. pylori* were grown in an incubator with controlled temperature and CO_2–environment (Benchmark Incu-Shaker Mini CO_2). The incubator was maintained at 10% CO_2, 37°C. Fresh colonies were streaked out before each experiment on Columbia agar plates supplemented with 2.5 units/mL Polymixin-B, 10 μg/mL Vancomycin, 2 mg/mL β-cyclodextrin, and 5% v/v defibrinated horse blood. Colonies appeared on the horse-blood agar plates within 3-4 days and were picked with the aid of sterilized cotton-tipped applicators. The cells were then inoculated in 5 mL of BB10 (90% Brucella Broth + 10% Fetal Bovine Serum) to grow overnight cultures. No antibiotics were added to the liquid cultures as per previous protocols [72, 114]. Overnight cultures were grown for ~16 hours to an OD_{600}~0.25-0.5 and diluted to OD_{600}~0.1 in fresh BB10. The day cultures were grown to an OD_{600}~0.125-0.15 in the shaker incubator set at 170 rpm under 10% CO_2 and at 37°C. Prior to imaging, the cells were diluted in a motility buffer (MB- 0.01 M phosphate buffer, 0.067 M NaCl, and 0.1 mM EDTA, pH~7.0) at ~6-7% v/v (BB10/MB).

4.4.3. Motility assays

Cells were imaged in a culture-dish (Delta T^{TM} system, Bioptechs Inc.) on a phase-contrast microscope (Nikon Optiphot) equipped with a 10X phase objective. The dish was kept covered with a lid that was not airtight and that allowed a part of the top liquid surface to be exposed to air. Videos were recorded with a CCD camera (IDS model UI-3240LE) at 45 frames per second. Unless otherwise specified, the objective

was focused ~5-20μm away from the bottom surface of the culture-dish. All experiments were performed at 37° C unless otherwise noted.

4.4.4. Temperature control

The microscope was housed inside a temperature control chamber (ETS Model 5472, Electro-Tech Systems, Inc), which enabled precise control over the temperature during the experiments. The grown cultures were stored in flasks within the chamber. Prior to each measurement, ~ 50 μL of cells were diluted in ~ 1.3 – 1.5 mL of MB. The entire mixture was then transferred to the culture dish and covered with the lid. As the cell density was low (~ 4×10^6 cells/mL) and as the liquid surface was exposed to air, oxygen gradients were minimized; the cells remained motile in MB for over an hour.

In the case of the temperature variation experiments, the cells were visualized in the dish ~ 5 -10 min after each change in the temperature. Once recording was completed, the contents of the culture dish were emptied. The dish was then flushed with ethanol followed by copious amounts of DI water outside the chamber. The dish was then reused for further experiments. The whole cycle was repeated each time the temperature was changed.

4.4.5. Chemoattractant response

We filled the culture dish with 20 mM urea (Fisher Chemical™) in MB at 37° C, which served as an attractant. In the control case, no urea was added to the MB in the dish. We pipetted 50 μL of the cell culture into the dish prior to imaging. Videos were recorded and analysis was performed on the videos once the hydrodynamic flows visually subsided (~ 30s).

4.4.6. Data analysis

The low cell density enabled us to employ particle-tracking methods to record the swimming trajectory of each cell [78]. All the videos were analyzed with custom-written MATLAB codes based on centroid-detection-based particle-tracking routines [115]. The experimental data shown in Figure 4-3C, D and Figure 4-4 were obtained from two biological and multiple technical replicates. All other data were collected from 5 or more biological and multiple technical replicates.

4.4.7. CW_{bias} calculations

Recorded videos were visually scanned with ImageJ (NIH) to confirm the number of reversals for each cell. The distance traveled between any two reversals was identified as a segment and numbered (see Figure 4-1A**)**. The speeds were binned as per the segments, yielding *n+1* bins for *n* reversals. A reversal changes the mode of motility between the pusher and the puller mode. On the other hand, a 180° turn by the cell maintains the same mode. Each reversal was therefore confirmed visually to distinguish between reversals; 180° turns were rarely observed. In cells that swam near surfaces, the pusher and puller modes were readily determined as described in Figure 4-2. In cells that did not swim near surfaces, we compared the mean speeds, which alternated as shown in Figure 4-1D. All the *alternating* fast speed-bins were labeled as pushers; *alternating* low speed-bins were labeled as pullers. The video frames corresponding to the puller bins were labeled as puller frames.

To determine the CW_{bias}, cells that were observed for at least 0.5 s were retained for analysis. CW_{bias} was calculated as the fraction of the time that a cell swam in the

puller (slower) mode, which corresponds to CW rotation of the filament. To do this, the number of frames in which the ith cell swam in the puller mode (i.e., puller frames), N_i^{CW}, was divided by the total frames over which the cell was observed, N_i, to yield: $CW_{bias,i} = \frac{N_i^{CW}}{N_i}$

The error associated with the calculation of $CW_{bias,i}$ values decreases with increasing N_i. But, different cells were observed for different durations; hence the $CW_{bias,i}$ values were allocated weights that corresponded to their respective durations: $\dot{W}_i = \frac{N_i}{\sum N_i}$. Mean bias was determined as:

$$CW_{bias} = \sum \dot{W}_i CW_{bias,i}$$

Reversal frequency was determined in a similar manner.

5. CONCLUSIONS & FUTURE WORK

Our results in Chapter 3 suggest that in *E. coli*, the motor sensitivity to the chemotactic response regulator (CheY-P) is modulated by mechanical forces on the motor. The modulation can be thought of as long-range, because the stator MotA interacts with FliG, and not FliM, which contains the binding site for CheY-P. As the regulation is dynamic, it provides a mechanism for the motor to adapt chemotaxis response to changing viscous environments. Future work can determine how the mechanosensitive regulation of CheY-P binding modulates chemotaxis in high and low viscosity environments. A rudimentary model is described for this force regulation (Appendix A.7, Appendix A Figure 4), which can be built upon in the future to quantitatively explain the data.

In Chapter 4, we discussed our method to quantify the chemotactic output in *H. pylori*. The application of our approach is expected to help identify key chemotaxis enzymes, protein functions, and effectors in this biomedically-relevant pathogen. In Appendix B.7, additional preliminary experiments are described.

In *E. coli*, the flagella are uniformly distributed on the cell surface, which causes the cell to tumble when the flagella rotate in opposite directions. *Helicobacter pylori* run and reverse as they carry all their flagella at a single pole. When a cell of *H. pylori* rotates its motors CCW, it swims forward. If it swims towards an attractant source, the decreasing kinase activity will decrease the probability of CW rotation, further promoting a run. However, if the cell is turning its motors CW such that it swims backward, the increasing kinase activity promotes CW rotation, further promoting the

backward movement. Therefore, the cell will continue backing away from the attractant source until the flagella randomly switch again. Thus, the modulation of the bias by the chemotaxis network will extend runs towards attractant sources and reversals away from attractant sources.

Given these problems with bias modulation, how do *H. pylori* undergo chemotaxis? It is possible that chemotaxis is inherently error-prone and inefficient in *H. pylori* compared to other chemotactic bacterial species. This notion should be tested in the future. Considering that polar flagellates likely experience oscillatory chemical levels as they run and reverse, what might be the role of putative methylation/demethylation enzymes in polar flagellates? Is methylation/demethylation necessary for chemotaxis? Future work on the kinetics of methylation and demethylation, and their resultant effects on chemotaxis, will shed light on some of these questions.

REFERENCES

1. CDC, *Antibiotic resistance threats in the United States*. (2019): Atlanta, GA: U.S. Department of Health and Human Services, CDC; 2019.

2. Berg HC, *E. coli in Motion*. (2008): Springer Science & Business Media.

3. Berg HC, *Random walks in biology*. (1993): Princeton University Press.

4. Cluzel P, Surette M, and Leibler S (2000) An ultrasensitive bacterial motor revealed by monitoring signaling proteins in single cells. *Science* **287**(5458): 1652-5.

5. Yuan J and Berg HC (2013) Ultrasensitivity of an adaptive bacterial motor. *J. Mol. Biol.* **425**(10): 1760-1764.

6. Belas R (2014) Biofilms, flagella, and mechanosensing of surfaces by bacteria. *Trends Microbiol.* **22**(9): 517-527.

7. Chawla R, Gupta R, Lele TP, and Lele PP (2020) A Skeptic's Guide to Bacterial Mechanosensing. *J. Mol. Biol.* **432**(2): 523-533.

8. Paulick A, Jakovljevic V, Zhang S, Erickstad M, Groisman A, Meir Y, Ryu WS, Wingreen NS, and Sourjik V (2017) Mechanism of bidirectional thermotaxis in *Escherichia coli*. *eLife* **6**: e26607.

9. Paster E and Ryu WS (2008) The thermal impulse response of *Escherichia coli*. *Proc. Natl. Acad. Sci. U.S.A.* **105**(14): 5373-5377.

10. Sourjik V and Berg HC (2002) Binding of the *Escherichia coli* response regulator CheY to its target measured in vivo by fluorescence resonance energy transfer. *Proc. Natl. Acad. Sci. U.S.A.* **99**(20): 12669-74.

11. Alon U, Surette MG, Barkai N, and Leibler S (1999) Robustness in bacterial chemotaxis. *Nature* **397**(6715): 168.

12. Lele PP, Hosu BG, and Berg HC (2013) Dynamics of mechanosensing in the bacterial flagellar motor. *Proc. Natl. Acad. Sci. U.S.A.* **110**(29): 11839-11844.

13. Wong GCL, Antani JD, Lele P, Chen J, Nan B, Kühn MJ, Persat A, Bru J-L, Høyland-Kroghsbo NM, and Siryaporn A (2021) Roadmap on emerging concepts in the physical biology of bacterial biofilms: from surface sensing to community formation. *Phys. Biol.*: https://doi.org/10.1088/1478-3975/abdc0e.

14. Chawla R, Ford KM, and Lele PP (2017) Torque, but not FliL, regulates mechanosensitive flagellar motor-function. *Sci. Rep.* **7**(1): 1-9.

15. Tipping MJ, Delalez NJ, Lim R, Berry RM, and Armitage JP (2013) Load-dependent assembly of the bacterial flagellar motor. *mBio* **4**(4): e00551-13.

16. Antani JD, Sumali AX, Lele TP, and Lele PP (2021) Asymmetric random walks reveal that the chemotaxis network modulates flagellar rotational bias in Helicobacter pylori. *eLife* **10**: e63936.

17. Katiyar A, Antani JD, McKee BP, Gupta R, Lele PP, and Lele TP (2021) A method for direct imaging of x–z cross-sections of fluorescent samples. *J. Microsc.* **281**(3): 224-230.

18. McCarter L, Hilmen M, and Silverman M (1988) Flagellar dynamometer controls swarmer cell differentiation of *V. parahaemolyticus*. *Cell* **54**(3): 345-351.

19. Hug I, Deshpande S, Sprecher KS, Pfohl T, and Jenal U (2017) Second messenger–mediated tactile response by a bacterial rotary motor. *Science* **358**(6362): 531-534.

20. Diethmaier C, Chawla R, Canzoneri A, Kearns DB, Lele PP, and Dubnau D (2017) Viscous drag on the flagellum activates *Bacillus subtilis* entry into the K-state. *Mol. Microbiol.* **106**(3): 367-380.

21. Waters CM and Bassler BL (2005) Quorum sensing: cell-to-cell communication in bacteria. *Annu. Rev. Cell Dev. Biol.* **21**: 319-346.

22. Berg HC and Purcell EM (1977) Physics of chemoreception. *Biophys. J.* **20**(2): 193-219.

23. Qi LS, Larson MH, Gilbert LA, Doudna JA, Weissman JS, Arkin AP, and Lim WA (2013) Repurposing CRISPR as an RNA-guided platform for sequence-specific control of gene expression. *Cell* **152**(5): 1173-1183.

24. Tuthill JC and Azim E (2018) Proprioception. *Curr. Biol.* **28**(5): R194-R203.

25. Harris CM, Dinges GF, Haberkorn A, Gebehart C, Büschges A, and Zill SN (2020) Gradients in mechanotransduction of force and body weight in insects. *Arthropod Str. Dev.* **58**: 100970.

26. Zill SN, Chaudhry S, Exter A, Büschges A, and Schmitz J (2014) Positive force feedback in development of substrate grip in the stick insect tarsus. *Arthropod Str. Dev.* **43**(5): 441-455.

27. Bastien R, Bohr T, Moulia B, and Douady S (2013) Unifying model of shoot gravitropism reveals proprioception as a central feature of posture control in plants. *Proc. Natl. Acad. Sci. U.S.A.* **110**(2): 755-760.

28. Okamoto K, Ueda H, Shimada T, Tamura K, Kato T, Tasaka M, Morita MT, and Hara-Nishimura I (2015) Regulation of organ straightening and plant posture by an actin–myosin XI cytoskeleton. *Nat. Plants* **1**(4): 1-7.

29. Berg HC (2003) The rotary motor of bacterial flagella. *Annu. Rev. Biochem.* **72**.

30. Sarkar MK, Paul K, and Blair D (2010) Chemotaxis signaling protein CheY binds to the rotor protein FliN to control the direction of flagellar rotation in *Escherichia coli*. *Proc. Natl. Acad. Sci. U.S.A.* **107**(20): 9370-9375.

31. Block SM, Segall JE, and Berg HC (1983) Adaptation kinetics in bacterial chemotaxis. *J. Bacteriol.* **154**(1): 312-323.

32. Sircar R, Borbat PP, Lynch MJ, Bhatnagar J, Beyersdorf MS, Halkides CJ, Freed JH, and Crane BR (2015) Assembly states of FliM and FliG within the flagellar switch complex. *J. Mol. Biol.* **427**(4): 867-886.

33. Yuan J, Branch RW, Hosu BG, and Berg HC (2012) Adaptation at the output of the chemotaxis signalling pathway. *Nature* **484**(7393): 233-236.

34. Sourjik V and Berg HC (2000) Localization of components of the chemotaxis machinery of *Escherichia coli* using fluorescent protein fusions. *Mol. Microbiol.* **37**(4): 740-751.

35. Lele PP, Branch RW, Nathan VSJ, and Berg HC (2012) Mechanism for adaptive remodeling of the bacterial flagellar switch. *Proc. Natl. Acad. Sci. U.S.A.* **109**(49): 20018-20022.

36. Santiveri M, Roa-Eguiara A, Kühne C, Wadhwa N, Hu H, Berg HC, Erhardt M, and Taylor NMI (2020) Structure and function of stator units of the bacterial flagellar motor. *Cell* **183**(1): 244-257.

37. Deme JC, Johnson S, Vickery O, Aron A, Monkhouse H, Griffiths T, James RH, Berks BC, Coulton JW, and Stansfeld PJ (2020) Structures of the stator complex that drives rotation of the bacterial flagellum. *Nat. Microbiol.* **5**(12): 1553-1564.

38. Guzman L-M, Belin D, Carson MJ, and Beckwith J (1995) Tight regulation, modulation, and high-level expression by vectors containing the arabinose PBAD promoter. *J. Bacteriol.* **177**(14): 4121-4130.

39. Ford KM, Antani JD, Nagarajan A, Johnson MM, and Lele PP (2018) Switching and torque generation in swarming *E. coli*. *Front. Microbiol.* **9**.

40. Manson MD, Tedesco PM, and Berg HC (1980) Energetics of flagellar rotation in bacteria. *J. Mol. Biol.* **138**(3): 541-561.

41. Blair DF and Berg HC (1988) Restoration of torque in defective flagellar motors. *Science* **242**(4886): 1678-1681.

42. Fahrner KA, Ryu WS, and Berg HC (2003) Biomechanics: bacterial flagellar switching under load. *Nature* **423**(6943): 938-938.

43. Yuan J, Fahrner KA, and Berg HC (2009) Switching of the bacterial flagellar motor near zero load. *J. Mol. Biol.* **390**(3): 394-400.

44. Lele PP, Shrivastava A, Roland T, and Berg HC (2015) Response thresholds in bacterial chemotaxis. *Sci. Adv.* **1**(9): e1500299.

45. Wang FB, Shi H, He R, Wang RJ, Zhang RJ, and Yuan JH (2017) Non-equilibrium effect in the allosteric regulation of the bacterial flagellar switch. *Nat. Phys.* **13**(7): 710-+.

46. Block SM, Segall JE, and Berg HC (1982) Impulse responses in bacterial chemotaxis. *Cell* **31**(1): 215-226.

47. Yuan J and Berg HC (2008) Resurrection of the flagellar rotary motor near zero load. *Proc. Natl. Acad. Sci. U.S.A.* **105**(4): 1182-1185.

48. Shimizu TS, Delalez N, Pichler K, and Berg HC (2006) Monitoring bacterial chemotaxis by using bioluminescence resonance energy transfer: Absence of feedback from the flagellar motors. *Proceedings of the National Academy of Sciences* **103**(7): 2093-2097.

49. Qin Z, Lin W-t, Zhu S, Franco AT, and Liu J (2017) Imaging the motility and chemotaxis machineries in *Helicobacter pylori* by cryo-electron tomography. *J. Bacteriol.* **199**(3): e00695-16.

50. Mariconda S, Wang Q, and Harshey RM (2006) A mechanical role for the chemotaxis system in swarming motility. *Mol. Microbiol.* **60**(6): 1590-1602.

51. Henrichsen J (1972) Bacterial surface translocation: a survey and a classification. *Bacteriol. Rev.* **36**(4): 478.

52. Pasupuleti S, Sule N, Cohn WB, MacKenzie DS, Jayaraman A, and Manson MD (2014) Chemotaxis of *Escherichia coli* to norepinephrine (NE) requires conversion of NE to 3, 4-dihydroxymandelic acid. *J. Bacteriol.* **196**(23): 3992-4000.

53. Berg HC and Block SM (1984) A miniature flow cell designed for rapid exchange of media under high-power microscope objectives. *Microbiology+* **130**(11): 2915-2920.

54. Peek Jr RM and Blaser MJ (2002) *Helicobacter pylori* and gastrointestinal tract adenocarcinomas. *Nat. Rev. Cancer.* **2**(1): 28.

55. Aihara E, Closson C, Matthis AL, Schumacher MA, Engevik AC, Zavros Y, Ottemann KM, and Montrose MH (2014) Motility and chemotaxis mediate the preferential colonization of gastric injury sites by *Helicobacter pylori*. *PLoS Pathog.* **10**(7): e1004275.

56. Ottemann KM and Lowenthal AC (2002) *Helicobacter pylori* uses motility for initial colonization and to attain robust infection. *Infect. Immun.* **70**(4): 1984-1990.

57. Constantino MA, Jabbarzadeh M, Fu HC, and Bansil R (2016) Helical and rod-shaped bacteria swim in helical trajectories with little additional propulsion from helical shape. *Sci. Adv.* **2**(11): e1601661.

58. Lauga E and Powers TR (2009) The hydrodynamics of swimming microorganisms. *Rep. Prog. Phys.* **72**(9): 096601.

59. Lertsethtakarn P, Ottemann KM, and Hendrixson DR (2011) Motility and Chemotaxis in *Campylobacter* and *Helicobacter*. *Annu. Rev. Microbiol.* **65**(1): 389-410.

60. Howitt MR, Lee JY, Lertsethtakarn P, Vogelmann R, Joubert L-M, Ottemann KM, and Amieva MR (2011) ChePep controls *Helicobacter pylori* infection of the gastric glands and chemotaxis in the Epsilonproteobacteria. *mBio* **2**(4): e00098-11.

61. Johnson KS and Ottemann KM (2018) Colonization, localization, and inflammation: the roles of *H. pylori* chemotaxis in vivo. *Curr. Opin. Microbiol.* **41**: 51-57.

62. Abedrabbo S, Castellon J, Collins KD, Johnson KS, and Ottemann KM (2017) Cooperation of two distinct coupling proteins creates chemosensory network connections. *Proc. Natl. Acad. Sci. U.S.A.* **114**(11): 2970-2975.

63. Lertsethtakarn P, Howitt MR, Castellon J, Amieva MR, and Ottemann KM (2015) *Helicobacter pylori* $CheZ_{HP}$ and ChePep form a novel chemotaxis-regulatory complex distinct from the core chemotaxis signaling proteins and the flagellar motor. *Mol. Microbiol.* **97**(6): 1063-1078.

64. Lowenthal AC, Simon C, Fair AS, Mehmood K, Terry K, Anastasia S, and Ottemann KM (2009) A fixed-time diffusion analysis method determines that the three cheV genes of *Helicobacter pylori* differentially affect motility. *Microbiology+* **155**(Pt 4): 1181.

65. Pittman MS, Goodwin M, and Kelly DJ (2001) Chemotaxis in the human gastric pathogen *Helicobacter pylori*: different roles for CheW and the three CheV paralogues, and evidence for CheV2 phosphorylation. *Microbiology+* **147**(9): 2493-2504.

66. Jiménez-Pearson M-A, Delany I, Scarlato V, and Beier D (2005) Phosphate flow in the chemotactic response system of *Helicobacter pylori*. *Microbiology+* **151**(10): 3299-3311.

67. Sourjik V and Wingreen NS (2012) Responding to chemical gradients: bacterial chemotaxis. *Curr. Opin. Cell. Biol.* **24**(2): 262-268.

68. Yang J, Chawla R, Rhee KY, Gupta R, Manson MD, Jayaraman A, and Lele PP (2020) Biphasic chemotaxis of *Escherichia coli* to the microbiota metabolite indole. *Proc. Natl. Acad. Sci. U.S.A.*: 201916974.

69. Scharf BE, Fahrner KA, Turner L, and Berg HC (1998) Control of direction of flagellar rotation in bacterial chemotaxis. *Proc. Natl. Acad. Sci. U.S.A.* **95**(1): 201-206.

70. Korobkova E, Emonet T, Vilar JMG, Shimizu TS, and Cluzel P (2004) From molecular noise to behavioural variability in a single bacterium. *Nature* **428**(6982): 574-578.

71. Collins KD, Andermann TM, Draper J, Sanders L, Williams SM, Araghi C, and Ottemann KM (2016) The *Helicobacter pylori* CZB Cytoplasmic Chemoreceptor TlpD Forms an Autonomous Polar Chemotaxis Signaling Complex That Mediates a Tactic Response to Oxidative Stress. *Infect. Immun.* **198**(11): 1563-1575.

72. Machuca MA, Johnson KS, Liu YC, Steer DL, Ottemann KM, and Roujeinikova A (2017) *Helicobacter pylori* chemoreceptor TlpC mediates chemotaxis to lactate. *Sci. Rep.* **7**(1): 1-15.

73. Sweeney EG, Henderson JN, Goers J, Wreden C, Hicks KG, Foster JK, Parthasarathy R, Remington SJ, and Guillemin K (2012) Structure and proposed mechanism for the pH-sensing *Helicobacter pylori* chemoreceptor TlpB. *Structure* **20**(7): 1177-1188.

74. Rader BA, Wreden C, Hicks KG, Sweeney EG, Ottemann KM, and Guillemin K (2011) *Helicobacter pylori* perceives the quorum-sensing molecule AI-2 as a chemorepellent via the chemoreceptor TlpB. *Microbiology+* **157**(Pt 9): 2445.

75. Sanders L, Andermann TM, and Ottemann KM (2013) A supplemented soft agar chemotaxis assay demonstrates the *Helicobacter pylori* chemotactic response to zinc and nickel. *Microbiology+* **159**(Pt 1): 46.

76. Schweinitzer T, Mizote T, Ishikawa N, Dudnik A, Inatsu S, Schreiber S, Suerbaum S, Aizawa S-I, and Josenhans C (2008) Functional characterization and mutagenesis of the proposed behavioral sensor TlpD of *Helicobacter pylori*. *J. Bacteriol.* **190**(9): 3244-3255.

77. Lowenthal AC, Hill M, Sycuro LK, Mehmood K, Salama NR, and Ottemann KM (2009) Functional Analysis of the *Helicobacter pylori* Flagellar Switch Proteins. *J. Bacteriol.* **191**(23): 7147-7156.

78. Ford KM, Chawla R, and Lele PP (2017) Biophysical characterization of flagellar motor functions. *JoVE* (119): e55240.

79. Yuan J, Fahrner KA, Turner L, and Berg HC (2010) Asymmetry in the clockwise and counterclockwise rotation of the bacterial flagellar motor. *Proc. Natl. Acad. Sci. U.S.A.* **107**(29): 12846-12849.

80. Stocker R (2011) Reverse and flick: Hybrid locomotion in bacteria. *Proc. Natl. Acad. Sci. U.S.A.* **108**(7): 2635-2636.

81. DiLuzio WR, Turner L, Mayer M, Garstecki P, Weibel DB, Berg HC, and Whitesides GM (2005) *Escherichia coli* swim on the right-hand side. *Nature* **435**(7046): 1271-1274.

82. Lauga E, DiLuzio WR, Whitesides GM, and Stone HA (2006) Swimming in circles: motion of bacteria near solid boundaries. *Biophys. J.* **90**(2): 400-412.

83. Segall JE, Block SM, and Berg HC (1986) Temporal comparisons in bacterial chemotaxis. *Proc. Natl. Acad. Sci. U.S.A.* **83**(23): 8987-8991.

84. Sagawa T, Kikuchi Y, Inoue Y, Takahashi H, Muraoka T, Kinbara K, Ishijima A, and Fukuoka H (2014) Single-cell *E. coli* response to an instantaneously applied chemotactic signal. *Biophys. J.* **107**(3): 730-739.

85. Stock J, Kersulis G, and Koshland Jr DE (1985) Neither methylating nor demethylating enzymes are required for bacterial chemotaxis. *Cell* **42**(2): 683-690.

86. Liu G, Tao A, Zhang R, and Yuan J (2020) Robustness in an Ultrasensitive Motor. *mBio* **11**(2).

87. Huang JY, Sweeney EG, Sigal M, Zhang HC, Remington SJ, Cantrell MA, Kuo CJ, Guillemin K, and Amieva MR (2015) Chemodetection and destruction of host urea allows *Helicobacter pylori* to locate the epithelium. *Cell Host Microbe* **18**(2): 147-156.

88. Perkins A, Tudorica DA, Amieva MR, Remington SJ, and Guillemin K (2019) *Helicobacter pylori* senses bleach (HOCl) as a chemoattractant using a cytosolic chemoreceptor. *PLoS Biol.* **17**(8).

89. Martínez LE, Hardcastle JM, Wang J, Pincus Z, Tsang J, Hoover TR, Bansil R, and Salama NR (2016) *Helicobacter pylori* strains vary cell shape and flagellum number to maintain robust motility in viscous environments. *Mol. Microbiol.* **99**(1): 88-110.

90. Yuan J and Berg HC (2010) Thermal and solvent-isotope effects on the flagellar rotary motor near zero load. *Biophys. J.* **98**(10): 2121-2126.

91. Turner L, Caplan SR, and Berg HC (1996) Temperature-induced switching of the bacterial flagellar motor. *Biophys. J.* **71**(4): 2227.

92. Turner L, Samuel ADT, Stern AS, and Berg HC (1999) Temperature dependence of switching of the bacterial flagellar motor by the protein $CheY^{13DK106YW}$. *Biophys. J.* **77**(1): 597-603.

93. Fukuoka H, Sagawa T, Inoue Y, Takahashi H, and Ishijima A (2014) Direct imaging of intracellular signaling components that regulate bacterial chemotaxis. *Sci. Signal.* **7**(319): ra32-ra32.

94. Josenhans C and Suerbaum S (2002) The role of motility as a virulence factor in bacteria. *Int. J. Med. Microbiol.* **291**(8): 605-614.

95. Lovely PS and Dahlquist F (1975) Statistical measures of bacterial motility and chemotaxis. *J. Theor. Biol.* **50**(2): 477-496.

96. Lauga E (2016) Bacterial hydrodynamics. *Annu. Rev. Fluid Mech.* **48**: 105-130.

97. Theves M, Taktikos J, Zaburdaev V, Stark H, and Beta C (2013) A bacterial swimmer with two alternating speeds of propagation. *Biophys. J.* **105**(8): 1915-1924.

98. Morse M, Colin R, Wilson LG, and Tang JX (2016) The aerotactic response of *Caulobacter crescentus*. *Biophys. J.* **110**(9): 2076-2084.

99. Xie L, Altindal T, Chattopadhyay S, and Wu X-L (2011) Bacterial flagellum as a propeller and as a rudder for efficient chemotaxis. *Proc. Natl. Acad. Sci. U.S.A.* **108**(6): 2246-2251.

100. Großmann R, Peruani F, and Bär M (2016) Diffusion properties of active particles with directional reversal. *New J. Phys.* **18**(4): 043009.

101. Detcheverry F (2017) Generalized run-and-turn motions: From bacteria to Lévy walks. *Phys. Rev. E* **96**(1): 012415.

102. Montrone M, Eisenbach M, Oesterhelt D, and Marwan W (1998) Regulation of Switching Frequency and Bias of the Bacterial Flagellar Motor by CheY and Fumarate. *J. Bacteriol.* **180**(13): 3375-3380.

103. Jasuja R, Keyoung J, Reid GP, Trentham DR, and Khan S (1999) Chemotactic responses of *Escherichia coli* to small jumps of photoreleased L-aspartate. *Biophys. J.* **76**(3): 1706-1719.

104. Dominick CN and Wu X-L (2018) Rotating bacteria on solid surfaces without tethering. *Biophys. J.* **115**(3): 588-594.

105. Lele PP, Roland T, Shrivastava A, Chen Y, and Berg HC (2016) The flagellar motor of *Caulobacter crescentus* generates more torque when a cell swims backwards. *Nat. Phys.* **12**(2): 175-178.

106. Sourjik V, Vaknin A, Shimizu TS, and Berg HC, *In vivo measurement by FRET of pathway activity in bacterial chemotaxis*, in *Method Enzymol.* (2007), Elsevier. p. 365-391.

107. Magariyama Y, Ichiba M, Nakata K, Baba K, Ohtani T, Kudo S, and Goto T (2005) Difference in bacterial motion between forward and backward swimming caused by the wall effect. *Biophys. J.* **88**(5): 3648-3658.

108. Kinosita Y, Kikuchi Y, Mikami N, Nakane D, and Nishizaka T (2018) Unforeseen swimming and gliding mode of an insect gut symbiont, *Burkholderia* sp. RPE64, with wrapping of the flagella around its cell body. *ISME J.* **12**(3): 838-848.

109. Liu B, Gulino M, Morse M, Tang JX, Powers TR, and Breuer KS (2014) Helical motion of the cell body enhances *Caulobacter crescentus* motility. *Proc. Natl. Acad. Sci. U.S.A.* **111**(31): 11252-11256.

110. Spohn G and Scarlato V (1999) Motility of *Helicobacter pylori* is coordinately regulated by the transcriptional activator FlgR, an NtrC homolog. *J. Bacteriol.* **181**(2): 593-599.

111. Lele PP and Berg HC (2015) Switching of bacterial flagellar motors triggered by mutant FliG. *Biophys. J.* **108**(5): 1275-1280.

112. Lam KH, Ling TKW, and Au SWN (2010) Crystal structure of activated CheY1 from *Helicobacter pylori*. *J. Bacteriol.* **192**(9): 2324-2334.

113. Arnold IC, Lee JY, Amieva MR, Roers A, Flavell RA, Sparwasser T, and Müller A (2011) Tolerance rather than immunity protects from Helicobacter pylori–induced gastric preneoplasia. *Gastroenterology* **140**(1): 199-209.

114. Huang JY, Sweeney EG, Guillemin K, and Amieva MR (2017) Multiple acid sensors control *Helicobacter pylori* colonization of the stomach. *PLoS Pathog.* **13**(1).

115. Crocker JC and Grier DG (1996) Methods of digital video microscopy for colloidal studies. *J. Colloid. Interf. Sci.* **179**(1): 298-310.

116. Thomas DR, Francis NR, Xu C, and DeRosier DJ (2006) The three-dimensional structure of the flagellar rotor from a clockwise-locked mutant of *Salmonella enterica serovar* Typhimurium. *J. Bacteriol.* **188**(20): 7039-7048.

117. Mikhailov A and Meinköhn D. *Self-motion in physico-chemical systems far from thermal equilibrium*. 1997. Berlin, Heidelberg: Springer Berlin Heidelberg.

118. Schienbein M and Gruler H (1993) Langevin equation, Fokker-Planck equation and cell migration. *B. Math. Biol.* **55**(3): 585-608.

119. Karatan E, Saulmon MM, Bunn MW, and Ordal GW (2001) Phosphorylation of the response regulator CheV is required for adaptation to attractants during *Bacillus subtilis* chemotaxis. *J. Biol. Chem.* **276**(47): 43618-43626.

120. Rao CV, Glekas GD, and Ordal GW (2008) The three adaptation systems of *Bacillus subtilis* chemotaxis. *Trends Microbiol.* **16**(10): 480-487.

121. Schreiber S, Bücker R, Groll C, Azevedo-Vethacke M, Garten D, Scheid P, Friedrich S, Gatermann S, Josenhans C, and Suerbaum S (2005) Rapid loss of motility of *Helicobacter pylori* in the gastric lumen in vivo. *Infect. Immun.* **73**(3): 1584-1589.

122. Mobley HL, Cortesia MJ, Rosenthal LE, and Jones BD (1988) Characterization of urease from *Campylobacter pylori*. *J. Clin. Microbiol.* **26**(5): 831-836.

123. Ansari S and Yamaoka Y (2017) Survival of *Helicobacter pylori* in gastric acidic territory. *Helicobacter* **22**(4): e12386.

124. Diaspro A, Federici F, and Robello M (2002) Influence of refractive-index mismatch in high-resolution three-dimensional confocal microscopy. *Appl. Optics* **41**(4): 685-690.

125. Hell S, Reiner G, Cremer C, and Stelzer EHK (1993) Aberrations in confocal fluorescence microscopy induced by mismatches in refractive index. *J. Microsc.* **169**(3): 391-405.

126. Diel EE, Lichtman JW, and Richardson DS (2020) Tutorial: avoiding and correcting sample-induced spherical aberration artifacts in 3D fluorescence microscopy. *Nat. Protoc.* **15**(9): 2773-2784.

127. Kuypers LC, Decraemer WF, Dirckx JJJ, and Timmermans JP (2005) A procedure to determine the correct thickness of an object with confocal microscopy in case of refractive index mismatch. *J. Microsc.* **218**(1): 68-78.

128. Van Elburg HJ, Kuypers LC, Decraemer WF, and Dirckx JJJ (2007) Improved correction of axial geometrical distortion in index-mismatched fluorescent confocal microscopic images using high-aperture objective lenses. *J. Microsc.* **228**(1): 45-54.

129. Feric M, Vaidya N, Harmon TS, Mitrea DM, Zhu L, Richardson TM, Kriwacki RW, Pappu RV, and Brangwynne CP (2016) Coexisting liquid phases underlie nucleolar subcompartments. *Cell* **165**(7): 1686-1697.

130. Hobson CM, Kern M, O'Brien Iii ET, Stephens AD, Falvo MR, and Superfine R (2020) Correlating nuclear morphology and external force with combined atomic force microscopy and light sheet imaging separates roles of chromatin and lamin A/C in nuclear mechanics. *Mol. Biol. Cell* **31**(16): 1788-1801.

131. Diaspro A, Chirico G, Usai C, Ramoino P, and Dobrucki J, *Photobleaching*, in *Handbook of biological confocal microscopy*. (2006), Springer. p. 690-702.

132. Li Y, Lovett D, Zhang Q, Neelam S, Kuchibhotla RA, Zhu R, Gundersen GG, Lele TP, and Dickinson RB (2015) Moving cell boundaries drive nuclear shaping during cell spreading. *Biophys. J.* **109**(4): 670-686.

133. Howard J, *Mechanics of Motor Proteins and the Cytoskeleton*. (2001): Sinauer Associates, Publishers.

134. Sheppard CJR and Török P (1997) Effects of specimen refractive index on confocal imaging. *J. Microsc.* **185**(3): 366-374.

135. Ingram VM (1969) A Side View of Moving Fibroblasts. *Nature* **222**(5194): 641-644.

APPENDIX A

APPENDIX TO CHAPTER 3

A.1. Raw data for CW_{bias}

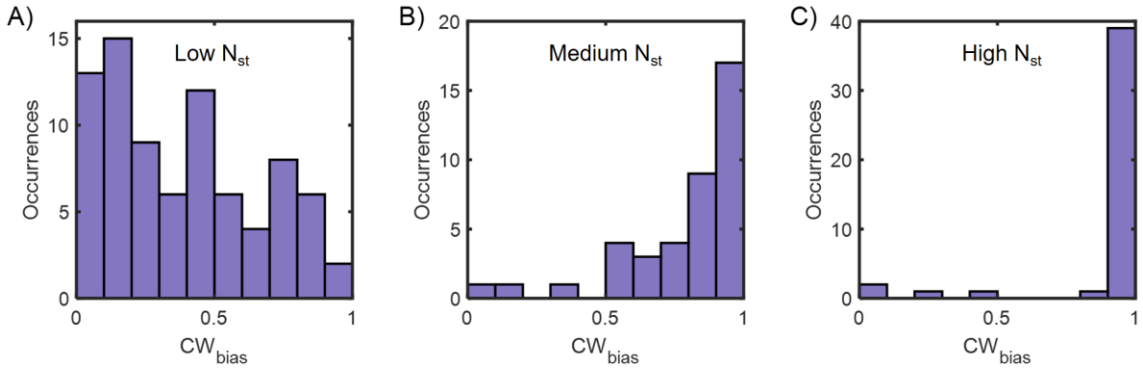

Appendix A Figure 1. Raw data for Figure 3-2B.
CW_{bias} histograms for the populations with A) low, B) medium, and C) high N_{st}.

A.2. Predicting CW_{bias} versus [CheY-P] relationship from CW_{bias} distributions

The random variables B and C represent the variability in CW_{bias} and [CheY-P] in a cell population, respectively. The random variable C (CheY-P level) is assumed to be normally distributed with a mean μ and standard deviation σ. The bias B at each C is calculated from the Hill function:

$$B = \frac{C^h}{C^h + K_D^h}$$

where h and K_D represent the Hill coefficient and the dissociation constant, respectively. We derive the probability density for the bias from the following expression [44]:

$$P(B) = f(\phi)\frac{d\phi}{dB}$$

where,

$$\phi(B) = C = K_D\left(\frac{B}{1-B}\right)^{\frac{1}{h}} = K_D\left(\frac{1}{B}-1\right)^{-\frac{1}{h}}$$

and $f(\phi)$ is the Gaussian function that describes the [CheY-P] distribution.

The expression for the CW_{bias} distribution is:

$$P(B) = \frac{K_D}{hB^2\sigma\sqrt{2\pi}}\left(\frac{1}{B}-1\right)^{-\frac{1}{h}-1}\exp\left(-\frac{1}{2}\frac{\left(K_D\left(\frac{1}{B}-1\right)^{-\frac{1}{h}}-\mu\right)^2}{\sigma^2}\right) \quad \text{Equation 1}$$

We assumed h = 10 and K_D = 3.1 μM for motors with a full complement of stator units (high torque group) based on an earlier work [4]. This is a reasonable assumption as the measurements of Cluzel and co-workers [4] were performed at high loads where the stator carries a full complement of stator units. We used a nonlinear least-square approach to fit equation 1 to the CW_{bias} distribution in the high torque group. This yielded $\mu = 5.3 \pm 0.5$ μM for the *ΔcheRcheBcheZ* cells. For the medium and low torque groups, we assumed that the μ and σ remained fixed while K_D was a free parameter. The fitted values of K_D for the different groups are shown below. The fits to the CW_{bias} distributions are indicated in the plots.

Appendix A Table 1. Nonlinear least-square fitting to probability densities shown in Figure 3-2B.

For the high N_{st} group, μ was considered a free parameter whereas for the other groups, K_D was a free parameter.

High N_{st}	**Medium N_{st}**	**Low N_{st}**
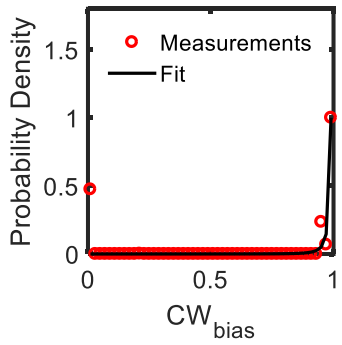	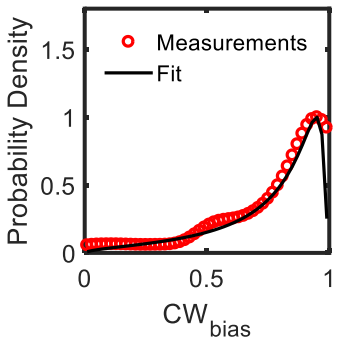	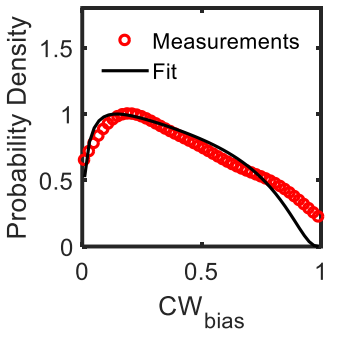
$K_D = 3.1$ μM	$K_D = 4.5 \pm 0.0$ μM	$K_D = 5.6 \pm 0.0$ μM

The nature of K_D's dependence on torque did not change when we assumed different values for μ and σ.

A.3. Estimation of CW_{bias} at varying viscous loads

The CW_{bias} was calculated from CCW-to-CW ($k_{CCW\to CW}$) and CW-to-CCW ($k_{CW\to CCW}$) switching rates from previous works [42, 43]:

$$CW_{bias} = \frac{k_{CCW\to CW}}{k_{CCW\to CW} + k_{CW\to CCW}}$$

A.4. Optical Trapping + TIRF Setup

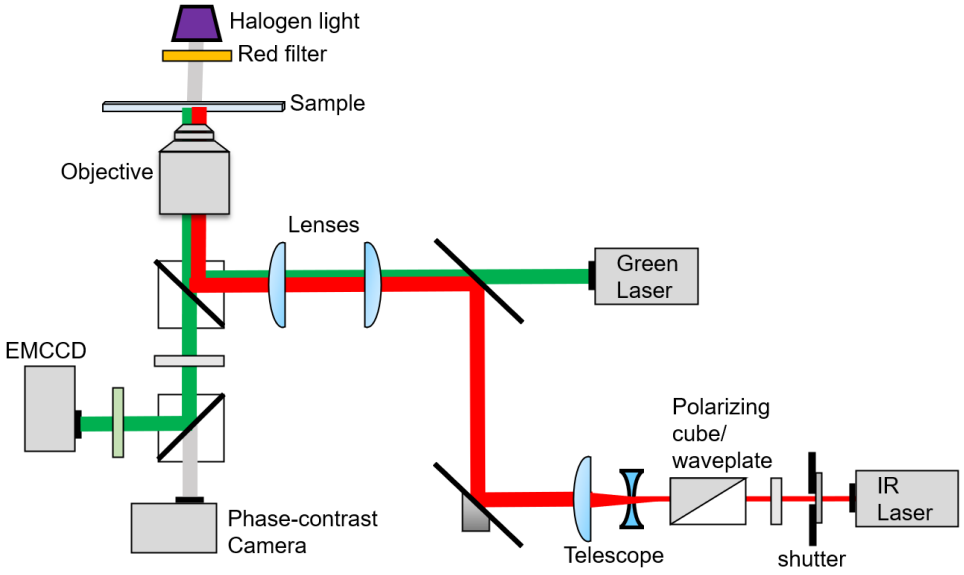

Appendix A Figure 2. Setup for combined optical trapping (red laser) and TIRF illumination (green).

A.5. Point of tether in tethered cells

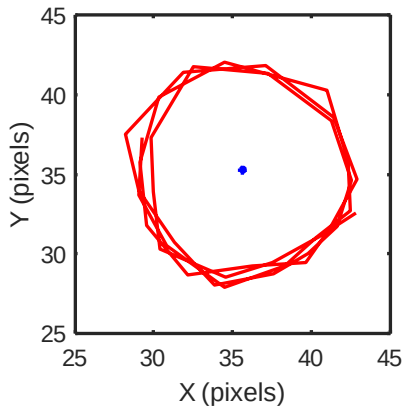

Appendix A Figure 3. Point of tether in tethered cells.

The red trajectory shows the movements of the center-of-mass of a tethered cell. The center-of-mass was obtained from each image by fitting an ellipse to the cell. The tether point (motor location) coincides with the center of a circular fit to the trajectory.

A.6. Strains and Plasmids

Appendix A Table 2. Plasmids used in Chapter 3.

Plasmid	Plasmid No.	Resistance	Cloning Sites
pBAD34-motAmotB	pPL39	Chloramphenicol	KpnI & SalI
pTrc99A-eyfp-cheY	pPL29	Ampicillin	KpnI & XbaI

Appendix A Table 3. Strains used in Chapter 3 (black) and intermediate lab strains (gray)

Strain name	Lab Strain #	Genotype	Plasmid
MotA/MotB, Fig 1B	PL240	*fliCst ΔcheRcheBcheYcheZ*	*pTrc99A-eyfp-cheY*
Δ*motAB*, Fig 1B	PL239	*fliCst ΔcheRcheBcheYcheZ, ΔmotAmotB*	*pTrc99A-eyfp-cheY*
Δ*motAB*/p(empty), Fig 1C	PL349	*fliCst ΔcheRcheBcheYcheZ, ΔmotAmotB*	*pTrc99A-eyfp-cheY pBAD34*
Δ*motAB*/p(MotAB), Fig 1C	PL350	*fliCst ΔcheRcheBcheYcheZ, ΔmotAmotB*	*pTrc99A-eyfp-cheY pBAD34-motAmotB*
MotA/MotB, Fig 1D	PL233	*fliCst fliM-eYFP(A206K)-fliM ΔcheY*	
Δ*motAB*, Fig 1D	PL333	*fliCst fliM-eYFP(A206K)-fliM ΔmotAmotB ΔcheY*	
Δ*cheRcheBcheZ*, Fig 2A, B	PL254	*fliCst ΔcheRcheBcheZ ΔmotAmotB*	*pBAD34-motAmotB*
Δ*cheRcheB*, Fig 2E	PL138	*fliCst ΔcheRcheB*	

A.7. Biophysical model: mechanosensory modulation of the switch

We concluded in Chapter 3 that the torque developed by the stators modulates the binding of the response regulator, CheY-P, to the motor. This results in precise adaptation in the CW_{bias} to changes in the external viscous load. To model our observations, we propose an extension of an existing model of the flagellar switch [69]. In this model, the flagellar motor has two conformations: CCW and CW, with the free energy difference ΔG between them (Appendix A Figure 4A). The CW_{bias} can be expressed in terms of CheY-P binding and unbinding rates (k_+ and k_- respectively). Scharf and coworkers [69] derived an analytical expression for the ratio of k_+ and k_-:

$$\frac{k_+}{k_-} = \frac{CW_{bias}}{1 - CW_{bias}}$$

$$= \exp\left(-\frac{\Delta G}{kT}\right) = \exp\left[-\frac{\Delta G_0}{kT} + \mathrm{M}\ln\left(\frac{K_{CCW}}{K_{CW}}\right)\left(\frac{C}{C + K_D}\right)\right]$$

Where, ΔG_0 is ΔG in absence of any bound molecules; M is the number of CheY-P binding sites in the flagellar motor ($M = 34$ as observed by reference [116]); K_{CCW} and K_{CW} are dissociation constants for CheY-P binding to the CCW and CW conformations, respectively (In *E. coli*, $K_{CCW}/K_{CW} = 4.7$ [93]); C is the intracellular concentration of CheY-P; and K_D is the dissociation constant for CheY-P binding to the motor. This expression leads to a sigmoidal relationship between CW_{bias} and C=[CheY-P].

Our results discussed in Chapter 2 suggest that K_D decreases with an increase in the number of stator units bound to the motor (N_{st}). In the above model, a decrease in K_D shifts the CW_{bias} vs [CheY-P] curve to the left (Appendix A Figure 4B), which is

consistent with our observations reported in Figure 3-2. An increase in ΔG_0 shifts the curve to the right (Appendix A Figure 4C). We propose the following scheme (Appendix A Figure 4D) to explain simultaneous remodeling of stators and CW_{bias}:

$$\Delta G_0 = f(\tau)$$

$$K_D = g(N_{st})$$

Where, τ is the motor torque, f is an increasing function of τ, and g is a decreasing function of K_D. A flagellar motor with a load-free stub rotates with a very low toque τ and a small N_{st} (① in Appendix A Figure 4D *left*). When the flagellar stub adheres to a bead or a surface, the torque immediately increases. As a result, ΔG_0 increases significantly and the CW_{bias} versus [CheY-P] curve shifts to the right (black to red curves in Appendix A Figure 4C, D). The number of bound stators, N_{st}, and hence, K_D, do not change immediately. However, based on [CheY-P] characteristic to the bacterium (dashed black line in Appendix A Figure 4D), the CW_{bias} drops to zero (② in Appendix A Figure 4D *left*). As the stator remodels by recruiting more units (N_{st}), K_D decreases, and the curve shifts to the left as in Appendix A Figure 4B. τ also increases as additional stator units bind to the rotor, however, we anticipate that the effect of N_{st} on K_D is much more significant than its effect on τ and thus ΔG_0. As a result of a decrease in K_D, the red curve shifts to the blue curve at medium N_{st}, and the CW_{bias} increases (③ in Appendix A Figure 4D *left*). The CW_{bias} eventually goes back to the pre-stimulus, steady state value (④ in Appendix A Figure 4D *left*). Thus, these events reflect the perfect adaptation in CW_{bias} concurrent to the stator remodeling.

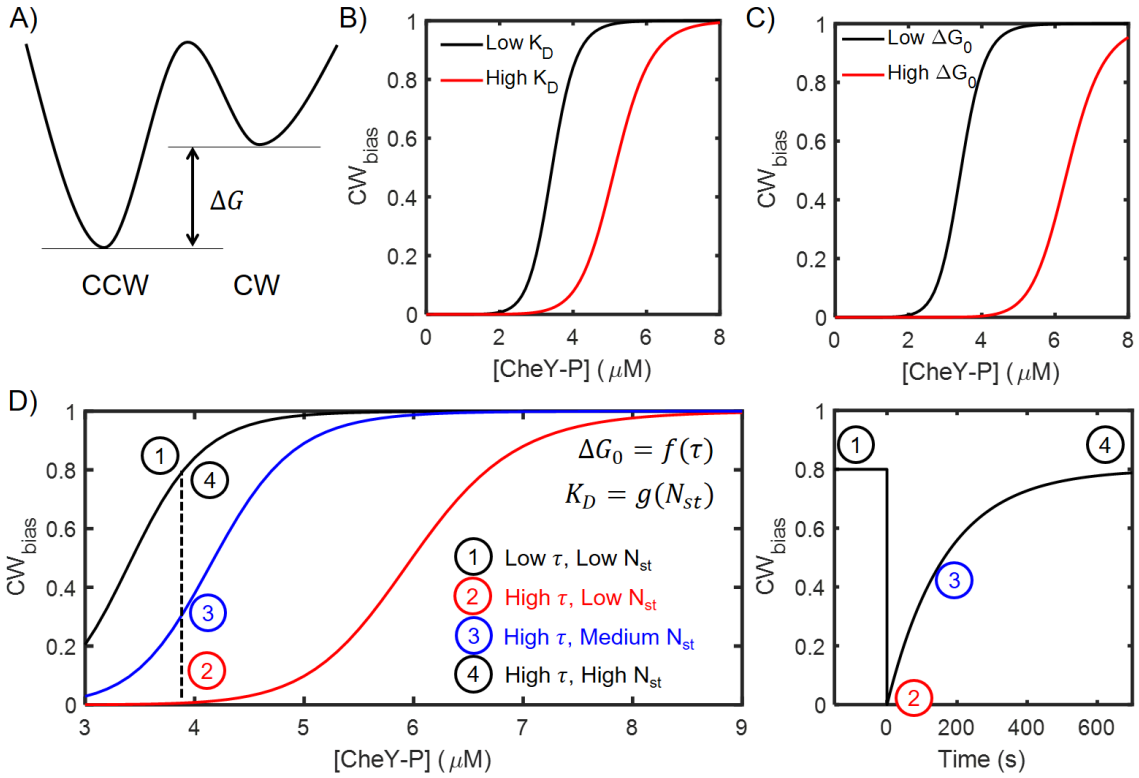

Appendix A Figure 4. Biophysical model for mechanosensory modulation of the switch. **A)** The flagellar switch is bistable: the CW and CCW conformations have a free energy difference of ΔG. **B)** CW_{bias} versus [CheY-P] relationship was obtained from the analytical model by Scharf and coworkers [69]. The sigmoidal curve shifts to the left upon a decrease in K_D. **C)** The curve shifts to the right upon an increase in ΔG_0. **D)** We propose this scheme for remodeling in CW_{bias} concurrent to stator remodeling (*right*). *Left*: The steady state CW_{bias} versus [CheY-P] curve is shown in black. We discuss the case of a cell with [CheY-P] ~ 3.9 μM (dashed black line). ① The cell initially has a flagellar stub rotating at steady-state with N_{st} = 1 or 2 stator units bound to the motor. ② As the flagellar stub adheres to a surface or a bead (a viscous load), the torque on motor increases significantly, which results in a dramatic increase in ΔG_0, and a shift to the right. According to this red curve, CW_{bias} = 0 for the value of [CheY-P] in this cell. ③ As time passes, the motor recruits additional stator units, so N_{st} increases, which results in a decrease in K_D. This shifts the curve to the right (red to blue). The CW_{bias} climbs up the dashed black line to meet the blue curve. ④ Upon further recruitment of stator units

(Appendix A Figure 4 Continued…)
(high N_{st}) case, the CW_{bias} perfectly adapts to the steady state level. While the CWbias follows the dashed black line on the left figure, the temporal variation in CW_{bias} is shown on the right.

This model can be incorporated in future works about flagellar mechanosensing. We speculate that such force-mediated adaptation mechanisms may be spread wider in the bacterial and the larger biological worlds.

APPENDIX B

APPENDIX TO CHAPTER 4

B.1. Δ*cheY* cells swim in the pusher mode only

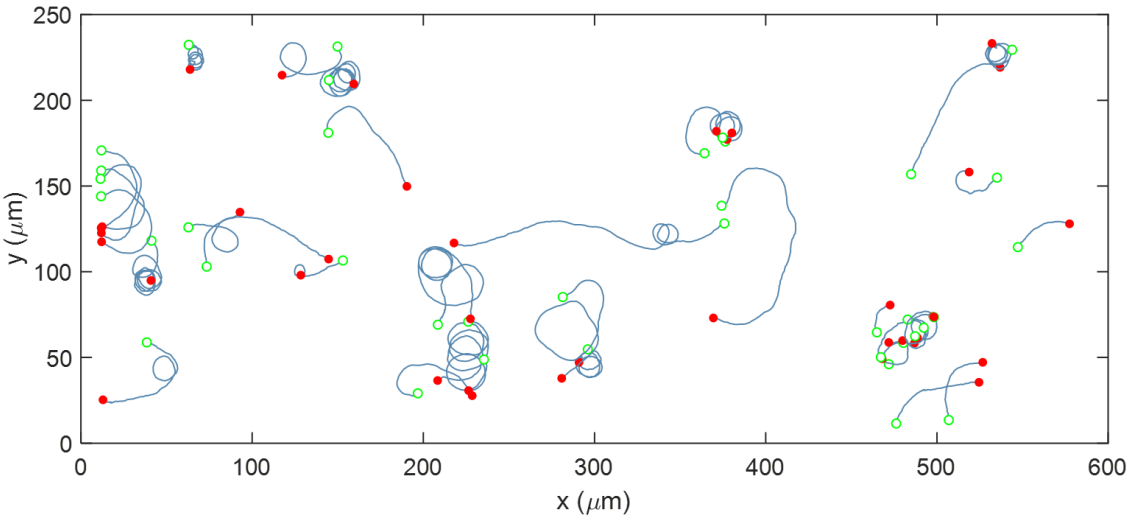

Appendix B Figure 1. Single cell trajectories of a *H. pylori* PMSS1 ΔcheY mutant. The cells swam in clockwise-only trajectories as shown: open green circles denote the start of a trajectory; filled red circles denote the end. This behavior was observed for n > 150 cells; here we show 38 cells. Reprinted with permission from [16].

B.2. Estimation of dissociation constants

The rate constants for flagellar switching from CCW to CW ($k_{CCW\rightarrow CW}$) and CW to CCW ($k_{CW\rightarrow CCW}$) were estimated from the CW_{bias} and the reversal frequencies, ω:

$$k_{CCW\rightarrow CW} = \frac{\omega}{2(1 - CW_{bias})}$$

$$k_{CW\rightarrow CCW} = \frac{\omega}{2CW_{bias}}$$

As shown in Appendix B Figure 2, both rate constants increased until the physiological temperature (37 °C) was attained; the rates decreased thereafter. Reliable

estimates of the rate constants could not be obtained at 25 °C, owing to the low frequency of reversals at that temperature.

Following the model of Scharf and co-workers [69], the ratio of the dissociation constant (*K*) to the concentration of the phosphorylated CheY (*C*) was calculated from:

$$\ln(K_{eq}) = \frac{-\Delta G^0}{kT} + m.\ln\left(K_{CCW}/K_{CW}\right)\frac{C}{C+K}$$

where $K_{eq} = \frac{CW_{bias}}{1-CW_{bias}}$, and *K* is the weighted average of the dissociation constants, K_{CCW} and K_{CW}, for CheY-P binding to the CCW and CW conformations, respectively. We assumed K_{CCW}/K_{CW} = 4.7 from an earlier work in *E. coli* [93]. The standard free energy difference between the CW and CCW conformations in the absence of CheY-P, ΔG^0, was estimated at the temperatures used in our work by extrapolating previous data [91]. The number of CheY-P binding sites in the flagellar switch in *H. pylori*, was determined from the ratio of the sizes of the switch complexes in the two species [49]: $m_{H.pylori} = m_{E.coli}\left(\frac{Diameter_{E.\ coli\ switch}}{Diameter_{H.\ pylori\ switch}}\right)$ where $m_{E.coli} = 34$ [35] .

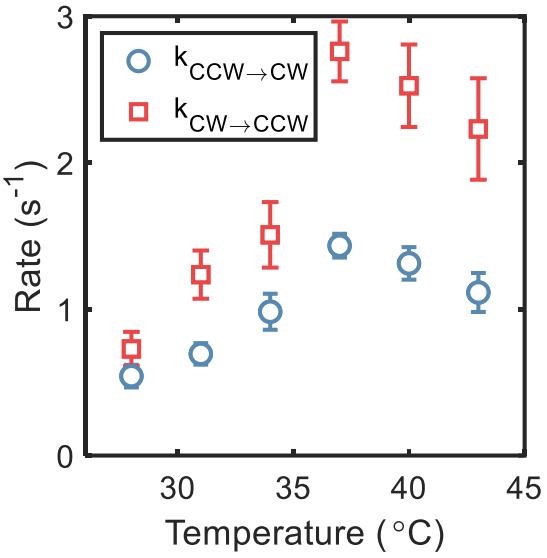

Appendix B Figure 2. The switching rates were estimated from the CW_{bias} and the reversal frequencies reported in Figure 4-4B.

The maximum $k_{CW \to CCW}$ and $k_{CCW \to CW}$ values were attained at 37 °C (2.75 ± 0.20 s^{-1} and 1.43 ± 0.08 s^{-1}). The standard error is indicated. Reprinted with permission from [16].

B.3. Wait-times for pusher and puller modes

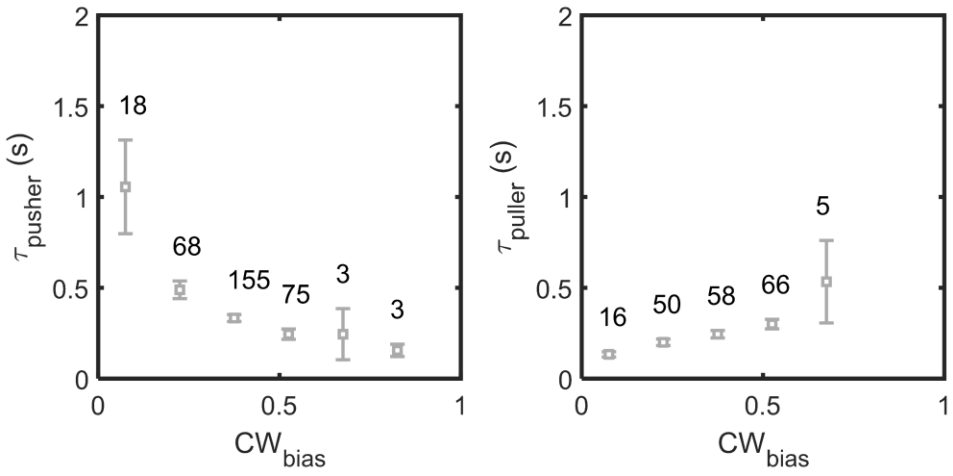

Appendix B Figure 3. Variation in wait-times in pusher and puller modes with CW_{bias}.

Each point on the plot is calculated by averaging over the number of samples noted above the point. Reprinted with permission from [16].

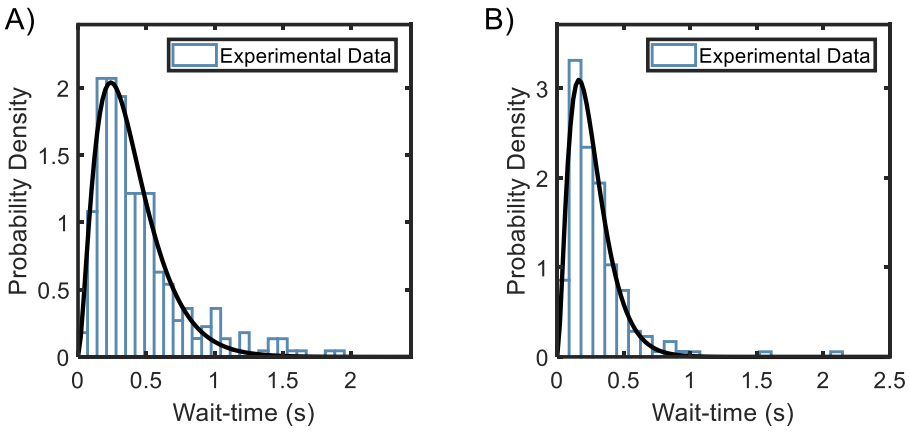

Appendix B Figure 4. Wait-time distributions.

A) pusher mode (n = 322 segments) and **B)** puller mode (n = 196 segments). Gamma-fits reveal that the mean ± variance in wait-times for the pusher mode is 0.38 ± 0.06 and that for the puller mode is 0.26 ± 0.02. Reprinted with permission from [16].

B.4. Diffusion model for asymmetric swimmers

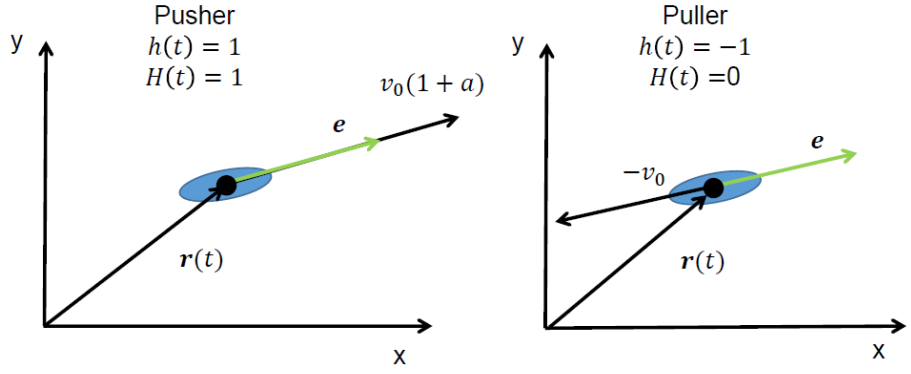

Appendix B Figure 5. Diffusion model schematic.

Cell alignment and position are defined by the vectors $\boldsymbol{e}$ and $\boldsymbol{r}$. Function $h(t)$ alternates between -1 and 1 with each reversal. The Heaviside function, $H(h)$, describes the magnitudes of the two swimming modes with the asymmetry parameter a. Reprinted with permission from [16].

The velocity of the bacterium is expressed as:

$$\frac{d\boldsymbol{r}(t)}{dt} = \boldsymbol{v}(t) = v_0\, \boldsymbol{e}(t)\, h(t)\, [1 + aH(t)] \tag{1}$$

where the unit vector $\boldsymbol{e}(t)$ represents cell alignment. The state function $h(t)$ describes the direction of swimming, and alternates between $h(t) = 1$ and $h(t) = -1$ to indicate the two modes (Appendix B Figure 5).

$$h(t) = \begin{cases} 1, & pusher \\ -1, & puller \end{cases}$$

A Heaviside function $H(t)$ characterizes the difference in swimming speeds in the two modes:

$$H(t) = \begin{cases} 1, & h(t) = 1 \\ 0, & h(t) = -1 \end{cases}$$

Thus, the magnitudes of the two speeds are, $v_{pusher} = (1 + a)v_0$ and $v_{puller} = v_{0,}$ where a is the asymmetry parameter.

Rotational diffusion causes the cell to deviate from a straight line during a run (or reversal), described by $\frac{d\theta}{dt} = \sqrt{2D_\theta}\xi(t)$, where the white noise is characterized by $\langle \xi(t) \rangle = 0$, and $\langle \xi(t)\xi(t+\tau) \rangle = \delta(-\tau)$. D_θ is the rotational diffusion coefficient.

The velocity autocorrelation is:

$$\langle \boldsymbol{v}(t)\boldsymbol{v}(t+\tau) \rangle = v_0^2 \langle \boldsymbol{e}(t)\boldsymbol{e}(t+\tau) \rangle \langle G(t,\tau) \rangle \tag{2}$$

here, $G(t,\tau) = h(t)h(t+\tau)[1 + aH(t)][1 + aH(t+\tau)]$ (3)

Also, $\langle \boldsymbol{e}(t) \cdot \boldsymbol{e}(t+\tau) \rangle = e^{-D_\theta \tau}$ [117, 118]

The value of G in time τ is influenced by the number of reversals, k, whether they are odd or even, and the initial mode of swimming at t (see Appendix B Table 1).

Appendix B Table 1. Value of $G(t,\tau)$ for different possibilities.

Number of Reversals	$h(t)$	$h(t+\tau)$	$H(t)$	$H(t+\tau)$	$G(t,\tau)$
Even	1	1	1	1	$(1+a)^2$
Even	-1	-1	0	0	1
Odd	1	-1	1	0	$-(1+a)$
Odd	-1	1	0	1	$-(1+a)$

For odd or even number of reversals occurring between time t and $t+\tau$, corresponding cases of initial and final values for state function *h* and Heaviside function *H* are considered. Substituting h and H values in (3), *G* is calculated for each case.

Based on Appendix B Table 1, the average value of the correlation can be determined from the probabilities of k reversals, $P_k^{h(t),h(t+\tau)}(t,\tau)$.

$$\begin{aligned}\langle G(t,\tau)\rangle = {} & (1+a)^2 P_0^{1,1}(t,\tau) + 1 \cdot P_0^{-1,-1}(t,\tau) \\ & + \left[(1+a)^2 \cdot P_{even}^{1,1}(t,\tau) + 1 \cdot P_{even}^{-1,-1}(t,\tau)\right] \\ & - (1+a)\left[P_{odd}^{1,-1}(t,\tau) + P_{odd}^{-1,1}(t,\tau)\right]\end{aligned} \tag{4}$$

Assuming that the probability of finding the cell in the two modes initially (at time t) is similar (CW_{bias} ~ 0.5), the expression reduces to:

$$\langle G(t,\tau)\rangle = \frac{(1+a)^2+1}{2} \cdot \left(P_0(t,\tau) + P_{even}(t,\tau)\right) \tag{5}$$

$$-(1+a)\cdot P_{odd}(t,\tau)$$

The probability P_{even} represents the cumulative probability that the cell undergoes an even and non-zero number of reversals ($k = 2, 4, 6, ...$). Similarly, the probability P_{odd} represents the cumulative probability that the cell undergoes an odd number of reversals ($k = 1, 3, 5, ...$).

To determine the probabilities, we extended an approach previously developed by Groβmann and co-workers for the case of an symmetric swimmer that stochastically reverses its direction of swimming [100]. Our experimental measurements suggested that the run-times obeyed a Gamma distribution (Figure 4-5A, main text):

$$\Omega(t) = \frac{r^M t^{M-1} e^{-rt}}{(M-1)!}$$

where, M is the shape-parameter and $1/r$ is the scale-parameter. The probability of $k = 0$ reversals was then determined in the Laplacian space as [100]:

$$P_0(t,\tau) \leftrightarrow \hat{P}_0(s,u) = \frac{1}{u}\cdot\left[\frac{1}{s} - \frac{1}{1-\widehat{\Omega}(s)}\cdot\frac{\widehat{\Omega}(s)-\widehat{\Omega}(u)}{u-s}\right] \quad (6)$$

$$\widehat{\Omega}(s) = \left(\frac{r}{r+s}\right)^2 \quad (7)$$

here,

To determine P_{even}, a summation of the even probabilities ($k = 2, 4, 6, ...$) was obtained while accounting for the turning angle, $\emptyset$:

$$P_{even}(t,\tau) \leftrightarrow \hat{\beta}_{even}(s,u) = \sum_{k=2,4,6,\ldots}^{\infty} \frac{1-\widehat{\Omega}(u)}{u}\cdot\frac{\left(\widehat{\Omega}(u)\right)^{k-1}}{1-\widehat{\Omega}(s)}\cdot\frac{\widehat{\Omega}(s)-\widehat{\Omega}(u)}{u-s}\cdot\alpha^k$$

$$= \alpha \cdot \Upsilon(s,u) \sum_{k=2,4,6,\ldots}^{\infty} \left(\alpha \cdot \widehat{\Omega}(u)\right)^{k-1} \tag{8}$$

$$\Upsilon(s,u) = \frac{1-\widehat{\Omega}(u)}{u} \cdot \frac{1}{1-\widehat{\Omega}(s)} \cdot \frac{\widehat{\Omega}(s)-\widehat{\Omega}(u)}{u-s} \tag{9}$$

The series summation reduces to:

$$\sum_{k=2,4,6,\ldots}^{\infty} \left(\alpha \cdot \widehat{\Omega}(u)\right)^{k-1} = \frac{\alpha \cdot \widehat{\Omega}(u)}{1-\left(\alpha \cdot \widehat{\Omega}(u)\right)^2} \tag{10}$$

Here, $\alpha = |\langle cos\emptyset \rangle|$. The turning angle, $\emptyset$, randomizes the bacterial trajectory similar to rotational diffusion but only acts upon a reversal.

Similarly,

$$P_{odd}(t,\tau) \leftrightarrow \hat{\beta}_{odd}(s,u) = \alpha \cdot \Upsilon(s,u) \sum_{k=1,3,5,\ldots}^{\infty} \left(\alpha \cdot \widehat{\Omega}(u)\right)^{k-1} \tag{11}$$

The series summation reduces to:

$$\sum_{k=1,3,5,\ldots}^{\infty} \left(\alpha \cdot \widehat{\Omega}(u)\right)^{k-1} = \frac{1}{1-\left(\alpha \cdot \widehat{\Omega}(u)\right)^2} \tag{12}$$

To estimate the long-time probabilities, the final value theorem was employed:

$$\hat{P}_k(t \to \infty, \tau) = \lim_{s \to 0} s \cdot \hat{P}_k(s,u) \tag{13}$$

Substituting (6) and (7) in (13),

$$P_0(t \to \infty, \tau) = \frac{1}{u} - \frac{r}{u^2 M}\left(1-\widehat{\Omega}(u)\right) \tag{14}$$

Substituting (7), (8), (9), and (10) in (13),

$$P_{even}(t \to \infty, \tau) \leftrightarrow \lim_{s \to 0} s \cdot \hat{\beta}_{even}(s, u) = \frac{r}{M} \cdot \frac{\widehat{\Omega}(u)}{u^2} \cdot \frac{\alpha^2 \left(1 - \widehat{\Omega}(u)\right)^2}{1 - \alpha^2 \cdot \widehat{\Omega}(u)^2} \tag{15}$$

Similarly,

$$P_{odd}(t \to \infty, \tau) \leftrightarrow \lim_{s \to 0} s \cdot \hat{\beta}_{odd}(s, u) = \frac{r}{M} \cdot \frac{1}{u^2} \cdot \frac{\alpha \left(1 - \widehat{\Omega}(u)\right)^2}{1 - \alpha^2 \cdot \widehat{\Omega}(u)^2} \tag{16}$$

Combining equations (14), (15), (16), and (5),

$$\begin{aligned} \hat{G}(u) = \frac{(1+a)^2 + 1}{2} & \\ \cdot \left\{ \frac{1}{u} - \frac{r}{u^2 M} \left(1 - \widehat{\Omega}(u)\right) + \frac{r}{M} \cdot \frac{\widehat{\Omega}(u)}{u^2} \cdot \frac{\alpha^2 \left(1 - \widehat{\Omega}(u)\right)^2}{1 - \alpha^2 \cdot \widehat{\Omega}(u)^2} \right\} & \\ - (1+a) \cdot \left\{ \frac{r}{M} \cdot \frac{1}{u^2} \cdot \frac{\alpha \left(1 - \widehat{\Omega}(u)\right)^2}{1 - \alpha^2 \cdot \widehat{\Omega}(u)^2} \right\} & \end{aligned} \tag{17}$$

For two-dimensions, the diffusion coefficient *D* is related to the average correlation over long-times as [100]:

$$D = \frac{v_0^2}{2} \hat{G}(D_\theta)$$

Finally, we obtain the following expression for the diffusion coefficient:

or,

$$D$$

$$= \frac{v_0^2}{2D_\theta}\left[\frac{(1+a)^2+1}{2}\cdot\left\{\begin{array}{c} 1-\frac{r}{MD_\theta}\left(1-\frac{r^M}{(r+D_\theta)^M}\right) \\ +\frac{\alpha^2 r}{MD_\theta}\cdot\frac{r^M}{(r+D_\theta)^M}\cdot\frac{((r+D_\theta)^M-r^M)^2}{(r+D_\theta)^{2M}-\alpha^2 r^{2M}}\end{array}\right\}\right] \quad (18)$$
$$-(1+a)\left\{\frac{\alpha\cdot r}{MD_\theta}\cdot\frac{((r+D_\theta)^M-r^M)^2}{(r+D_\theta)^{2M}-\alpha^2 r^{2M}}\right\}$$

For $a = 0$ (no asymmetry in speeds) and $\alpha = 1$ (180° reversals), equation 3.13 from [100] is recovered.

A Gamma fit to the experimentally-determined wait-time distributions yielded M = 3 (Figure 4-5A, main text), such that:

$$D$$

$$= \frac{v_0^2}{2D_\theta}\left[\frac{(1+a)^2+1}{2}\cdot\left\{\begin{array}{c} 1-\frac{\omega}{D_\theta}\left(1-\frac{(3\omega)^3}{(3\omega+D_\theta)^3}\right) \\ +\frac{|\langle cos\emptyset\rangle|^2\omega}{D_\theta}\cdot\frac{(3\omega)^3}{(3\omega+D_\theta)^3}\cdot\frac{((3\omega+D_\theta)^3-(3\omega)^3)^2}{(3\omega+D_\theta)^6-|\langle cos\emptyset\rangle|^2(3\omega)^6}\end{array}\right\}\right]$$
$$-(1+a)\left\{\frac{|\langle cos\emptyset\rangle|\cdot\omega}{D_\theta}\cdot\frac{((3\omega+D_\theta)^3-(3\omega)^3)^2}{(3\omega+D_\theta)^6-|\langle cos\emptyset\rangle|^2(3\omega)^6}\right\}$$

(19)

Here, the reversal frequency $\omega = r/M$.

B.5. Single cell simulation

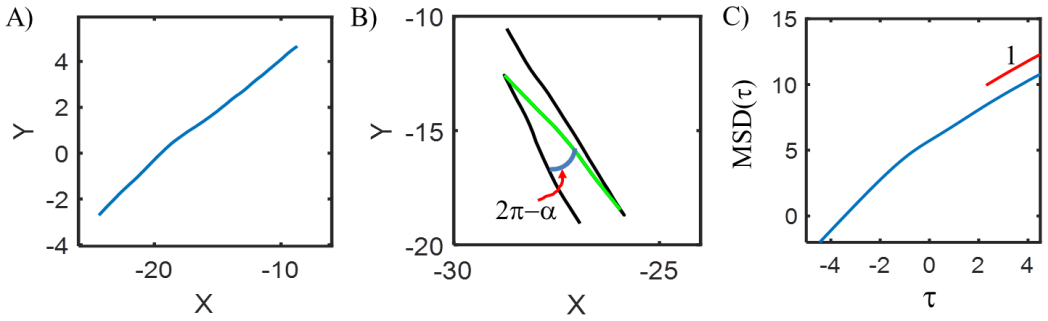

Appendix B Figure 6. Single cell simulations of asymmetric run-reversers
A) A representative cell trajectory as it engages in a simulated run. The total run interval, τ, was split into 71 batches. The trajectory is not a straight-line owing to Brownian motion. **B)** Two simulated reversals are indicated. Black and green segments indicate pusher ($v = v_o(1 + a)$) and puller ($v = v_o$) modes respectively. **C)** Bacterial movements became purely diffusive over long times (~ 100 s) as indicated by the linear dependence of MSD on lag time τ (log-log plot). The value of the diffusion coefficient was calculated at these long times. Reprinted with permission from [16].

Each cell was initialized at the origin ($x = 0, y = 0$) at time $t = 0$ s. Cell movement was simulated as alternating runs and reversals over a total duration of ~ 350 s. At the beginning of each run (or reversal), the time interval τ_i for the run (or reversal) was sampled from a Gamma distribution that was generated based on fits to experimental measurements (Figure 4-5A). Each i^{th} time interval τ_i was then divided into *n* batches of equal durations, Δt. The time-step Δt was fixed at 10 ms. Any remainder, $rem(\tau_i, \Delta t) = \zeta\ (< \Delta t)$, was allocated to an $(n+1)^{th}$ batch. Within each batch, the cell was assumed to travel in a straight line with a displacement given by:

$\boldsymbol{\varepsilon}_n = \boldsymbol{v}_n\zeta$, where $\zeta = \Delta t$ for each of the *n* bins and $\zeta = \tau_i - n\Delta t$ for the final $n+1^{\text{th}}$ bin.

$$\therefore \boldsymbol{\varepsilon}_n = h(t+\tau_i)v_o\big(1 + aH(t+\tau_i)\big)\boldsymbol{e}_n \times \zeta$$

(20)

Here, *h* is either +1 or -1 for a given interval:

$$h(t+\tau_i) = -h(t+\tau_{i+1}) \text{ and } |h(t+\tau_i)| = 1$$

(21)

The Heaviside function: $H = 1 \rightarrow h = 1$ and $H = 0 \rightarrow h = -1$. The position vector is simply: $\boldsymbol{e}_n = \cos(\theta_n)\boldsymbol{\delta_i} + \sin(\theta_n)\,\boldsymbol{\delta_j}$

The angle θ_n was updated in between batches to account for rotational Brownian motion:

$$\theta_{n+1}^i = \theta_n^i + (2D_\theta\zeta)^{0.5}$$

(22)

The x and y positions over time were calculated from, $x_k = \sum_1^k \boldsymbol{\delta_i}.\boldsymbol{\varepsilon}_n,\ y_k = \sum_1^k \boldsymbol{\delta_j}.\boldsymbol{\varepsilon}_n$. A sample trajectory for one such interval consisting of $n+1 = 71$ batches is indicated in Appendix B Figure 6A.

The turn angle, ∅, is the angle between the original direction just before and the new direction just after a reversal. The angle tends to randomize the bacterial random walk, in addition to Brownian motion. The turn angle is likely influenced by kinematic properties of the cell body and filaments, as well as the flexibility of the flagellar hook. To account for the turning angle, at the start of each time interval τ_i , the angle θ was updated as:

$$\theta_1^{i+1} = \theta_{end}^{i} + (2D_\theta\zeta)^{0.5} + \emptyset^{i+1}$$

Note that this update only occurred at the start of each interval; subsequent batch-updates for θ within the interval occurred as per equation 22. The angles $\emptyset^{i+1}$ were sampled from a distribution that was obtained from fits to the experimental data (Figure 4-1B, main text). A representative reversal with the turning angle is shown in Appendix B Figure 6B.

Diffusion Coefficients

The simulations were repeated for 1000 cells. Mean square displacements were calculated as:

$$MSD(\tau) = \langle\big(x(t+\tau) - x(t)\big)^2 + \big(y(t+\tau) - y(t)\big)^2\rangle$$

The MSD versus the lag time τ became linear at long times (~ 100 s), indicating purely diffusive behavior (Appendix B Figure 6C). The diffusion coefficient was calculated from the slope of MSD versus τ over these times (D = slope/4 for two-dimensional walk).

Simulated diffusion with varying asymmetry and CW_{bias}

Following the scheme described above, we simulated movements of cells over varying CW_{bias}. To vary the bias, the mean wait times in the pusher and puller modes were varied. The wait times were Gamma distributed and the sum of the intervals ($\tau_{i,pusher}$ and $\tau_{i,puller}$) was fixed at 0.35 s. Diffusion coefficients were calculated by simulating 1000 cells each for the conditions $a = 0$, 0.25, 0.5, 0.75, and 1; for CW_{bias} = 0.14, 0.25, 0.39, 0.48, 0.61, 0.75, and 0.86. Results are plotted in Figure 4-5D.

B.6. Swimming asymmetry away from bounding surfaces

Differences in swimming speeds in the pusher and puller modes have been reported for *Vibrio alginolyticus*, but only near surfaces [107]. A similar asymmetry was observed in *Pseudomonas putida* in the bulk fluid [97]. To determine if near-wall effects played a role in the speed asymmetry in *H. pylori*, we recorded motile cells in the bulk, away from surfaces. To determine if near-wall hydrodynamic effects influence the asymmetry in *H. pylori*, we focused the microscope objective ~ 200 μm in the bulk fluid and recorded motility away from any surfaces in a culture-dish (see *Materials and Methods*, section 4.4). Appendix B Figure 7 shows one such trajectory. We observed that swimming speeds in consecutive segments were anti-correlated, in a similar manner as trajectories near surfaces (refer to Figure 4-1). Although this observation has been made for a small number of cells (n = 4 cells), this preliminary data suggests that the asymmetry is unlikely to be due to the presence of nearby surfaces.

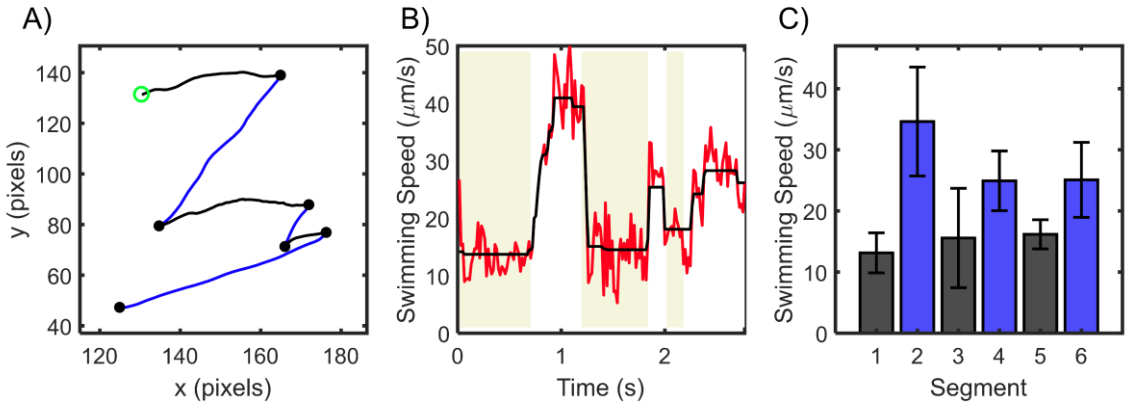

Appendix B Figure 7. *H. pylori* cells exhibit asymmetry ~200μm away from surfaces. **A)** Trajectory of a representative cell is shown, where the segment-color changes upon each reversal. Beginning of the trajectory is denoted by a green circle, reversals are denoted by black circles. **B)** Quantitatively determined speeds of the same cell. The

(Appendix B Figure 7 Continued…)
shaded regions indicate alternating swimming modes. **C)** Average speed for each segment along with the standard deviation is indicated in a chronological manner. Reprinted with permission from [16].

B.7. Dynamic measurements of the chemotactic output in *H. pylori*

The genes encoding components of the chemotaxis network and the flagellar motors in *H. pylori* share many similarities to those in the model bacterium *E. coli* [59, 62-65]. However, genes encoding the key enzymes responsible for chemotactic adaptation, methyltransferase CheR and methylesterase CheB, are absent from the *H. pylori* genome. *H. pylori* do contain homologues to the CheV proteins [66], which have been implicated in chemotactic adaptation in *Bacillus subtilis* [119, 120]. This raises the question: does the chemotaxis network in *H. pylori* adapt to sensed stimuli? In *E. coli*, chemotactic adaptation is robust: the CW_{bias} is restored precisely to the pre-stimulus level within minutes [11]. Such precise adaptation allows *E. coli* to respond to a large dynamic range of chemical (attractant/repellent) concentrations. Determining whether chemotactic adaptation occurs in *H. pylori* is important for studying the full capability of *H. pylori* to chemotax.

The method developed in Chapter 4 and [16] allows us to measure changes in CW_{bias} over time, as shown in Appendix B Figure 8A. In Appendix B Figure 8B, we report data from our initial experiments where we exposed swimming *H. pylori* cells to intermediate concentrations of a known attractant and a known repellent. Slight changes in the CW_{bias} were observed. Higher concentrations of the repellent hydrochloric acid are expected to decrease the environmental pH. *H. pylori* lose their motility at a pH < 3

[121]. A change in pH could also interfere with the functions of the proton-powered flagellar motors in this organism. Due to the urease enzyme, addition of urea to the medium allows *H. pylori* to survive and remain motile at lower pH [122, 123], however, mixing urea and acid will confound the experimental design. These issues will need to be addressed in future work. Finally, we also determined how cells adapt to sudden changes in temperatures. Sample data is shown in Appendix B Figure 8C, in which the cells were subjected to a step increase in the temperature.

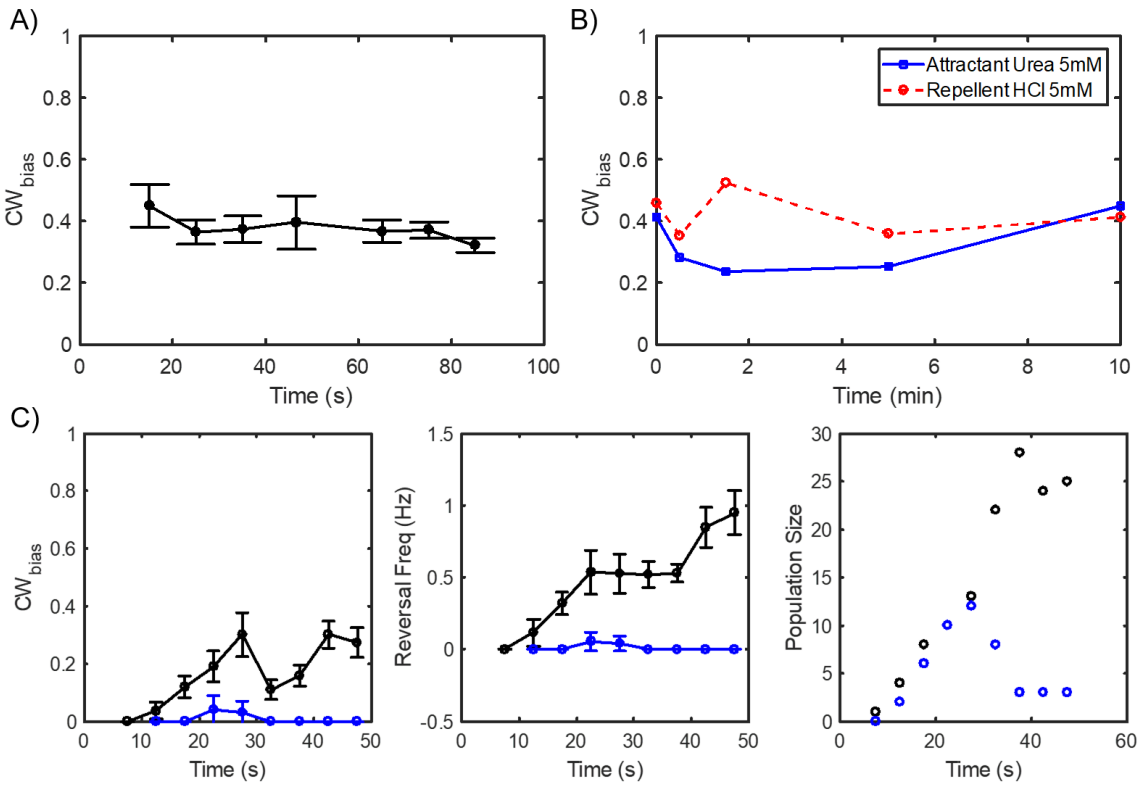

Appendix B Figure 8. Dynamic measurements of CW_{bias} in *H. pylori*.
A) For *H. pylori* swimming in The variation in CW_{bias} over time was determined by repeating the analysis in [16] for swimmers recorded over different time points. The time-window for the calculation of each value was ~ 30 s and the sample sizes ranged from n = 11 to 62 cells. **B)** Dynamics measurement of CW_{bias} in swimming *H. pylori*

(Appendix B Figure 8 Continued…)
subjected to intermediate concentrations of chemo-effectors (attractant urea, 5mM, blue; repellent hydrochloric acid, 5mM, red dashed line). Each data point was obtained by averaging CW_{bias} for n > 50 cells recorded over 20-30 seconds. **C)** Dynamic measurement of CW_{bias} (*left*) and reversal frequency (*middle*) in *H. pylori* swimming at room temperature and subjected to a temperature impulse of 37°C (black). In blue are the data from the control experiment where cells continued swimming at room temperature. *Right*: the cell population sizes for each time-point are indicated.

An important technique to determine the chemotaxis behavior in bacteria are to study their accumulation near point sources of attractants. This technique has been previously applied to study chemotaxis in *H. pylori* [87, 88, 114]. Our preliminary assay with a rudimentary setup is indicated in Appendix B Figure 9, where we stimulated *H. pylori* with a micropipette containing 1 mM attractant urea. Because we carried out this assay near a surface, we could determine the mode of swimming based on circular trajectories (refer to Figure 4-2), however, these circular trajectories trapped the cells near the surface so we were not able to observe the accumulation of cells at the mouth of the micropipette.

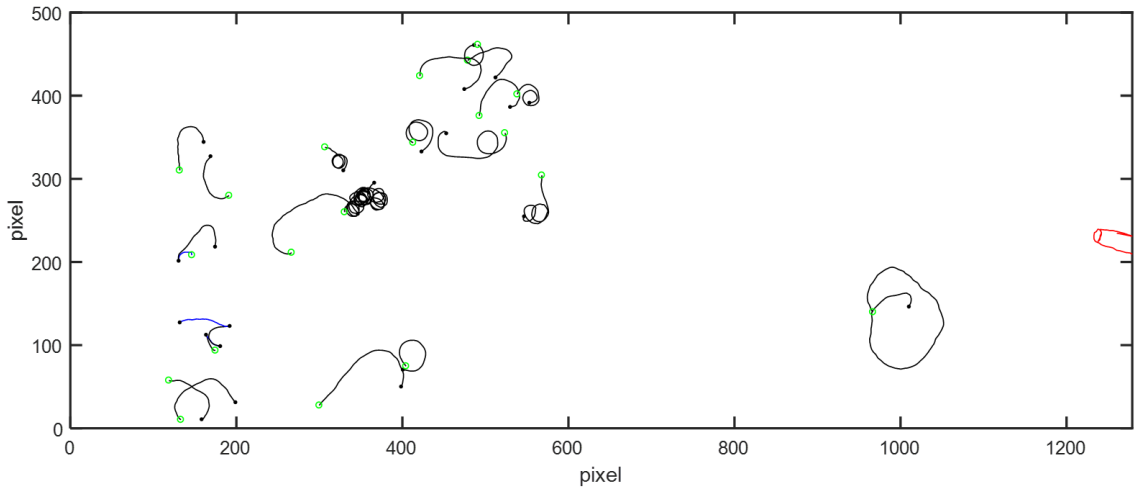

Appendix B Figure 9. Chemotaxis of *H. pylori* near a micropipette.
Motility of *H. pylori* cells was measured near a micropipette (red) containing 1 mM solution of attractant urea. The green circle denotes the start and the black dot denotes the end of each trajectory. Most cells near the surface swim in CW circles, which corresponds to the pusher mode ($CW_{bias} = 0$).

In addition to all the future work discussed here, many fascinating questions remain about the chemotaxis network, the flagellar motors, and the cooperativity between them in *H. pylori*. We expect that our assays and future continuation of this work will help identify the role of key enzymes in these systems.

APPENDIX C

DESIGN OF AN ORTHOGONAL IMAGING CHAMBER[‡]

C.1. Introduction

Confocal fluorescence microscopy has been the technique of choice to visualize x-z or axial cross-sectional views (i.e., images in a plane parallel to the optical plane) of microscopic fluorescent objects, using image slices acquired in the focal plane. However, reconstructed x-z cross-sectional profiles of fluorescent objects which are the size of several microns can be distorted in confocal microscopy [124, 125]. These distortions are caused largely by the mismatch between the refractive indices of the medium in which the sample is present and the oil present on typical oil-immersion objectives. The mismatch causes differences between axial travel of the objective relative to the sample and travel of the focal plane in the sample itself, resulting in distortion of the x-z shapes. Also, refractive-index mismatch causes the axial resolution to worsen and peak intensity to decrease with travel into the sample.

Methods to correct for the mismatch have been proposed including the use of water-objective lenses and the calculation of correction factors [124, 126-128]. Other recent approaches include the use of prisms to deflect light in such a way that the x-z cross-section can be directly imaged [129, 130]. Here we developed an approach to image x-z shapes of fluorescent objects, which does not require scaling with correction factors or extra devices like prisms in the light path. We designed an imaging chamber in

[‡] This appendix is a part of the published work (reprinted with permission) "A method for direct imaging of x–z cross-sections of fluorescent samples" by A Katiyar*, JD Antani*, et al., 2020, Journal of Microscopy, 281(3), 224-230. © 2020 Royal Microscopical Society. (* equal authors)

which samples could be mounted along a plane perpendicular to the focal plane, effectively making what would normally be a measurement in the x-z plane, into a measurement in the x-y plane. Imaging of the x-y cross-sections of spherical polystyrene beads immersed in mounting medium with an oil-immersion objective revealed a substantial reduction in distortion. We further tested the chamber for imaging cells and nuclei (see the publication [17] for details).

C.2. Design of the chamber

A 35 × 75 × 11.75mm (W×L×H) chamber was designed to hold two glass slides in an orientation perpendicular to the focal plane as shown in Appendix C Figure 1 and Appendix C Figure 2. A 22mm × 22mm × 0.17 mm coverslip (Fisher Scientific, Cat. No. 12-542-B) was adhered to the bottom of the imaging chamber with RTV-108 glue (Momentive RTV Silicone Sealant) to protect the microscope objective from brushing against the edges of the vertical slides. Microscope glass slides (VWR, Cat. No. 26004-422) and coverslips were cut (25mm x 11 mm and 22mm x 11 mm respectively) to enable imaging with a long working distance condenser (Ti-C CLWD, Nikon Instrument Inc.). Two such slides were then inserted in the slotted grooves (8.75 x 1.3 mm with a depth of 1.75 mm) along the walls of the chamber. Once positioned, the vertical slides were pressed against the bottom coverslip by tightening the lid of the imaging chamber (35x35x3 mm) with four threaded screws (Appendix C Figure 1). An imaging window was provided within the lid to enable simultaneous transmitted light and fluorescence microscopy. All the designs were developed with CAD software

(SolidWorks, 3D Assault Systems) and 3D-printed (VeroWhite resin material, 3D printer: Stratasys Objet Eden 260V).

A schematic of our mounting approach is shown in Appendix C Figure 1. A 3D-printed chamber was designed to hold two glass slides perpendicular to the focal plane. The microscope objective was focused near the bottom edge of the glass slide and the region was scanned to image fluorescent objects. In this setup, the glass slide is held parallel to the optical axis of the microscope, allowing us to image the cross-section orthogonal to the glass slide in the x-y plane (this cross-section would normally be the x-z cross-section reconstructed from confocal z-stacks). The light path in our setup was such that the light from the objective lens passed through the coverslip and into the glycerol-based mounting media before exciting the fluorophores in the sample.

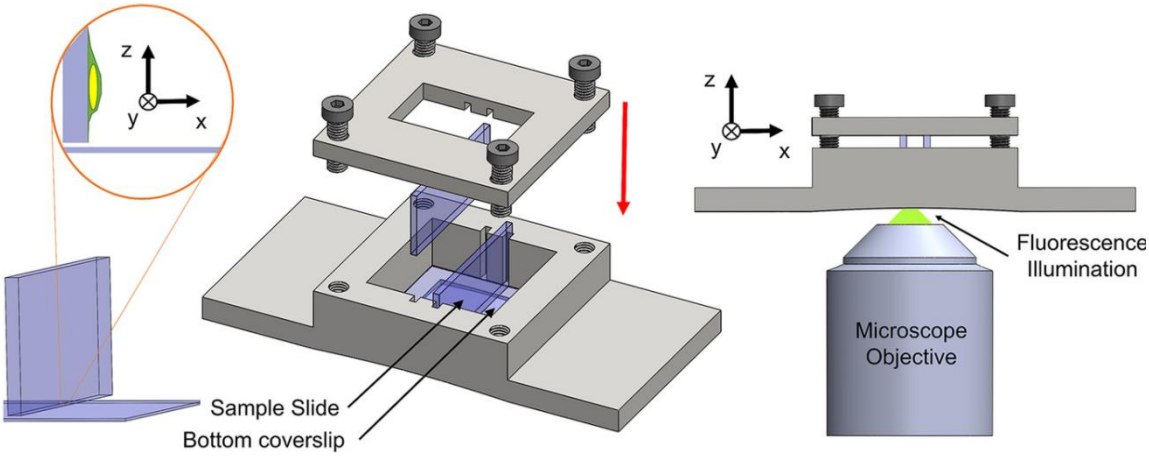

Appendix C Figure 1. Schematic of the orthogonal imaging chamber.
3D-printed chamber holds slides in an orientation perpendicular to focal plane. Glass slides are slotted vertically in the grooves along the walls of the chamber. A lid is tightened to push the glass slides against the bottom coverslip with threaded screws. A

(Appendix C Figure 1 Continued…)

window is provided in the lid to enable transmitted light microscopy. A photo of the imaging chamber (total length = 75 mm) is included. Reprinted with permission from [17].

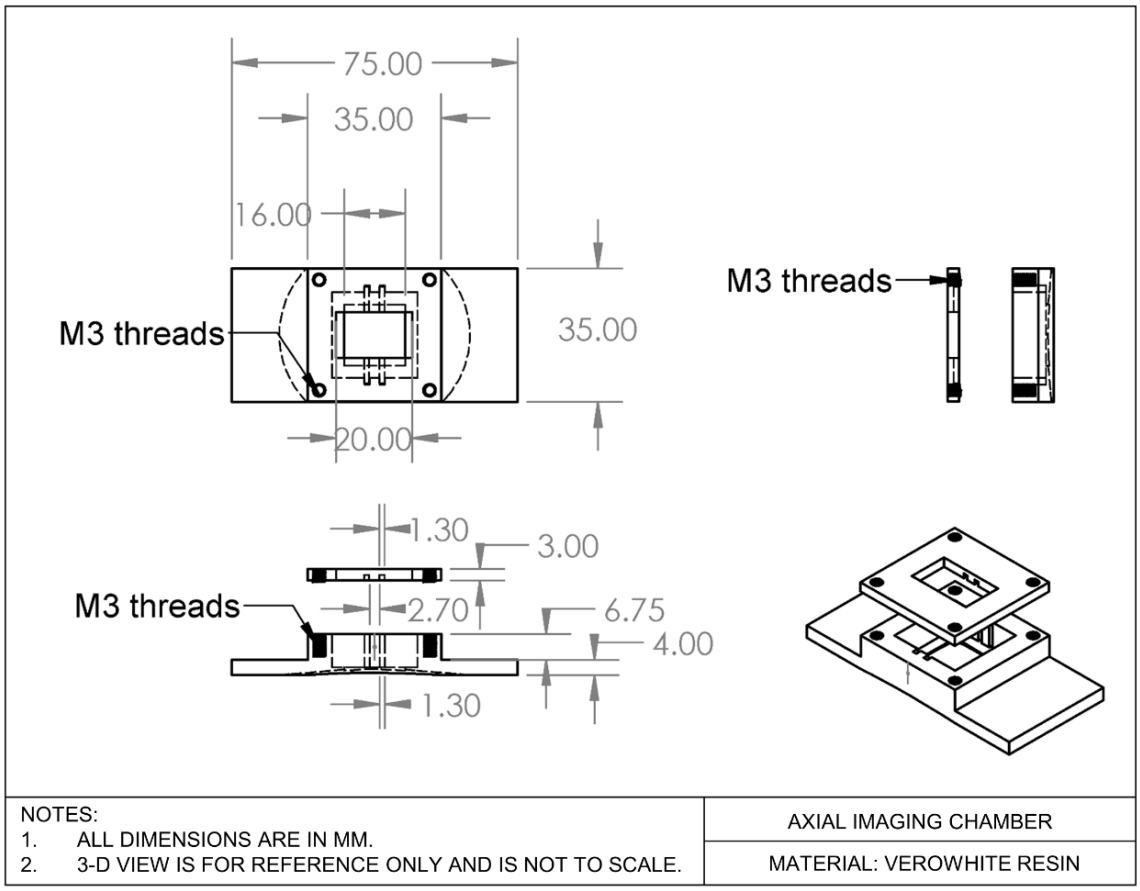

Appendix C Figure 2. Engineering drawing of the orthogonal imaging chamber. Reprinted with permission from [17].

C.3. The chamber allows circumventing the error in z-stack reconstructions

We first reconstructed the x-z cross-sections of fluorescent beads of known diameters from confocal z-stacks. We compared these x-z cross-sections to single confocal fluorescent images of x-y cross-sections of fluorescent beads in the orthogonal

imaging chamber. All images were acquired on a laser scanning confocal microscope (see the published work [17] for details) using a Nikon CFI Plan Apo Lambda 60X/1.4 NA oil immersion objective lens. Beads were mounted on the glass slides in mounting media with a refractive index of 1.45, while the refractive index of oil was around 1.52. Consistent with previous reports [131], the x-z shapes of 10-15 μm fluorescent beads reconstructed from confocal z-stack imaging resembled a tear-drop shape (Appendix C Figure 3A, C). The average change in the height of the bead was ~ 53 % for the 10 μm beads and ~ 45 % for the 15 μm beads (Appendix C Figure 3B, D). This distortion was measured for confocal z-stacks acquired at a step-size of ~250 nm which is below the Nyquist criterion.

In contrast, images of the beads acquired with the orthogonal imaging chamber were not distorted from their circular shapes (Appendix C Figure 3A, C; right). The measured heights were statistically indistinguishable from the diameter specified by the manufacturer (Appendix C Figure 3B**,** D). These data demonstrate the utility of the orthogonal imaging chamber for reducing distortions in images of shapes captured orthogonal to the mounting surface.

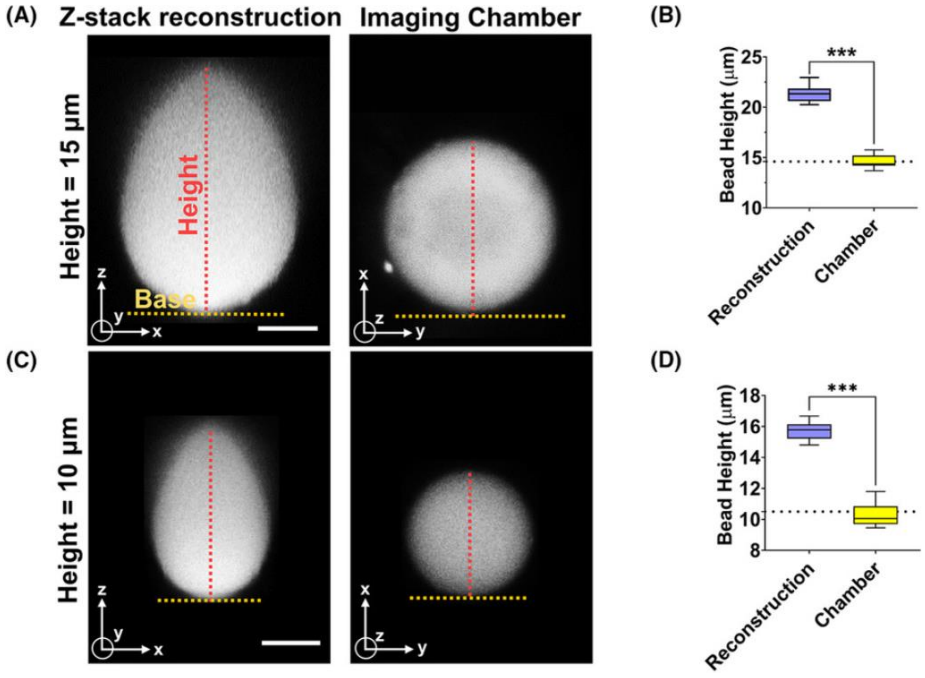

Appendix C Figure 3. Confocal sectioning versus the orthogonal imaging chamber. Comparison of x-z shapes reconstructed from confocal sectioning, and corresponding x-y shapes acquired in the orthogonal imaging chamber. **A)** Image of x-z cross-section of fluorescent bead (diameter = 15 µm) reconstructed from confocal z-stacks and acquired with the imaging chamber. Scale bar is 5 µm. **B)** The graph shows a quantitative comparison of diameter of beads (d = 15 µm) corresponding to the two imaging methods in A). Dotted line represents manufacturer's specification for the mean diameter of the bead. The experiments were performed in triplicates and 20 beads were quantified. "***" signifies statistically significant difference ($p < 0.05$ by student's *t*-test). **C)** Image shows x-z cross-section of fluorescent bead (diameter = 10 µm) reconstructed from confocal z-stacks and a single x-y image acquired with the orthogonal imaging chamber. Scale bar is 5 µm. **D)** Graph shows a comparison of diameter of beads (d = 10 µm) corresponding to the two imaging methods in C). Dotted line represents manufacturer's specification for the mean diameter of the bead. The experiments were performed in triplicates and 20 beads were quantified. "***" signifies statistically significant difference ($p < 0.05$ by student's *t*-test). Reprinted with permission from [17].

C.4. Discussion

Three-dimensional confocal microscopy is the technique of choice to visualize x-z cross-sections of particles and cellular structures, but these cross-sections are subject to considerable distortions owing largely to the phenomenon of refractive-index mismatch. Here we developed an approach for mounting samples side-ways such that what is normally the x-z cross-section for imaging conventional samples is directly imaged in the x-y plane in the orthogonal imaging chamber. The chamber allows imaging of planes perpendicular to the glass slide with resolution similar to that achieved in XY imaging. Additionally, the reconstruction needed to visualize x-z cross-sections is not required here, as only one image is required of the x-y plane. As such our approach will have better time resolution than approaches that involve reconstruction of confocal z-stacks.

One limitation of our approach is that cells can only be imaged close to the edge of the glass slide because of the low working distance of typical 60X or 100X objectives. Nonetheless, for an imaging depth of 70-100 μm with reference to the top surface of the coverslip and an imaging width of 15 mm for our glass slides, the area over which imaging can be performed is 1 – 1.5 mm^2, which enables imaging of a substantially large number of micron-sized objects. Further, the area of imaging may also be increased by using objectives that have high working distances. The vertical mounting of cells could potentially impact their shapes due to gravity. However, gravity does not affect the shape of mammalian cells as they adhere and spread on a surface [132]. This is consistent with the fact that gravitational forces on cells are very small compared to forces associated with molecular motors that drive cell spreading [133].

Fluorescence intensity drops with distance from the cover slip [134]. This could make it difficult to visualize dimmer samples in the orthogonal imaging chamber. While, the point spread function becomes more diffuse laterally with depth [124], the gross shape of object remains unchanged. Finally, the imaging chamber does not solve the problem of 3-D rendering of objects; any 3D reconstructions will appear elongated in the z direction.

The imaging chamber is compatible with both upright and inverted microscopes, and can be coupled with micromanipulation devices for studying force-deformation relationships of soft particles or cells. Also, it may prove valuable in studying dynamic events in cells in the orthogonal direction. For example, a similar orthogonal mounting approach as ours has been previously used by [135] to study mammalian cell migration. The improved resolution and time resolution offered by our approach should be especially useful in this regard.

C.5. Conclusion

Orthogonal mounting of fluorescent samples here is a simple but effective method to directly image x-z cross-sections. The improved spatial and time resolution of this method should prove useful for diverse biological applications.

APPENDIX D

TRACKING OF MIGRATING NUCLEI FROM MICROSCOPY IMAGES

In this work, I discuss our approach to automatically track mammalian cell nuclei during cell migration. The nuclei were fluorescently labeled with Hoechst or GFP-BAF and the nuclear boundaries were visualized through confocal microscopy. The algorithm for finding the centroid of nuclei is described in Appendix D Figure 1.

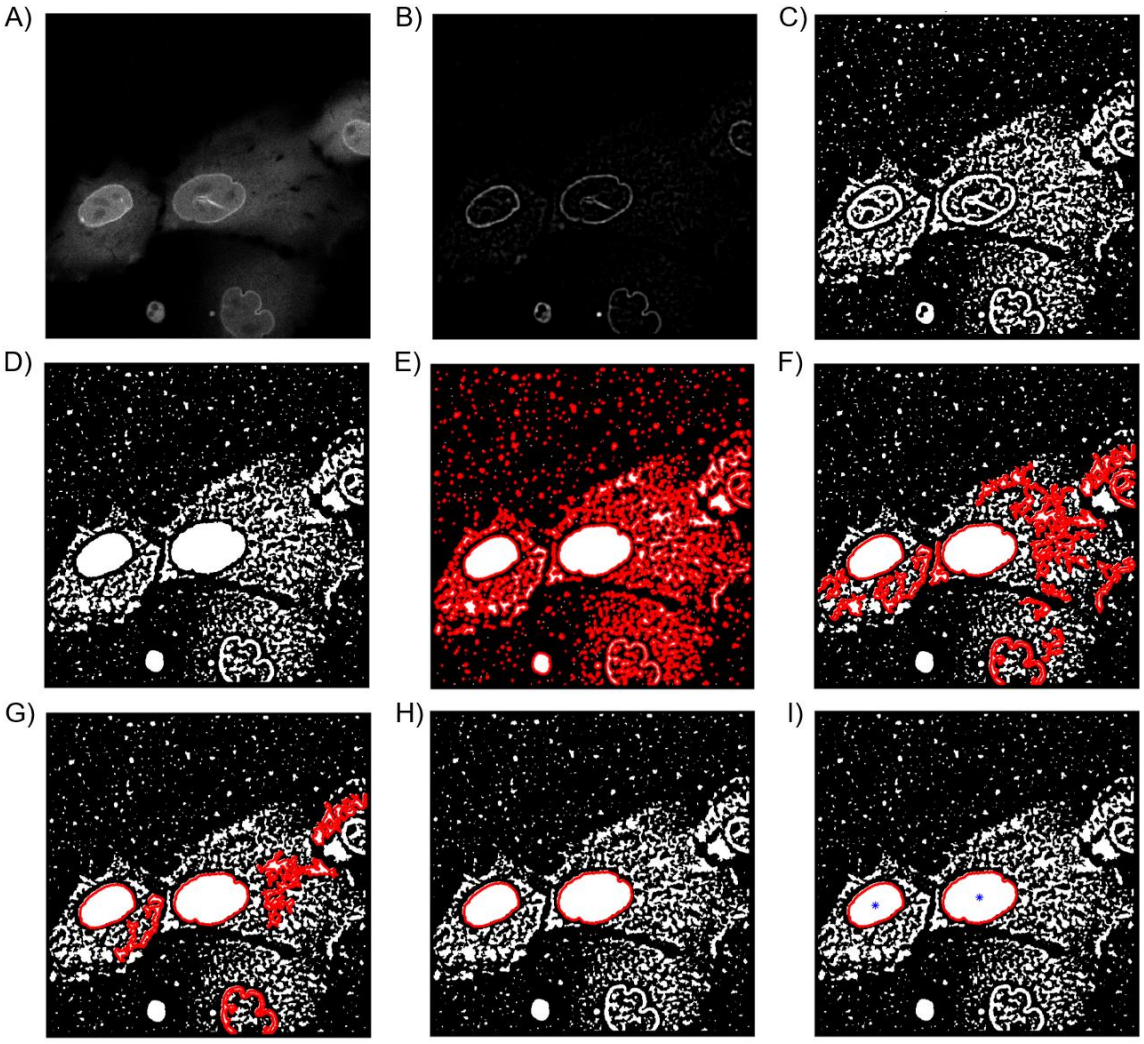

Appendix D Figure 1. Tracking cellular nuclei through image analysis.

(Appendix D Figure 1 Continued…)

A) Original image: a single frame from the video of migrating nuclei is shown as a sample image. **B)** A size based band-pass filter was applied, using the `bpass` function in MATLAB. **C)** Based on an automated threshold, each grayscale pixel in the image was binarized to Black or White (`imbinarize` function in MATLAB). **D)** Closed loops with white boundaries were filled to yield bounded features, using the `imfill` function in MATLAB. **E)** Boundaries (plotted as red lines) of all closed loops were determined using the `bwboundaries` function in MATLAB. **F)** A minimum perimeter filter was applied to each feature. Features with perimeter higher the threshold value were retained. **G)** A minimum area filter was applied to each feature. Features with area higher than the threshold value were retained. **H)** A circularity threshold was applied: features with $Circularity = \frac{4\pi(area)}{(perimeter)^2} > 0.4$ were retained. Only the nuclei remained in the sample image. **I)** The centroid of each nucleus (denoted as a blue star) was calculated by averaging the X- and Y- coordinates of the boundaries.